Master Thesis

Modelling of Critical Gas Velocities based on the Entrained Droplet Model for Gas Wells and the Effect of Heat Loss on Gas Production

Written by:
Gernot Schwaiger, BSc
m0835141

Advisors:
Univ.-Prof. Dipl.-Ing. Dr.mont. Herbert Hofstätter
Dipl.-Ing. Dr.mont. Rudolf K. Fruhwirth

Leoben, Austria; February 24, 2016

EIDESSTATTLICHE ERKLÄRUNG

Ich erkläre an Eides statt, dass ich die vorliegende Diplomarbeit selbständig und ohne fremde Hilfe verfasst, andere als die angegebenen Quellen und Hilfsmittel nicht benutzt und die den benutzten Quellen wörtlich und inhaltlich entnommenen Stellen als solche erkenntlich gemacht habe.

Datum Unterschrift

AFFIDAVIT

I hereby declare that the content of this work is my own composition and has not been submitted previously for any higher degree. All extracts have been distinguished using quoted references and all information sources have been acknowledged.

Date

Signature

Acknowledgement

For their efforts and assistance, a special *Thank You* to the Chair of Petroleum and Geothermal Energy Recovery and its head, Univ.-Prof. Dipl.-Ing. Dr.mont. Herbert Hofstätter.

Dipl.-Ing. Dr.mont. Rudolf K. Fruhwirth (Chair of Petroleum and Geothermal Energy Recovery) has been the ideal thesis supervisor. His advice and patient encouragement aided the writing of this thesis in innumerable ways. He has set an example of excellence as a mentor and instructor.

Finally, I dedicate this work to my parents. Their support, love and encouragement from the beginning of my studies up until now have been invaluable. I am forever grateful and I could not have done this without you - **Thank You!**

To each of the above, I extend my deepest appreciation.

Abstract

Natural gas is one of the most important energy sources. In 2014, it accounted for about a quarter of the world energy consumption. Accordingly, gas production operations take place on a global level, and potential improvements of these operations may possibly have a significant effect. This holds especially true when those improvements are straightforward and easy to implement. Additionally, if these measures eliminate or postpone the need for workover interventions, there is a reduced risk of incidents which directly leads to an improved health, safety and environment record.

Thus, this thesis aims to investigate the ubiquitous issue of liquid loading which at some point affects every gas well. The liquid loading of gas wells occurs in many cases due to heat loss into the surrounding formation and decreasing flow velocities within the production tubing. Heat loss into the formation is facilitated by the circumstance that the use of appropriately insulated tubings is usually neglected. The absence of insulation permits unnecessary heat loss and thus a subsequent reduction in gas temperature. The reduced temperature in turn may lead to condensation of liquids, adding to the possibly already existing amount of fluids in the reservoir. Moreover, flow velocities decrease due to two main causes. One is the inevitable decline of reservoir pressure. The other is the reduced gas volume which is caused by the reduced gas temperature. Therefore, the understanding of heat flow and methods to reduce loss are desirable to tackle this issue.

In this thesis, the leading formula for the determination of critical gas flow velocities which must not be undercut by the actual flow velocity is investigated. This formula is colloquially known as ”Turner’s equation” and allows the calculation of the minimum flow velocity needed to lift liquid droplets all the way up to the surface. This “entrained droplet model” contains several parameters which ultimately depend on the prevailing pressure and temperature conditions. Hence, a heat transfer model was built in order to formulate and determine the pressure and temperature values for every point within the wellbore. The heat transfer model builds on concepts such as equation of state correlations, heat capacity models, density models, viscosity models, the Joule-Thomson coefficient and water density and water surface tension models.

As a result, it was found that insulated tubings lead to higher temperature and pressure readings, and that these effects can be quantified for different types and thicknesses of insulation materials. Moreover, the temperature increase also leads to higher actual gas velocities. Thus, critical gas velocities are exceeded more easily and for a longer period of time, and the margin between them is more pronounced. In the end, this allows an increased amount of gas production and the postponing of the economic limit of a gas well.

Kurzfassung

Erdgas ist eine der wichtigsten Energiequellen. Im Jahr 2014 war es verantwortlich für rund ein Viertel des Weltenergieverbrauchs. Dementsprechend findet Gasproduktion weltweit statt und mögliche Verbesserungen dieser Produktionsmethoden können erhebliche Auswirkungen haben. Dies gilt insbesondere dann, wenn diese Verbesserungen überschaubar und einfach zu implementieren sind. Weiters kann das Unfallrisiko reduziert werden, wenn diese Maßnahmen Workover-Tätigkeiten verhindern oder verzögern. Somit wird auch die Gesundheit-, Sicherheit- und Umwelt-Bilanz einer Firma verbessert.

Diese Arbeit beschäftigt sich mit der allgegenwärtigen Problematik von Flüssigkeitsansammlungen, welche jede Gasbohrung früher oder später betreffen. Die Flüssigkeitsansammlungen in Gasbohrungen entstehen in den meisten Fällen durch Wärmeverlust in die umliegende Gesteinsformation und durch abnehmende Fließgeschwindigkeiten im Förderstrang. Der Wärmeverlust wird begünstigt durch die Tatsache, dass die Verwendung von angemessen isolierten Fördersträngen meist vernachlässigt wird. Das Fehlen dieser Isolierung erlaubt unnötigen Wärmeverlust und daher eine Reduzierung der Gastemperatur. Die reduzierte Temperatur wiederum führt zur Kondensation von Flüssigkeiten, die zusätzlich zu den möglicherweise bereits existierenden Lagerstätten-Flüssigkeiten hinzukommen. Zudem nimmt die Fließgeschwindigkeit aus zwei Gründen ab. Einer ist der unvermeidliche Abfall des Lagerstätten-Drucks. Der andere ist das reduzierte Gasvolumen aufgrund der verringerten Temperatur. Daher sind das Verständnis des Wärmeflusses und Methoden zur Verringerung dieser Verluste wünschenswert, um diese Problematik zu bekämpfen.

Diese Arbeit untersucht die führende Formel zur Bestimmung der kritischen Gas-Geschwindigkeiten, welche nicht durch die tatsächlichen Gas-Geschwindigkeiten unterschritten werden dürfen. Diese Formel ist umgangssprachlich als „Turner-Gleichung“ bekannt und erlaubt die Berechnung der minimal benötigten Fließgeschwindigkeit, um Flüssigkeits-Tropfen bis zur Oberfläche zu befördern. Dieses „Mitgerissene Tröpfchen Modell“ beinhaltet mehrere Parameter, welche letztendlich von Druck und Temperatur abhängig sind. Daher wurde ein Wärmeübertragungs-Modell kreiert, um die vorherrschenden Druck- und Temperatur-Bedingungen im gesamten Förderstrang berechnen zu können. Das Wärmeübertragungs-Modell baut auf Konzepte auf wie Zustandsgleichungen, Wärmekapazitäts-Modelle, Dichte-Modelle, Viskositäts-Modelle, dem Joule-Thomson Koeffizient und Wasser-Dichte- und Wasser-Oberflächenspannungs-Modelle.

Das Modellieren hat schlussendlich gezeigt, dass isolierte Förderstränge höhere Temperaturen und Drücke ermöglichen und dass diese Auswirkungen berechenbar sind für verschiedene Arten und Dicken von Isolierungen. Weiters führt der Temperaturanstieg zu höheren Gas-Geschwindigkeiten. Daher wird die kritische Gas-Geschwindigkeit leichter und für einen längeren Zeitraum von der tatsächlichen Gas-Geschwindigkeit überschritten und die Differenz zwischen den beiden ist stärker ausgeprägt. Dies ermöglicht eine höhere Produktionsrate und verlängert die Wirtschaftlichkeit einer Gasbohrung.

Table of Content

Page

List of Tables

List of Figures

Abbreviations

BHFP	Bottom Hole Flowing Pressure
BWR	Benedict-Webb-Rubin
CFM	Continuous Film Model
EDM	Entrained Droplet Model
EoS	Equation of State
GFK	Glass fiber reinforced plastic
HC	Hydrocarbons
HSE	Health, Safety and Environment
HTM	Heat Transfer Model
ID	Inner Diameter
IPR	Inflow Performance Relationship
JT	Joule-Thomson
OD	Outer Diameter
ppm	Parts per million
t.b.d.	To be determined
TPC	Tubing Performance Curve
WHFP	Wellhead Flowing Pressure

1 Introduction

Natural gas is one of the world's most important energy sources. The demand is continuously growing and in 2014, natural gas accounted for about a quarter of the the entire world energy consumption, as shown in Figure 1. [1, p. 42]

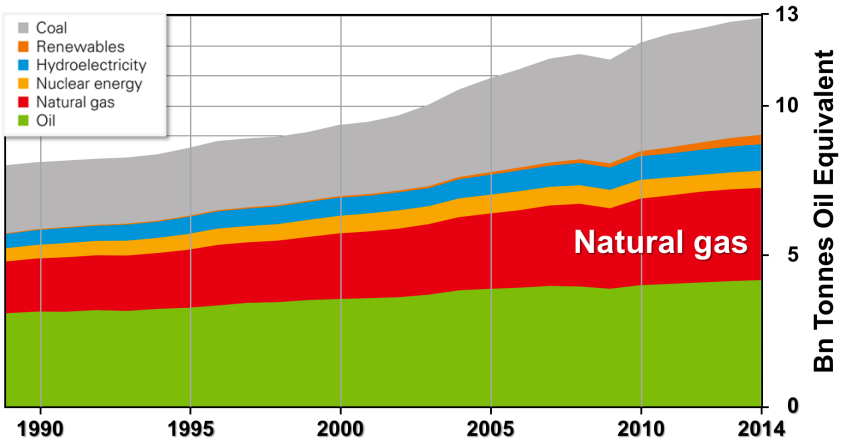

Figure 1: Worldwide Energy Consumption in 2014. [1, p. 42; modified]

The situation in Austria is very similar: about 22 % of the primary energy usage were supplied by natural gas in 2012. These 22 % are composed of about 5 % which were produced domestically and of 17 % which were imported, mainly from Russia and Norway. [2, pp. 6-7]

Thus, given this important status, a great deal could potentially be gained by having a closer look at how natural gas is produced and whether there is room for improvement in today's worldwide production practices.

1.1 Problem Statement

An area that traditionally has been neglected in the design of wellbore completions is the occurrence of heat loss from the media within the production tubing into the surrounding formation. Hydrocarbons are typically found in reservoirs which have a depth of several kilometers (Figure 2) and accordingly, exhibit pressures ranging from about 150 to 1000 bar und temperatures ranging from about 60 to 230 °C. During the production of these hydrocarbons to the surface, the surrounding rock formation (or, in the case of offshore production, the surrounding sea water) becomes considerably cooler than the media in the tubing string due to the temperature reduction associated with the geothermal gradient. If the tubing and the surrounding completion are not insulated, heat loss into the surrounding formation is facilitated.

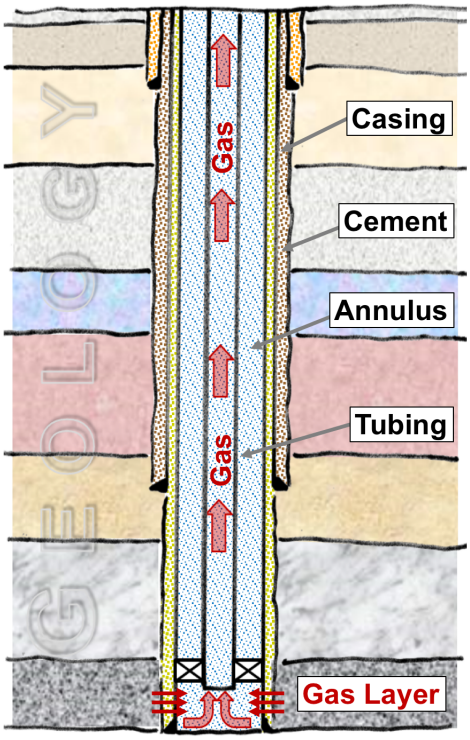

Figure 2: Schematic of a Gas Well. [3]

While surface facilities are usually built in such a way that heat losses are minimized, these heat preserving considerations are often not conveyed to the design of wellbore completions (such as casing and cement) and tubings (see Figure 2). This potentially represents large areas of improvement.

Since gas production is always accompanied by the presence of liquids, these heat preserving considerations should be heeded much more rigorously. Liquids may already be present in the reservoir or start to occur during production due to condensation. Other possible sources include water horizons, residuals from interventions, leaking packers and channelling behind the casing. [4]

The condensation process is caused by the decreasing temperature which occurs mostly due to the aforementioned heat loss into the formation (the Joule-Thomson effect is at work as well, see Chapter 3.3.5) and is ultimately facilitated by neglected insulating properties of the installed completion. Therefore, at the dew point of the gas, any decrease in temperature or increase in pressure will cause evaporated liquids to condense. Moreover, condensed water is low in total chlorides (less than 500 ppm) which can pose the additional problem of damaging formations containing swelling clays. [11]

Typical liquids are water or condensate; the latter is composed of liquefied higher hydrocarbons such as propane and butane. While at the beginning of gas production both of these liquids are being removed from the wellbore without further difficulty by being entrained in the gas stream, the inevitable decreases in tubing pressure and temperature have a negative impact on the removal abilities of the well.

As a result of these pressure and temperature decreases, the gas density decreases and the upward flow velocity of the natural gas in the production tubing continuously decreases as well. Once this upward velocity falls short of a certain so-called *critical gas velocity*, the gas stream loses its ability to carry the liquids all the way to the surface. Thus, liquids are not being removed from the wellbore any longer and they start to accumulate at the bottom of the well, creating a backpressure which is adversely affecting the production capacity of the reservoir (Figure 3). In the worst case, this liquid column can exert such an amount of backpressure that the gas well is effectively killed and production ceases. This happens when the remaining reservoir pressure is smaller than the backpressures caused by the liquid column, hydrostatic losses, friction losses and acceleration losses.

As an example, Figure 3 shows that after a continuous increase in surface water production, the water production rate starts to decline at a certain point (about 8 months). Also, the gas rate decreases and severe decline occurs. This means that the well is loading up and affecting the flowing capabilities of the well. Once the gas production stops after 12 months, no more lifting energy is supplied to the water in the wellbore and thus, production of gas and water ceases completely.

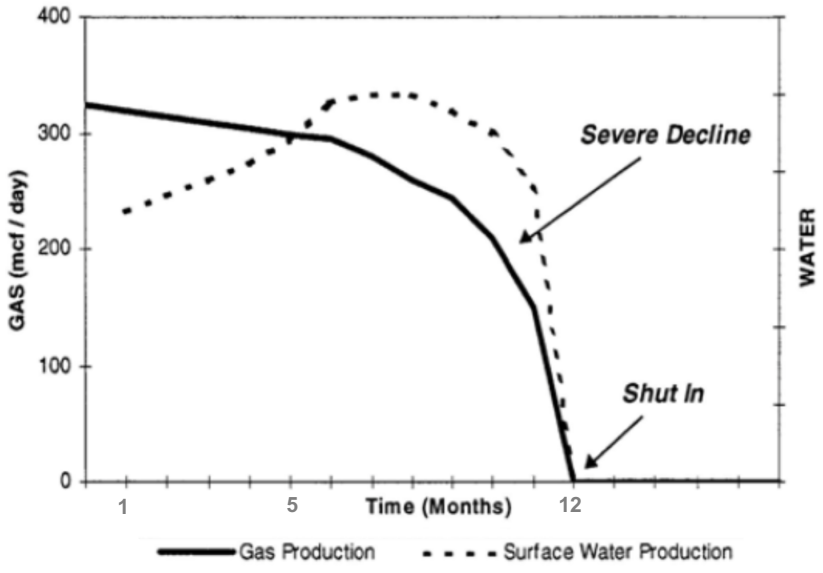

Figure 3: Typical Gas/Water Production Profile. [4]

This concept of *liquid loading* was formulated by Turner et al. [1969]. Based on the balance of the forces acting on a liquid droplet, they stated a formula which yields the required velocity for continuous liquid removal out of the wellbore: the aforementioned critical gas velocity. This formula consists of several parameters which ultimately are all dependent on the prevailing pressure and temperature conditions.

Thus, an improved conservation of heat within the tubing influences these parameters and would therefore also affect the gas velocity. This in turn could help in postponing the phenomenon of liquid loading and lead to an improved ultimate recovery factor of gas reservoirs. Moreover, the postponed occurrence of liquid loading would also delay the need for workover interventions.

This also contributes directly to the health, safety and environment (HSE) record of the operator by eliminating the need for or reducing the amount of workover interventions which always include a certain safety risk. Other problems associated with liquid loading are formation damages and increased corrosion. [4]

Figure 4 shows an example of the influence of liquid loading and the resulting need for liquid removal. On three occasions, the gas production stopped due to liquid loading. As counter-measures, a plunger lift system, compression and gas recirculation had to be installed. If possible, it would be desirable to be able to forgo these costly and potentially hazardous measures by preventing or delaying liquid loading.

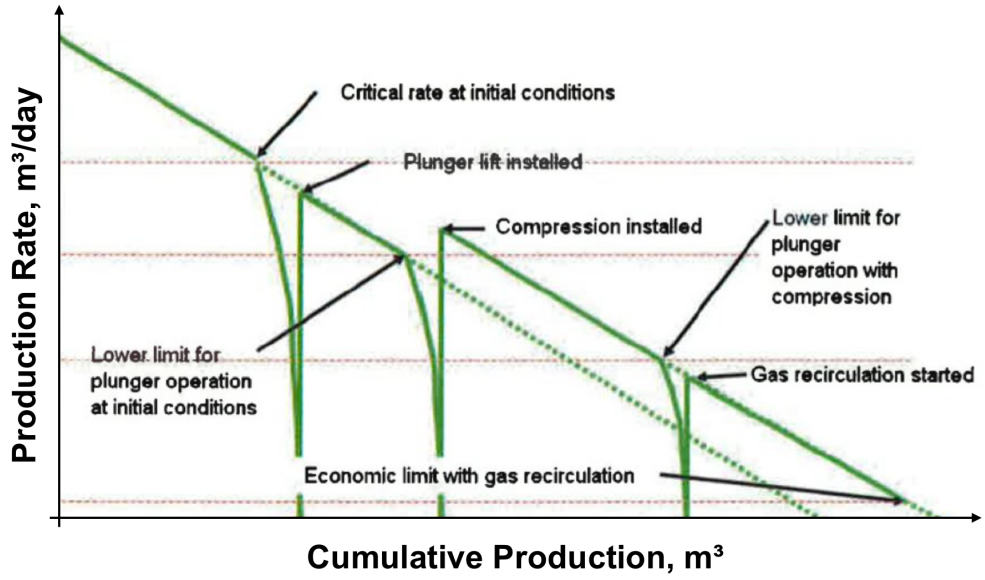

Figure 4: Production Behaviour of a Gas Well with Liquid Loading. [4]

Well-established indications for the onset of liquid loading are e.g. stop of liquid production, erratic gas production behaviour, significant pressure changes in gradient curves and increasing differences in tubing and casing pressure. Possible deliquification techniques include installing a velocity string; installing artificial lift methods that can be adapted to the removal of relatively small amounts of unwanted liquids (such as gas lift); using surfactants to decrease the droplet's surface tension; adopting intermittent production with a plunger lift system (Figure 5); increasing the gas rate; removing unnecessary bottlenecks; and heating the tubing. [4]

It is worth mentioning that artificial lift methods and deliquification methods might seem similar, yet are profoundly different in that the first is designed to get the desired product to the surface, while the latter is only concerned with getting liquids out of the way. As an example, evaporation by a significant reduction of wellhead pressure is an additional efficient deliquification technique which is unacceptable for artificial lift, however. [5]

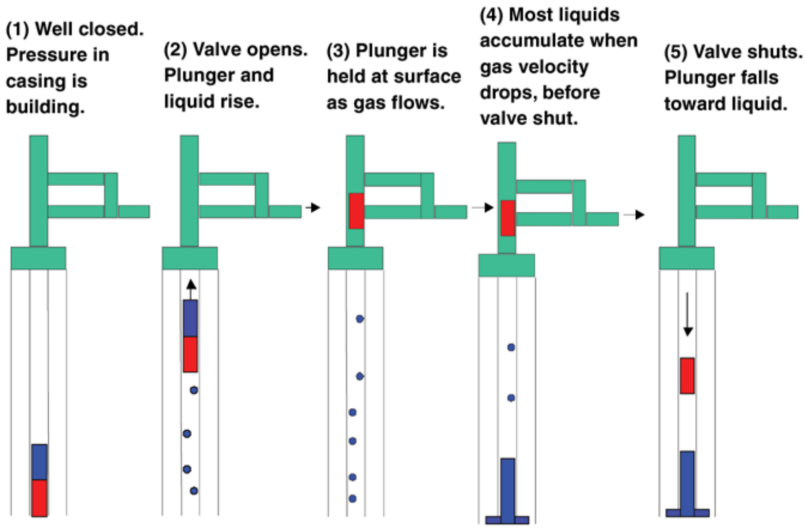

Figure 5: Simplified Illustration of the Working Principle of a Plunger Lift System. [13]

Another possibility is the previously mentioned reduction of the wellhead pressure which on one hand evaporates liquids, increases the flow rate and improves liquid lift capabilities but on the other hand creates the need for compressor stations to meet the pressure requirements of the sales line. [7, p. 60]

2 Literature Review

Following the publication of the paper by Turner et al. [1969], a multitude of authors used it as a starting point for their own investigations. This chapter aims to give an overview of the original work, additional findings and the contributions of the respective authors.

2.1 Turner et al. [1969]

Turner et al. [1969] tackled the issue of liquid loading by trying to analyse the involved parameters and to find a formula to predict the minimal flow rate required for a continuous removal of liquids. In their study, they examined two different models which account for the upward transport of liquids: the Continuous Film Model (CFM) and the Entrained Droplet Model (EDM).

The Continuous Film Model deals with liquid phases that accumulate on the surface of the tubing and are being moved upward due to the shear force of the gas acting on the liquid film. The main interest is finding the minimum gas rate that is needed to provide enough lift to the film to prevent a gas well from loading up. The approach used by Turner et al. [1969] follows Hewitt [1961] and his analysis of Dukler's [1960] work. The forces at work are the interfacial shear between the moving gas and the liquid adhering to the tubing, counteracted by gravity and friction (see Appendix A). However, after tests with independent field data from gas wells that produced liquids were completed, the forecasts of the continuous film model did not show a good match with this data. In some cases, while the wells were in fact unloading liquids, the film model falsely predicted the gas rates as being too low. Moreover, the theoretical framework behind the film model suggests dependency on the gas liquid ratio of the well. Turner et al. [1969] therefore drew the conclusion that the continuous film model is not the commanding mechanism for liquid unloading. Finally, a downward moving liquid film starts to thicken at certain points due to the countercurrently moving gas and forms a bridge across the tubing. The breakdown of this bridge then causes the formation of entrained droplets which require an entirely different transport mechanism, namely the EDM.

The Entrained Droplet Model is based on the occurrence of liquid drops within the gas stream. In other words, a liquid drop is falling under its own weight through a fluid until it reaches its terminal velocity. This terminal, or threshold, velocity can be expressed as the maximum velocity the droplet can reach due to the force of gravity, while simultaneously being counteracted by the drag force and the buoyancy force (as is shown in Figure 6).

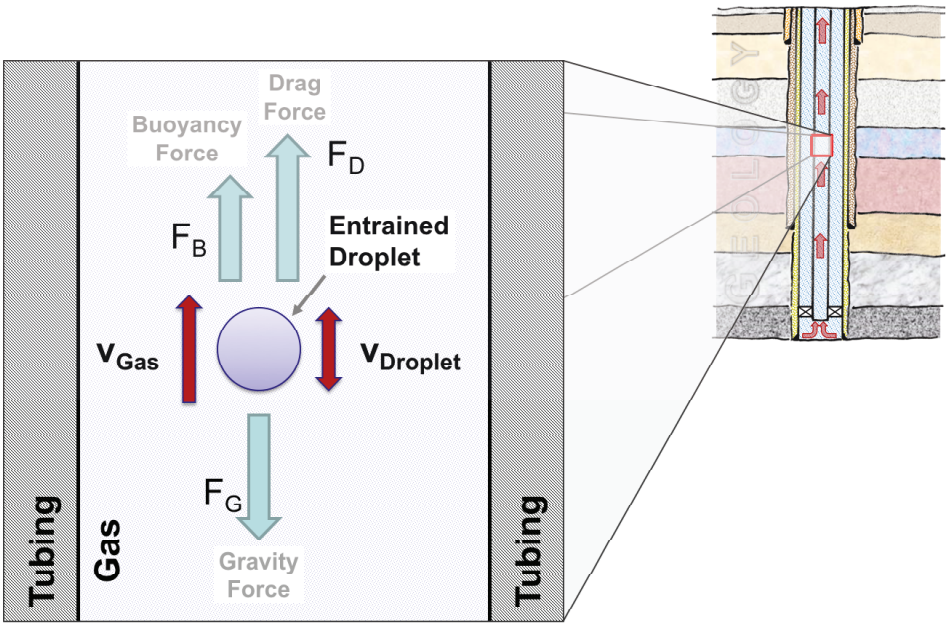

Figure 6: Forces at Work in the Entrained Droplet Model. [3]

The gravity force F_G acting on a spherical object can be expressed as

$$F_G = \rho_L \, g \, V = \rho_L \, g \, \frac{\pi d_d^3}{6} \tag{1}$$

while the drag force F_D is

$$F_D = \frac{1}{2} \, c_D \, A_d \, \rho_G \, v^2 = \frac{1}{2} \, c_D \, \frac{\pi d_d^2}{4} \, \rho_G \, v^2 \tag{2}$$

and the buoyancy force F_B is determined as follows:

$$F_B = \rho_G \, g \, V = \rho_G \, g \, \frac{\pi d_d^3}{6} \tag{3}$$

Combining equations (1), (2) and (3) as a balance of forces yields

$$F_G = F_D + F_B \tag{4}$$

$$F_G - F_B = F_D$$

$$(\rho_L - \rho_G) \, g \, \frac{\pi d_d^3}{6} = \frac{1}{2} \, c_D \, \frac{\pi d_d^2}{4} \, \rho_G \, v^2$$

Solving the last form of Eq.(4) for v results in the so-called threshold velocity

$$v^2 = \frac{4 \, g \, d_d \, (\rho_L - \rho_G)}{3 \, c_D \, \rho_G} \tag{5}$$

To account for the influence of velocity and surface tension, the Weber number is introduced in Eq.(6); the concept of the Weber number is further discussed in Chapter 2.8.

$$We = \frac{\rho_G \, d_d \, v^2}{\sigma_L} \tag{6}$$

The unknown diameter d_d of the entrained droplets as used in Eq.(5) is then substituted by re-arranging the Weber number to give d_d.

$$d_d = \frac{\sigma_L \, We}{\rho_G \, v^2} \tag{7}$$

After the re-arrangement, the formula for the critical velocity to lift droplets in vertical wells is obtained as

$$v_c = \left[\frac{4 \, g \, \sigma_L \, We_c \, (\rho_L - \rho_G)}{3 \, c_D \, \rho_G^2}\right]^{1/4} \tag{8}$$

In order to guarantee liquid removal, the actual gas velocity in the tubing may never fall short of this critical velocity. The recently introduced parameter We_c will be discussed in Chapter 2.8. As a next step, Turner et al. [1969] went on in an attempt to simplify this equation by substituting four of the five parameters with adequate average values for both cases, water and condensate, using the following assumptions:

- drag coefficient, c_D= 0.44
- surface tension of water, σ_W = 60 dyn/cm = 0.06 N/m
- surface tension of condensate, σ_C = 20 dyn/cm = 0.02 N/m
- density of water, ρ_W = 67 lb/ft^3 = 1073 kg/m^3
- density of condensate, ρ_C = 45 lb/ft^3 = 721 kg/m^3
- critical Weber number, We_c = 30

The gas density which is a function of pressure, temperature and gas gravity was also simplified. They determined that pressure variations have a larger effect than variations in temperature or gas gravity, and subsequently used average values for these two less influential parameters as well:

- specific gravity of gas, γ_G = 0.6
- temperature of gas, T_G = 120 °F = 49 °C

Finally, after substituting all these parameters from Eq.(8) with the mentioned constants, they arrived at two simplified critical velocity equations for water ($v_{c,w}$) and for condensate ($v_{c,c}$) with both only being a function of pressure.

$$v_{c,w} = \frac{5.62(67-0.0031\,p)^{1/4}}{(0.0031\,p)^{1/2}}\ [\mathrm{ft/sec}];\ p \text{ in psi} \tag{9}$$

$$v_{c,c} = \frac{4.02(45-0.0031\,p)^{1/4}}{(0.0031\,p)^{1/2}}\ [\mathrm{ft/sec}];\ p \text{ in psi} \tag{10}$$

The numeric values in these two equations also include an upward adjustment of approximately 20 %. This is due to the fact that Turner et al. [1969] compared field data with the calculation results of their model and found that this modification is necessary to achieve a better match for the calculated minima and to ensure the removal of all drops. They based this change on Figure 7 which is constructed in such a way that if the minimum calculated flow rate equals the actual flow rate of the test well, it will plot on the diagonal. The axes of Figure 7 plot the test flowrate of gas versus the calculated minimum flowrate of gas.

If the model is representative, all wells with near-load up conditions (circles on the graph) should plot near the diagonal. Wells that unload easily (squares) should plot above the diagonal and wells that don't unload (triangles) should plot below. Based on these results, they adjusted the diagonal straight line upwards by 20 % to the dashed line. [8]

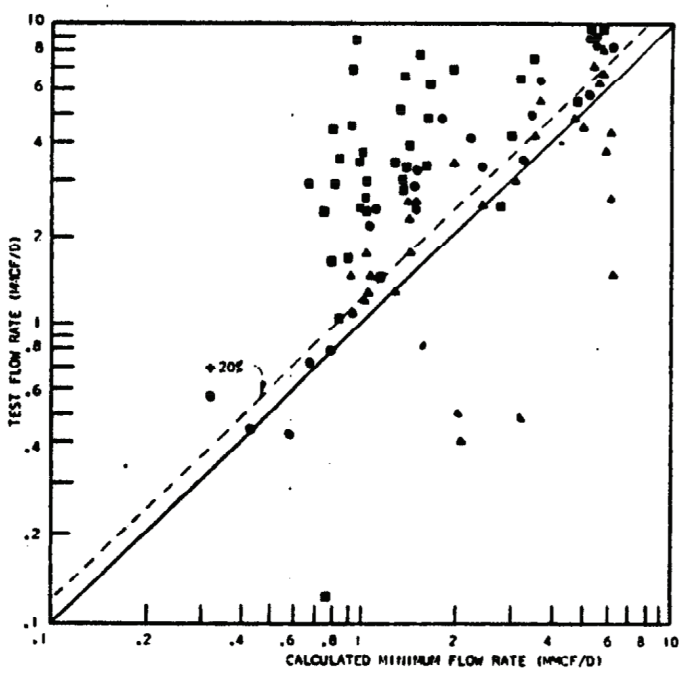

Figure 7: Entrained Droplet Model after Turner et al. [1969]. [8]

In their conclusion, they also note that these equations are not limited to tubings but can be applied for similar flow geometries also and that if both kinds of liquid are present, the properties of the denser liquid should be used. This should done to ensure liquid removal no matter whether the occuring liquid is (lighter) condensate or (heavier) water.

Moreover, since gas wells are usually thought of in terms of production rates, equations (9) and (10) can also be converted into *critical gas flow rates*. A volumetric flow rate may be computed as

$$q_c = \frac{3.067\ p\ v_c\ A}{(T+460)z}\ [\mathrm{MMscf/day}];\ p \text{ in psi; } A \text{ in ft}^2,\ T \text{ in °F} \tag{11}$$

Replacing the critical velocity in Eq.(11) with both $v_{c,w}$ and $v_{c,c}$ leads to

$$q_{c,w} = \frac{17.24\ p\ A}{(T+460)z} * \frac{(67-0.0031\ p)^{1/4}}{(0.0031\ p)^{1/2}}\ [\mathrm{MMscf/day}];\ p \text{ in psi; } A \text{ in ft}^2,\ T \text{ in °F} \tag{12}$$

$$q_{c,c} = \frac{12.33\ p\ A}{(T+460)z} * \frac{(45-0.0031\ p)^{1/4}}{(0.0031\ p)^{1/2}}\ [\mathrm{MMscf/day}];\ p \text{ in psi; } A \text{ in ft}^2,\ T \text{ in °F} \tag{13}$$

2.2 Coleman et al. [1991]

Coleman et al. [1991] took a closer look at the concept which was presented by Turner et al. [1969]. They examined the data used by Turner et al. [1969] and stated that the data they had used mostly consisted of wells with a wellhead flowing pressure larger than 500 psi (about 34 bar). As liquid loading mostly aggravates once the remaining pressure in the reservoir continuously declines, Coleman et al. [1991] decided to focus on wells that experience the phenomenon of liquid load-up and also have a wellhead flowing pressure (WHFP) below 500 psi.

For this, they used two separate sources of field data. In one test for 17 wells which flowed at a stable rate above their critical flow rate q_c, the WHFP was gradually increased until the wells started to show typical signs for the beginning of liquid loading (i.e. an exponential decline in production rate).

The second source were production charts of 39 wells which were searched for comparable tendencies of declining rates. Here, the onset of liquid loading was determined by interpreting the corresponding rates and the wellhead flowing pressure for each well using 8-day L-10 production charts as seen in Figure 8.

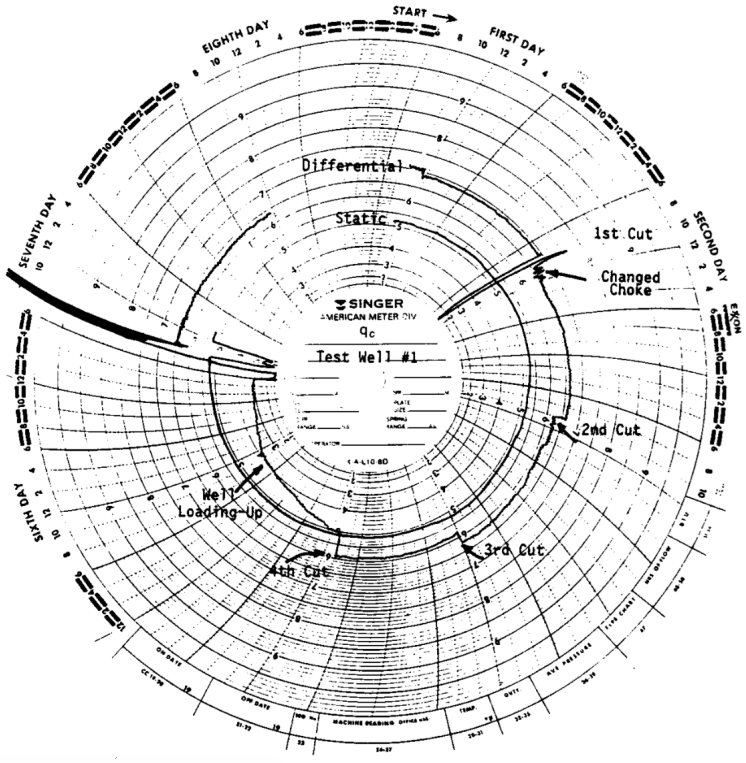

Figure 8: 8-day L-10 Production Chart of a Gas Well. [11]

When Coleman et al. [1991] plotted this data (Figure 9), they found that it matched Turner et al.'s [1969] predictions better without the 20 % upward adjustment and drew six conclusions from this result. First, they concur with the assumption that in most cases the WHFP has a controlling influence on the beginning of liquid loading. Secondly, they revealed that in some tests the WHFP had to be increased significantly to force load-up. Thirdly, wells that exhibitied slugging behaviour plotted well below the theoretical line and should be considered anomalies. Fourthly, the liquid to gas ratio ranged from 1 to 22.5 bbl/MMscf and in this analysis, it did not have any effect concerning liquid load-up. This means that the amount of liquid which is present in the tubing does not influence the onset of liquid loading, only the gas flow rate does; a finding that is consistent with Turner et al.'s [1969] results. Fifth, in most cases the main source of loading fluid was condensed water; A finding that significantly strengthens the postulation that heat losses into the formation during production should be minimized as vigorously as possible.

And finally, as their sixth finding, Coleman et al. [1991] observed during the utilisation of three-phase separators a complete stop in liquid production once the well went into load-up behaviour. The reason for this is that the critical velocity was equal or larger than the actual gas velocity and thus, the liquid droplets were being held up in the tubing string.

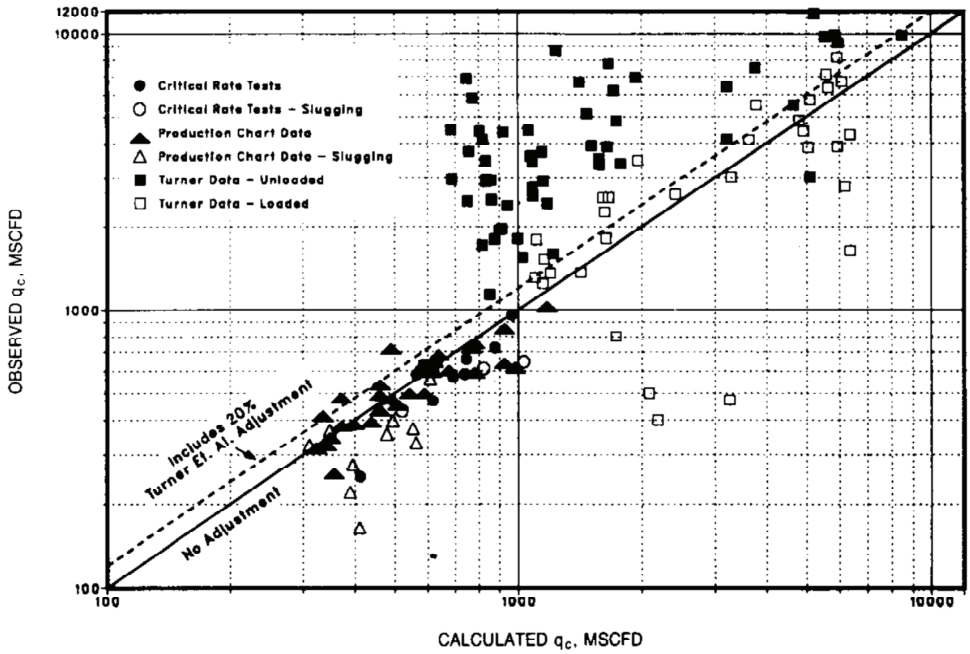

Figure 9: Plot of Data Points comparing Observed and Calculated Critical Rates. [11]

In their conclusion, they emphasize that the 20 % upward adjustment is not required for wells with a WHFP of less than 500 psi, that the primary source of load fluid is condensed water and that the largest-diameter segment should be used for calculations.

2.3 Nosseir et al. [1997]

In their paper, Nosseir et al. [1997] pointed out that the equation put forth by Turner et al. [1969] required empirical adjustment by 20 % with different data ranges, while Coleman et al. [1991] found that no such adjustment is necessary. Nosseir et al. [1997] presented a new approach that takes the influence of flow regimes into account in order to find the underlying causes for these discrepancies. [57]

The flow regime affects the magnitude of the drag coefficient and and determines which drag coefficient equation is representative under the given cirumstances. Nosseir et al. [1997] discuss analytical equations for three different flow conditions. [57]

The first is the laminar flow regime for $\mathrm{Re} < 1$. In this scenario, the drag coefficient can be expressed by

$$c_D = \frac{24\,\mu}{d_d v_G \rho_L} \tag{14}$$

The second is the transition flow regime which is in the range of 1 < Re < 1000, described by

$$c_D = \frac{30}{\mathrm{Re}^{0.625}} \tag{15}$$

Thirdly, the following equation can be used for fully developed turbulences with Re reaching up to 200,000, where the drag coefficient is reasonably constant. This drag coefficient value from Eq.(16) is the one used by Turner et al. [1969].

$$c_D = 0.44 \tag{16}$$

In their research, Nosseir et al. [1997] evaluated the Reynolds numbers for the data used by Turner et al. [1969] and by Coleman et al. [1991] to determine why they came to different conclusions concerning an upward adjustment. Nosseir et al. [1997] found that Turner et al.'s [1969] data has Reynolds values ranging from $2*10^5 < \mathrm{Re} < 10^6$ (resulting in drag coefficients of about 0.2), while Coleman et al.'s [1991] data is in the lower range of $10^4 < \mathrm{Re} < 2*10^5$ (resulting in drag coefficients of about 0.44). Therefore, for the data set used by Coleman et al. [1991], a good match was achieved and no adjustment required. [57]

With these results, Nosseir et al. [1997] decided to develop two models, one for transition flow regimes

$$v_c = 14.6 \frac{{\sigma_L}^{0.35}(\rho_L - \rho_G)^{0.21}}{{\mu_G}^{0.134}{\rho_G}^{0.426}} \tag{17}$$

and one for highly turbulent flow regimes

$$v_c = 21.3 \frac{{\sigma_L}^{0.25}(\rho_L - \rho_G)^{0.25}}{{\rho_G}^{0.5}} \tag{18}$$

Eq.(18) is very similar to Turner et al.'s [1969] equation after adjustment where they determined the coefficient to be 20.4 instead of 21.3. According to Nosseir et al. [1997], this shows that Turner et al.'s [1969] equation tries to match different ranges of actual data and it also explains why Coleman et al. [1991] did not need the 20 % adjustment.

Ignoring the influence of flow regimes on the drag coefficient turned out to be the cause for this mismatch. The new approach by Nosseir et al. [1997] improves the match quality, honors the prevailing flow regime and provides a better physical explanation. [57]

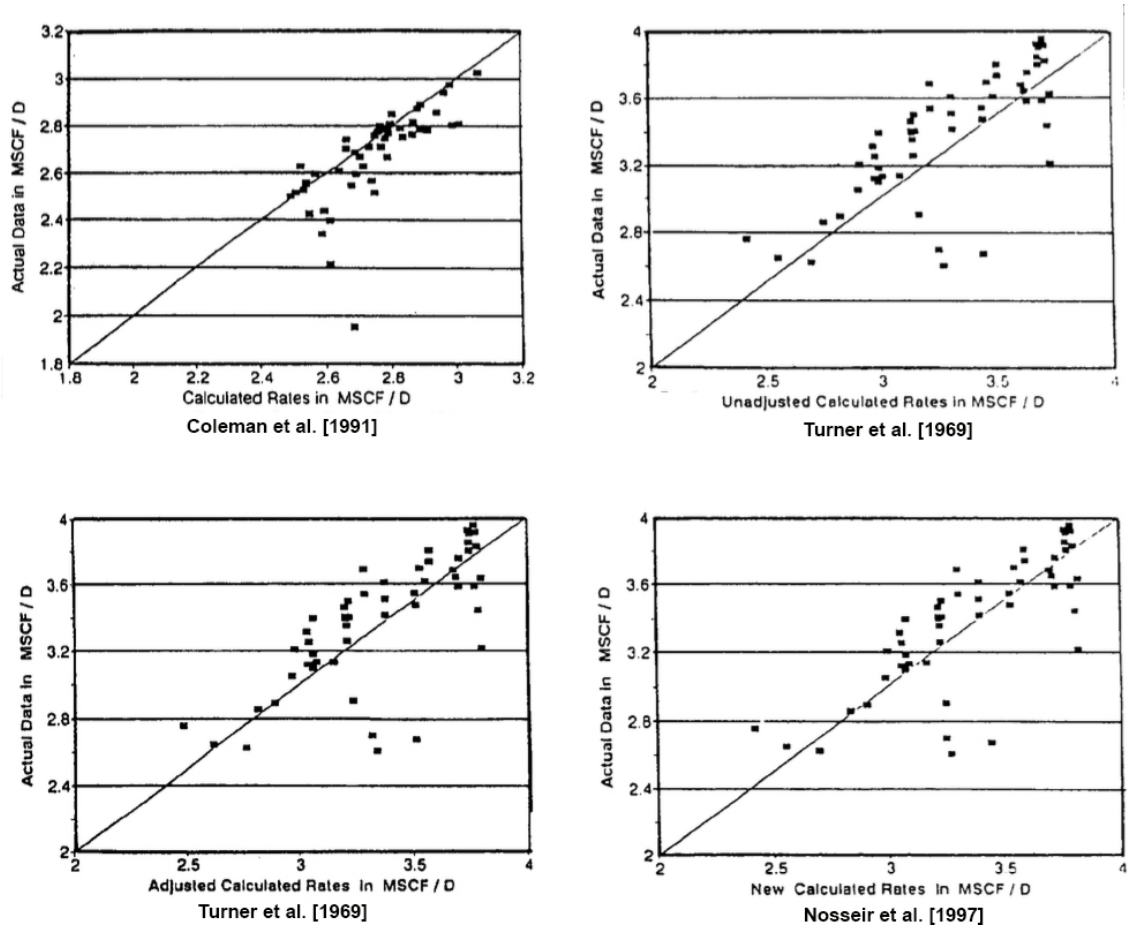

Figure 10: Comparison between four different Calculation Models. [57, modified]

As Figure 10 shows, the data used by Coleman et al. [1991] shows a good fit with the (unadjusted) Coleman et al. [1991] formula. For Coleman et al. [1991] themselves, their unadjusted model is rather unaccurate which is improved by the upward correction of 20 %. The model by Nosseir et al. [1997] which uses the appropriate equation depending on the flow regime shows an even further improvement in match quality.

2.4 Li et al. [2002]

According to Li et al. [2002], many gas wells in China produce at rates which are lower than the minimum flow rates necessary to prevent liquid loading as determined by Turner et al.'s [1969] equation. The engineers responsible for these wells found that reducing the required critical rate by two-thirds yielded more accurate results. Thus, Li et al. [2002] set out to find the underlying causes for this apparent mismatch and they started to examine the deformation falling droplets experience due to the forces acting on the droplet. These forces cause the change from a spherical shape to a flat shape (Figure 11).

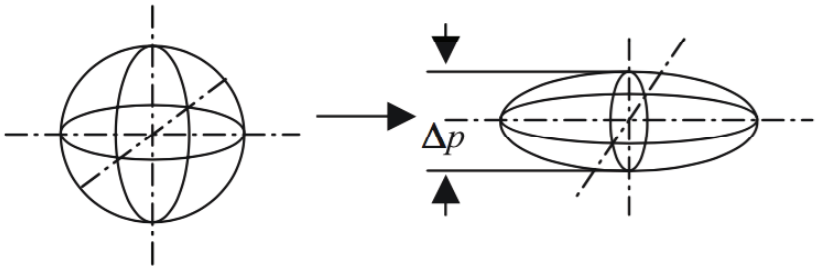

Figure 11: Spherical Drop (left side) being deformed into a Flattened Shape (right side) in a High-Velocity Gas Stream due to pressure differences. [12]

This deformation of the droplet which occurs in high-velocity gas streams can be explained by pressure differences which manifest themselves between the fore portion and the aft portion of a droplet. Thus, the spherical drop is forced into a convex beam as shown in Figure 11. Since a spherical form has a smaller surface area that can be engaged by the gas stream than a flattened shape, a higher critical flow velocity is needed to lift the droplet to surface. Conversely, the flattened droplet displays a larger efficient area and lower flow velocities are sufficient to transport the drop upwards.

Therefore, Li et al. [2002] took the fact that critical rates determined with the Turner et al. [1969] equation are much larger than the actual rates of their reference wells as a hint that entrained liquid droplets are flattened.

Li et al. [2002] derived their critical velocity to be

$$v_c = 2.5 \left[\frac{\sigma_L \, (\rho_L - \rho_G)}{\rho_G^2} \right]^{1/4} \tag{19}$$

To arrive at this simplification, they used a drag coefficient of 1.00 for the Reynolds number range of 10^4 to 10^5 for a flattened sphere (see Chapter 2.8 for further details). The critical rate then is

$$q_c = 2.5 * 10^5 \left(\frac{p \, v_c \, A}{T \, z} \right); \; p \text{ in kPa} \tag{20}$$

When comparing their model with Turner et al. [1969], Li et al. [2002] emphasize the large difference between the coefficients which are 6.6 and 2.5, respectively (Figure 12). This is the reason for the critical velocities determined by Li et al. [2002] being significantly smaller than those calculated by Turner et al. [1969].

	Turner et al. [1969]	Li et al. [2002]
Drop shape	Spherical	Flat
Drag coefficient, C_D	≈0.44	≈1.0
Terminal velocity formula	$v_t = 6.6 \sqrt[4]{\frac{(\rho_L - \rho_g)}{g^2}}$	$v_t = 2.5 \sqrt[4]{\frac{(\rho_L - \rho_g)}{g}}$

Figure 12: Comparison of the Coefficients by Turner et al. [1969] and Li et al. [2002]. [12]

They then proceeded to test their formula on 16 wells, and subsequently to compare it to Turner et al.'s [1969] formula as well. Figure 13 is set up in such a way that the datum points will plot on the diagonal if the well's actual flow rate matches the critical flow rate (squares). If the actual flow rate is lower and liquid loading occurs (triangles), the points will plot below; if the flow rate is larger than the critical rate, the points should be located above the diagonal (rhombi). As is suggested in Figure 13, the model of Li et al. [2002] on the left side appears to yield much better results than Turner et al.'s [1969] model on the right side.

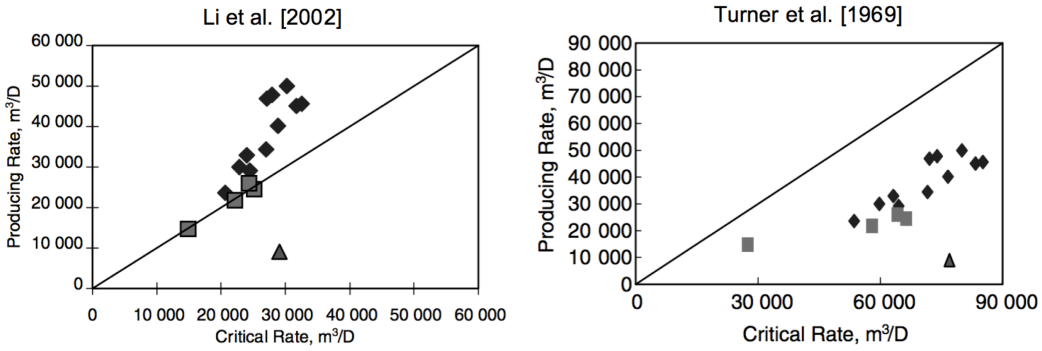

Figure 13: Comparison of Li et al.'s [2002] model and Turner et al.'s [1969] model. [12]

2.5 Lea and Nickens [2004]

Lea and Nickens [2004] start by discussing the total flowing-pressure drop which can be expressed as the sum of friction, acceleration and elevation pressure losses. For gas wells with low production rates, the friction and acceleration terms are likely to be small.

However, the elevation, or gravity, term increases with liquid loading and can reach unfavorable dimensions. They also discuss the influence of the prevailing flow regimes. The flow regimes are a function of superficial gas and liquid velocities (see Chapter 3.5), and Lea and Nickens [2004] used Figure 14 to illustrate this parameter:

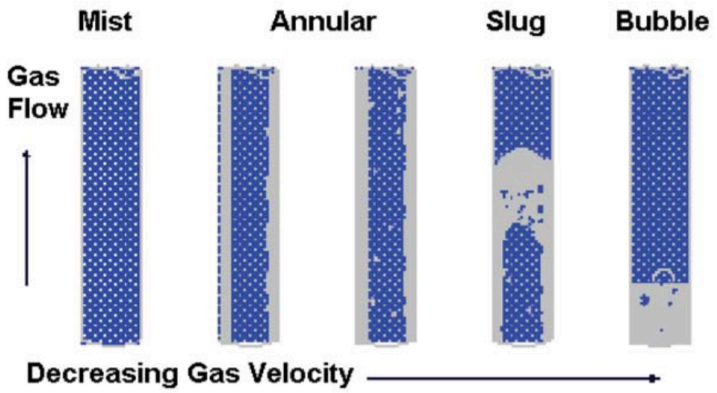

Figure 14: Flow Regime Chart. [7]

During mist flow, the well may experience only a slight increase in pressure drop. With decreasing gas velocity, however, the flow becomes more sluggish and finally reaches bubble flow. At this stage, a large fraction of the wellbore is filled with liquid and the production capability of the reservoir is hindered significantly.

Thus, it is highly advisable to try to stay in mist flow. Lea and Nickens [2004] list several ways to achieve this. They recommend creating a lower wellhead pressure, increasing the flow velocity by using a smaller tubing, getting the liquids out via the use of pump or gas lift and the sealing off of water zones.

To detect liquid loading, Lea and Nickens [2004] propose to closely observe the behaviour of the decline. As seen in Figure 15, sharp drops usually are a clear indication for liquid loading. Other symptoms include liquid slugs arriving at the surface and sharp gradient changes on a flowing-pressure survey.

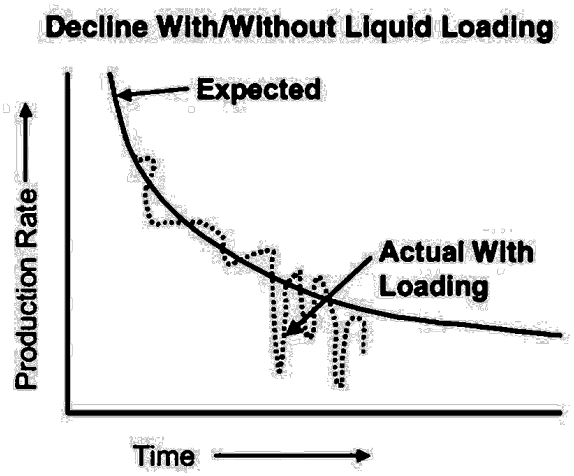

Figure 15: Decline Curve with and without Liquid Loading. [13]

An analysis method that can be applied is the investigation of the inflow performance relationship curve (IPR curve) and the tubing performance curve (TPC) for different tubing diameters (D_1-D_3), as seen in Figure 16. The flowing pressure needed by the TPC for varying production rates is composed of the tubing-pressure drop and the tubing flowing pressure. The required pressure increases at low production rates due to liquid loading and also at high production rates, in this case due to friction.

The intersection of the IPR curve and the TPC then predicts the flow rate. From the two intersections, the intersection with the higher rate is the stable one. As seen in Figure 16, the tubing diameter has a significant impact on the TPC. Since D_1 is too large and D_3 has high friction, D_2 may be considered as the best choice.

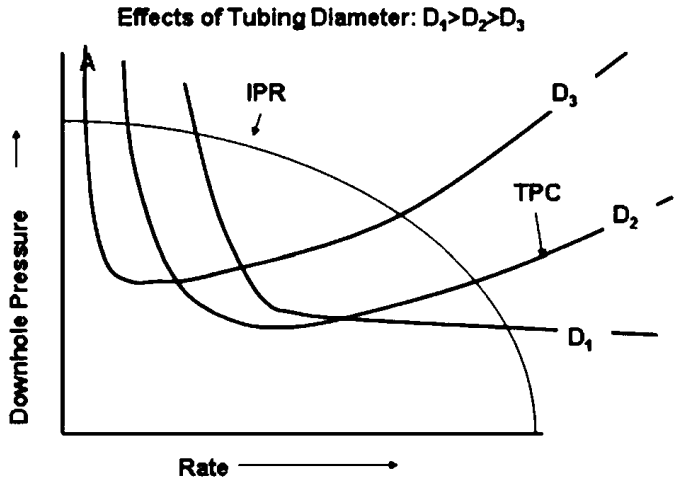

Figure 16: Inflow Performance Relationship (IPR) vs. Tubing Performance Curve (TPC) for three different Tubing Diameters. [13]

2.6 Luan and He [2012]

Luan and He [2012] wanted to calculate minimum required flow rates for low-pressure gas wells and based their approach on the combination of the concepts of Turner et al. [1969] and Li et al. [2002]. They state that while Turner et al.'s [1969] model (including the 20 % upward adjustment) generally overestimates the probability of liquid occurrence, Li et al.'s [2002] model tends to underestimate the liquid loading occurrence. Thus, they assume that the actual critical flow rate of low-pressure wells is found between the results of these two models (see Figure 17). The approach by Luan and He [2012] seeks to combine these models and fine-tune it by accounting for the changes of gas-lifting efficiency caused by droplet rollover during the ascent within the tubing.

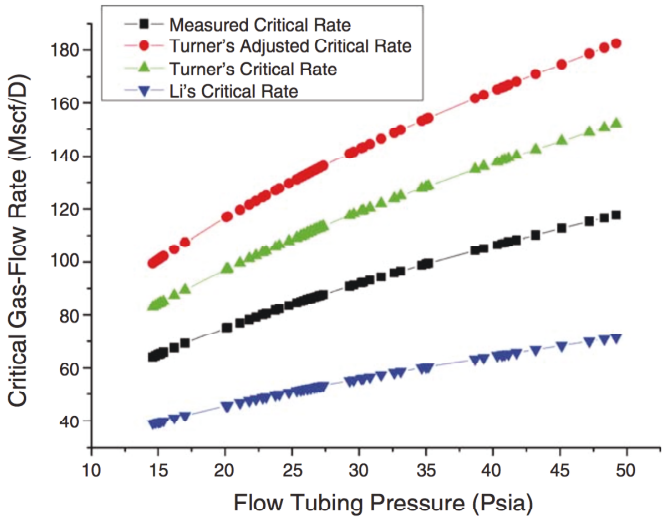

Figure 17: Comparison of Critical Flow Rates. [14]

They further argue that the reason for Turner et al.'s [1969] ineptitude towards low-pressure gas wells stems from the fact that it does not honor the deformation of the entrained droplets. In Li et al.'s [2002] model, they assume that part of the gas-lifting energy is wasted due to rolling-over droplets which influences the effective surface area. Therefore, the model of Luan and He [2012] acknowledges both the influence of deformed droplets and the changes in gas-lifting energy.

The gas-lifting efficiency losses due to droplet-rollover are quantified by introducing a dimensionless variable, the loss factor S. The loss factor ranges from zero to one and the larger it is, the closer the calculated results are to those of Turner et al.'s [1969] model. If the factor is equal to zero, the new model concurs with Li et al.'s [2002] calculations. The new model can be represented by Eq.(21).

$$v_{crit-S} = v_{crit-L} + S(v_{crit-T} - v_{crit-L}) \tag{21}$$

The magnitude of S was obtained by fitting the calculated results to the production data of more than 300 gas wells. After finding the range to be 0.75 to 0.83, they decided to use the upper limit of 0.83. With this, they were able to match the calculated minimum flow rates more closely to the actual minimum flow rates where the wells started to show signs of liquid loading than Turner et al. [1969] and Li et al. [2002] could.

This was also confirmed by an error analysis which found the new model to be more accurate than Turner et al.'s [1969] and Li et al.'s [2002] models. However, they emphasized that Turner

et al.'s [1969] results are very close to theirs and thus name this to be the reason why Turner et al.'s [1969] Entrained Droplet Model is widely accepted.

Luan and He [2012] conclude that although theoretically convincing, proof of flat-shaped droplets in high-pressure wells has yet to be found and they recommend to use their new model for low-pressure gas wells with less than 500 psia.

2.7 Li et al. [2014]

In this paper by Li et al. [2014], the influence of deviated or horizontal wells on liquid loading is investigated. To this end, they added the pipe angle α to account for the deviation from the vertical axis (Figure 18).

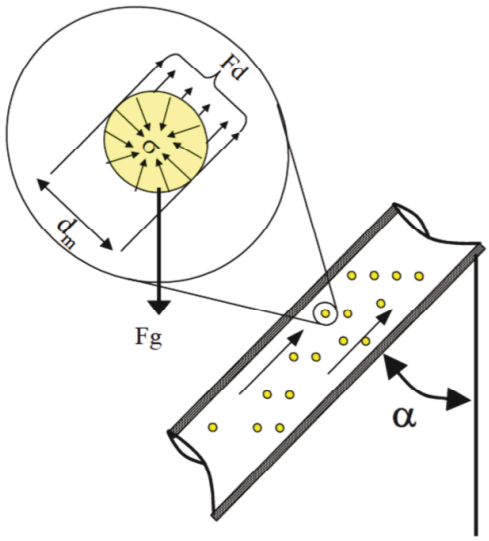

Figure 18: Pipe Deviated by Angle α from the Vertical Axis. [15]

As a result, the critical gas velocity according to Li et al. [2014] is

$$v_c = \left[\frac{4\, g\, \sigma_L\, We_c\, (\rho_L - \rho_G)}{3\, C_D\, \rho_G^2 \cos(\alpha)}\right]^{1/4} \tag{22}$$

They also cite the results of several other investigators, mentioning that liquid film reversal starts at the onset of liquid loading. While the liquid film (U_{film}) near the gas core (U_{gas}) still flows upwards, the film near the pipe wall (U_{wave}) may already be on its way downhole as shown in Figure 19.

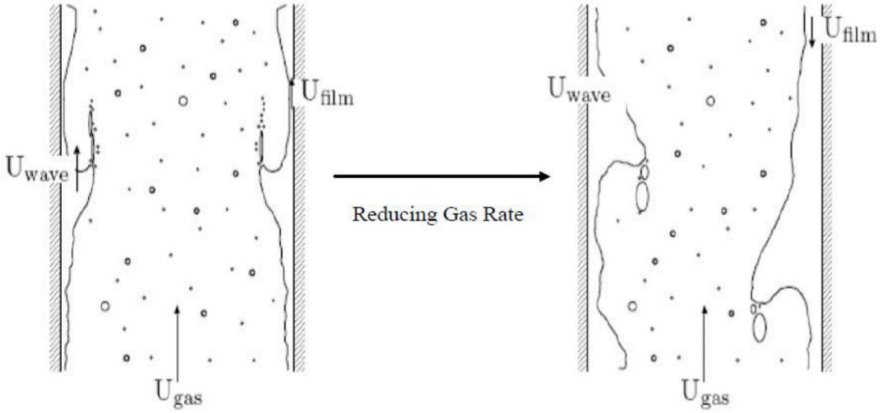

Figure 19: Flow Reversal of the Liquid Film Adhering to the Tubing Wall. [15]

Moreover, the influence of deviation angles on the critical gas velocity was explored as well. The critical velocity increases up to a deviation of 60° and then decreases while the deviation increases to 90° (Figure 20).

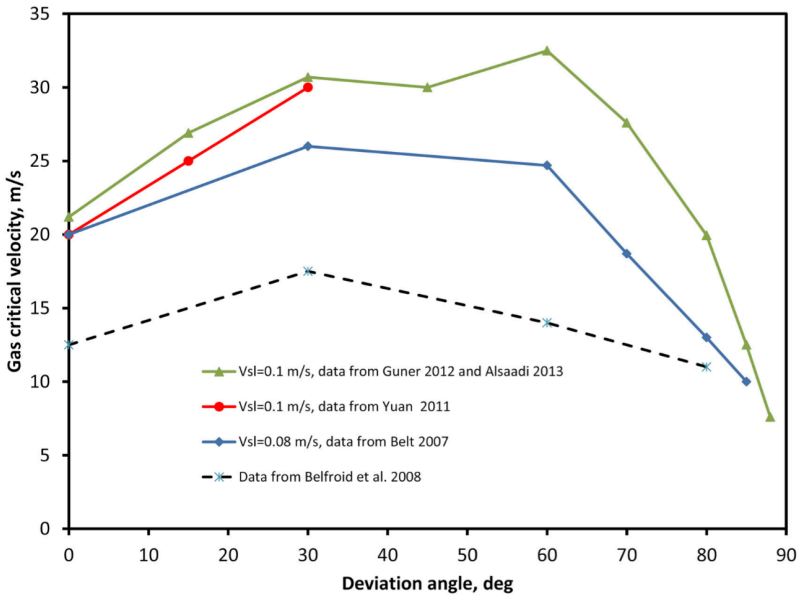

Figure 20: Influence of Deviation Angles on the Critical Gas Velocity. [15]

The result of Li et al.'s [2014] work is a two-variable curve-fit model to predict the critical gas rate based on the deviation angle and the liquid superficial velocity. As a limitation, they note that the simulation was performed with air-water tests under atmospheric pressure. Moreover, in this work, the focus will lie on the Entrained Droplet Model including the deviation angle as proposed by Li et al. [2014] in Eq.(22).

2.8 Dimensionless Quantities

In this chapter, the basic concepts behind several dimensionless quantities of importance are discussed and illustrated.

2.8.1 Reynolds Number

The Reynolds number is defined as the ratio of inertial forces to viscous forces.

$$\mathrm{Re} = \frac{\mathrm{nert\ al\ forces}}{\mathrm{v\ scous\ forces}} = \frac{\rho\ \mathrm{v}\ \mathrm{L}}{\mu} \tag{23}$$

For pipes, the characteristic length L is the hydraulic diameter of the pipe, $\mathrm{d_H}$. When calculating the Reynolds number for production tubings, the hydraulic diameter is simply the inside diameter of the tubing.

To calculate the hydraulic diameter $\mathrm{d_H}$ for an annulus, the hydraulic diameter is determined as inner diameter (ID) of outside pipe minus the outer diameter (OD) of the inside pipe.

$$\mathrm{d_{H,annulus}} = \mathrm{ID_{outside\ pipe}} - \mathrm{OD_{inside\ pipe}} \tag{24}$$

The magnitude of the Reynolds number allows an estimate of the prevailing flowing conditions under the given circumstances. It is difficult to determine strict boundary values to distinguish between laminar and turbulent flow, but certain guidelines exist. Laminar flow is usually thought possible with $\mathrm{Re} < 2100$ and turbulent flow starts at $\mathrm{Re} > 4000$. The range from 2100 to 4000 is usually referred to as transition zone where both flow types are possible and can coexist with each other. [16, p. 207]

The Reynolds number is used to estimate other important parameters, such as the friction factor (Figure 21 and Figure 22 in Chapter 2.8.2) and the drag coefficient (Figure 23 in Chapter 2.8.3).

2.8.2 Friction Factor

The friction factor is based on the work of Cheng [2008]. Cheng [2008] compared the friction factor from the widely-used Moody [1944] diagram shown in Figure 21 to the data from Nikuradse [1933] which is displayed in Figure 22.

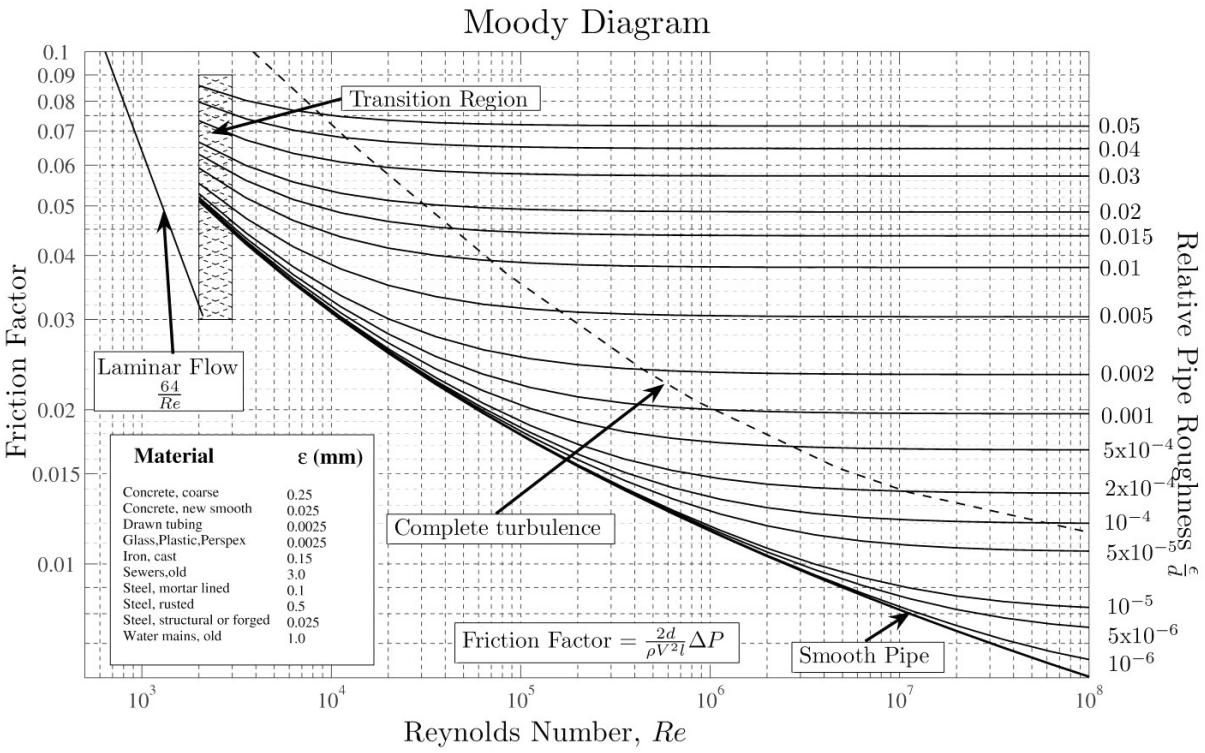

Figure 21: Moody [1944] Diagram. [20]

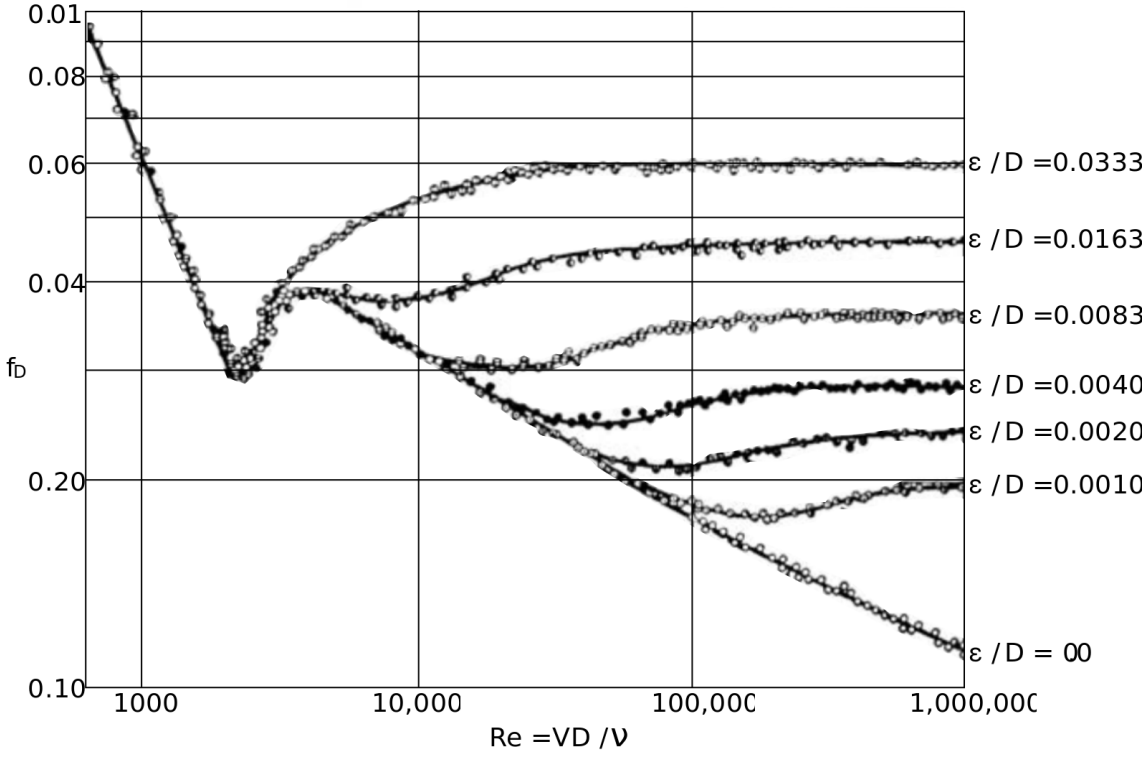

Figure 22: Nikuradse [1933] Diagram. [20]

Moody [1944] related the Darcy-Weisbach friction factor for values of relative pipe roughness against the Reynolds number. Nikuradse [1933] conducted flow measurements which became the benchmark in hydraulic engineering.

In this comparison, Cheng [2008] found that these two friction factor models varied from each other and stated that he developed an interpolation method to derive a single friction equation which includes various flow conditions and even the transitional regimes.

First, Cheng [2008] states the transition from laminar to turbulent flow with the friction factor f which consits of friction for laminar flow, f_L, and for turbulent flow, f_T. These two are influenced by the exponent α_f, a weighting factor.

$$f = f_L^{\alpha_f} f_T^{1-\alpha_f} \tag{25}$$

In turbulent flow, a transitional regime exists between fully smooth and fully rough turbulent flows. This is honored by another weighting factor, the exponent β_f.

$$f_T = f_{TS}^{\beta_f} f_{TR}^{1-\beta_f} \tag{26}$$

Combining these two equations yields

$$f = f_L^{\alpha_f} f_{TS}^{(1-\alpha_f)\beta_f} f_{TR}^{(1-\alpha_f)(1-\beta_f)} \tag{27}$$

To determine these three friction factors, the following three equations may be used respectively. Re is the Reynolds number, d_P is the pipe diameter and k_S is the sand grain diameter.

For laminar pipe flows,

$$f_L = \frac{64}{Re} \tag{28}$$

For fully-smooth turbulent pipe flows,

$$f_{TS} = (1.8 \log\frac{Re}{6.8})^{-2} \tag{29}$$

For fully-rough turbulent pipe flows,

$$f_{TR} = (2 \log\frac{3.7\, d_P}{k_S})^{-2} \tag{30}$$

As an end result, the friction factor for pipes roughened by well-sorted grains is given by

$$\frac{1}{f} = \left(\frac{Re}{64}\right)^{\alpha_f} \left(1.8 \log \frac{Re}{6.8}\right)^{2(1-\alpha_f)\beta_f} \left(2 \log \frac{3.7\, d_P}{k_S}\right)^{2(1-\alpha_f)(1-\beta_f)} \tag{31}$$

The weighting factors α_f and β_f are defined as follows.

$$\alpha_f = \frac{1}{1 + (Re/2720)^9} \tag{32}$$

$$\beta_f = \frac{1}{1 + [Re/(160 * \frac{d_P}{k_S})]^2} \tag{33}$$

2.8.3 Drag Coefficient

The drag coefficient is used to state the amount of resistance an object moving through a fluid experiences. The coefficient includes dependencies such as object shape, speed and fluid density and accounts for skin friction and form drag. It is calculated as follows:

$$c_D = \frac{2\, F_D}{\rho\, v^2\, A} \tag{34}$$

This means that the drag force F_D is proportional to the square of the velocity relative to the fluid and proportional to the density of said fluid. Moreover, it also varies as a function of flow direction, fluid viscosity, and object size. Since velocity, viscosity and length are incorporated in the Reynolds number, the drag coefficient also is a function of Re (Figure 23).

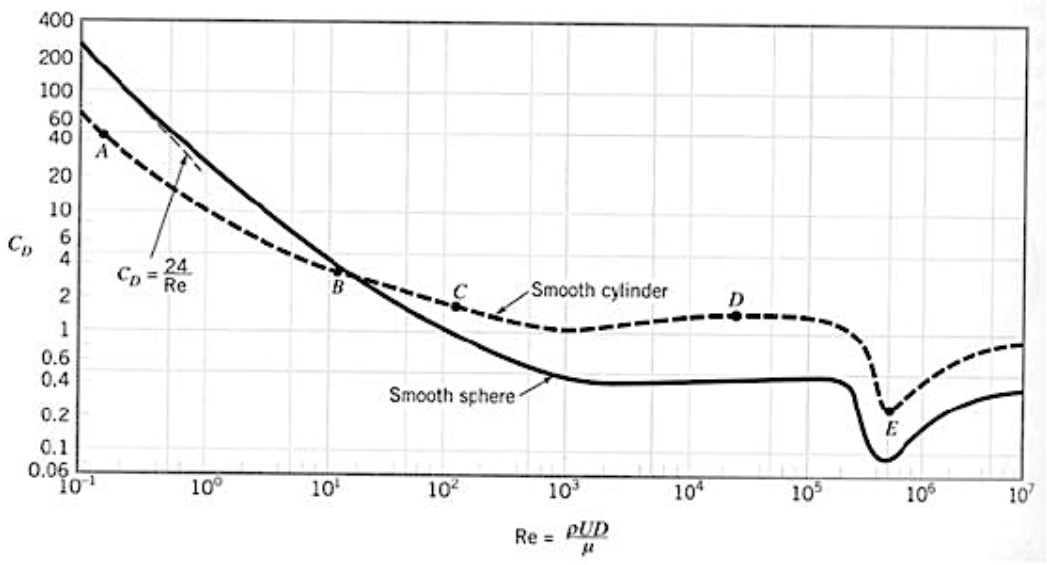

Figure 23: Drag Coefficient vs. Reynolds Number. [21]

In Figure 23, it is shown that for a smooth sphere and for a Reynolds number range of 10^3 to 10^5, the drag coefficient is relatively stable and has a value of about 0.44. This is the value which was used by Turner et al. [1969] for their simplification of the critical velocity calculation. Li et al. [2002] assumed a flattened sphere for their model and took a value of 1.00.

2.8.4 Weber Number

The Weber number is defined as

$$\mathrm{We} = \frac{\mathrm{nert\ a\ of\ flu\ d}}{\mathrm{surface\ tens\ on}} = \frac{\rho_G\, d_d\, v^2}{\sigma_L} \tag{35}$$

It is used to describe the formation and break-up of liquid droplets which are moving through a medium of a certain density with a certain velocity. The external forces try to break up the droplet while the surface tension acts against this process and holds the drop together. The droplet diameter d_d is hard to determine and often the limiting factor in calculations.

This lead to the concept of the critical Weber number which is defined as the point where droplets shatter (Figure 24). Extensive research on this topic was conducted by Hinze [1949]. He determined the Weber number to be on the order of 20 to 30 when they shattered.

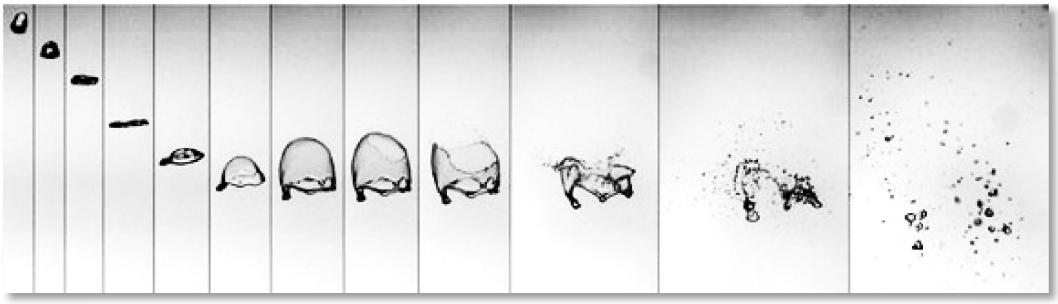

Figure 24: Experiment Conducted to determine Critical Weber Numbers. [23]

Figure 24 shows that at the beginning, the droplet on the left is still intact due to a low velocity and the fact that the surface tension is still large enough to keep the spherical shape. As the velocity increases, the droplet starts to deform which was the area of interest for Li et al. [2002]. At a certain point (frame 5), the droplet starts to deform significantly and the shattering of the droplet begins.

2.8.5 Grashof Number

The Grashof number is the governing parameter for fluid flow in natural convection. With respect to rotationally symmetric flow and considering the influence of the gravitational acceleration, it can be defined as follows:

$$\mathrm{Gr} = \frac{\beta\, g\, \Delta T\, L^3}{\left(\frac{\mu_G}{\rho_G}\right)^2} \tag{36}$$

2.8.6 Prandtl Number

The Prandtl number relates the momentum diffusivity to the thermal diffusivity is defined as

$$\mathrm{Pr} = \frac{\text{v scous d ffus on rate}}{\text{thermal d ffus on rate}} = \frac{\mu/\rho}{k/(c_p\, \rho)} = \frac{\mu\, c_p}{k} \tag{37}$$

Accordingly, a large value signifies that the momentum diffusivity is dominating, while a small value shows that thermal diffusivity is predominant.

2.8.7 Nusselt Number

The Nusselt number describes heat transfer at a thermal boundary layer and is defined as

$$\mathrm{Nu} = \frac{\text{convect ve heat transfer}}{\text{conduct ve heat transfer}} = \frac{hL}{k} \tag{38}$$

It relates convective heat transfer (including advection and diffusion) to conductive heat transfer. In this work, the Gnielinski correlation for forced convection in turbulent pipe flow is applied (see Chapter 3.2).

3 Methodology

In the following chapters, the development of the Entrained Droplet Model, the development of the Heat Transfer Model, the relevant correlations for gas and water properties, and the development of the Two Phase Flow Model are discussed. Later on, these models will then be combined to allow for the calculation of any scenario with a large possibility of different settings and parameters. Thus, adapting the model to any real-world scenario which is desired to be evaluated by this method is possible.

3.1 Entrained Droplet Model

As elaborated in the previous chapter, the final formulation of Turner et al.'s [1969] equation which will be used from this point on is the following:

$$v_c = \left[\frac{4\ g\ \sigma_L\ We_c\ (\rho_L - \rho_G)}{3\ C_D\ \rho_G^2\ s\ n(\alpha)}\right]^{1/4} \tag{39}$$

It slightly varies from Eq.(22) where Li et al. [2014] used a different definition for the deviation angle. The devation angle in Eq.(39) is determined as shown in Figure 25; also, the local running coordinate λ is introduced (starting at the bottom of the wellbore). Gravity is acting downwards (negative z-direction), and the direction of the gas flow is in positive z-direction, from the reservoir up to the surface.

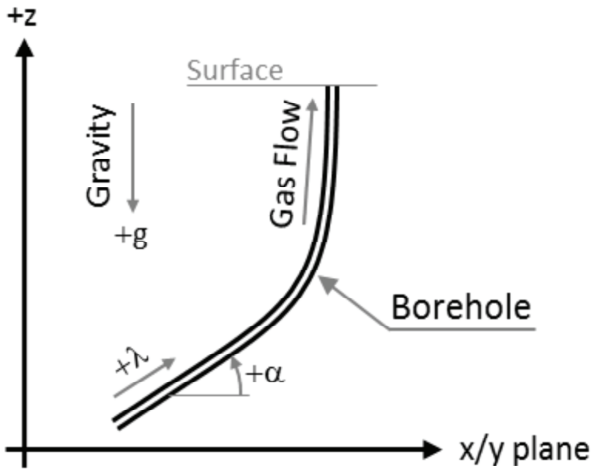

Figure 25: Used Coordinate System. [3]

As mentioned in Chapter 2.1, these are the parameters which make up the critical velocity formula and for which Turner et al. [1969] decided to use average values:

- drag coefficient
- surface tension of water
- surface tension of condensate
- density of water
- density of condensate
- critical Weber number

These simplified assumptions are likely to be the culprits for the mismatch which Turner et al. [1969] and the other authors found when comparing their respective calculated critical velocities with actual field data, and also for the limitation to certain pressure and temperature conditions. Thus, in this approach, the implementation of models for each of these parameters is proposed instead of the use of constant values. Therefore, the ability to calculate the prevailing pressure and temperature conditions for every point in the tubing is absolutely necessary for a representative Entrained Droplet Model since all these parameters ultimately depend on and are influenced by those conditions (see Figure 26).

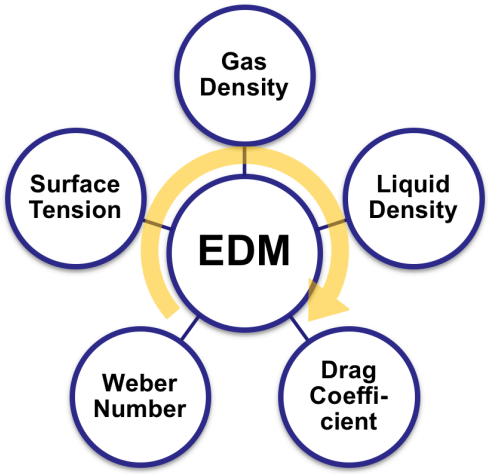

Figure 26: Required Models for the Entrained Droplet Model (EDM). [3]

Thus, a Heat Transfer Model has to be formulated which takes into account the conditions of the wellbore and which can be used for the determination of the current pressure within the tubing and the temperature of the gas stream. This model is described in the next chapter.

It must be emphasized that the Entrained Droplet Model by Turner et al. [1969] is designed for mist flow as the prevailing flow regime in the tubing string, as elaborated in Chapter 3.5.

3.2 Heat Transfer Model

The Heat Transfer Model was developed as outlined in this chapter. According to Michel and Civan [2006 & 2008], the laws of conservation for mass, momentum and energy are used to describe the fluid behaviour, the flow regime and the general equations of pressure and temperature. These equations ultimately all depend on each other since their parameters (like heat capacity, density, Joule-Thomson coefficient, …) themselves depend on and influence the prevailing temperature and pressure conditions.

As shown in Figure 27, the Heat Transfer Model requires the modelling of numerous, previously mentioned, interlinked parameters.

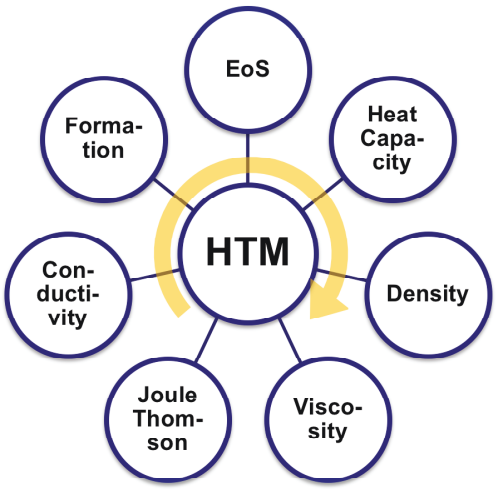

Figure 27: Required Models for the Heat Transfer Model (HTM). [3]

Assuming no losses of mass in the system implies that the mass flow rate $\dot{m}$ is constant at any point in the wellbore as shown in Eq.(40). Moreover, the production conditions are set as steady-state.

$$\dot{m} = \rho_G \, v \, A_f = \text{const.} \tag{40}$$

The momentum balance consists of three terms for which the recently introduced local running coordinate λ is used (Figure 25):

the hydrostatic term

$$\frac{dp}{d\lambda} = -\rho_G \, g \, s \, n \, (\alpha) \tag{41}$$

the friction term

$$\frac{dp}{d\lambda} = -\frac{f_D}{2d}\,\rho_G\,v^2 \tag{42}$$

and the acceleration term

$$\frac{dp}{d\lambda} = -\rho_G\,v\,\frac{dv}{d\lambda} \tag{43}$$

Incoporating these terms into one equation yields the pressure equation

$$\frac{dp}{d\lambda} = -\rho_G\,g\,s\,n(\alpha) - \frac{f_D}{2d}\,\rho_G\,v^2 - \rho_G v\frac{dv}{d\lambda} \tag{44}$$

The combination of mass balance and energy balance leads to the temperature equation

$$\frac{dT}{d\lambda} = \eta\frac{dp}{d\lambda} - \frac{g}{c_p}\,s\,n(\alpha) - \frac{v}{c_p}\frac{dv}{d\lambda} + \frac{q'}{c_p\dot{m}} \tag{45}$$

The first term on the right hand side of Eq.(45) shows that it depends on Eq.(44), while some parameters in Eq.(44) require a temperature value for their calculation. Thus, an iterative approach was chosen.

Using the local running coordinate λ, reformulating Eq.(40) to

$$\rho_G\,v = \frac{\dot{m}}{A_f} \tag{46}$$

and introducing the boundary condition p_b, Eq.(44) can be rewritten as

$$p(\lambda) = p_b - \lambda\,\rho_G\,g\,s\,n(\alpha) - \lambda\frac{f_D}{2d}\,v\,\frac{\dot{m}}{A_f} - \lambda\frac{\dot{m}}{A_f}\frac{dv}{d\lambda} \tag{47}$$

As an entire well may be up to several kilometers long, it has to be divided into multiple sections prior to any calculations taking place. These sections don't have to have the same length; however, they should be homogeneuos. To find homogeneous sections, multiple factors (such as the surrounding formation, the installed completion, used materials, diameters, etc.) have to be taken into account.

This information should subsequently be used to create homogeneuos sections. Then, for the first section located at the end of the wellbore all necessary parameters (density, viscosity, …) are calculated at the bottom and at the top of each section.

As a next step, the results will be used as starting points for the calculation of the next section, and so on. This process is repeated until it is carried out for the entire length of the wellstring.

Since λ starts at the bottom of the wellbore respectively at the bottom of the tubing string, the first value of p_b, as required in Eq.(47), is the pressure at this depth in the casing. For the suceeding sections, p_b is the calculated pressure $p_{(L)}$ at the top of the preceeding sections (Figure 28).

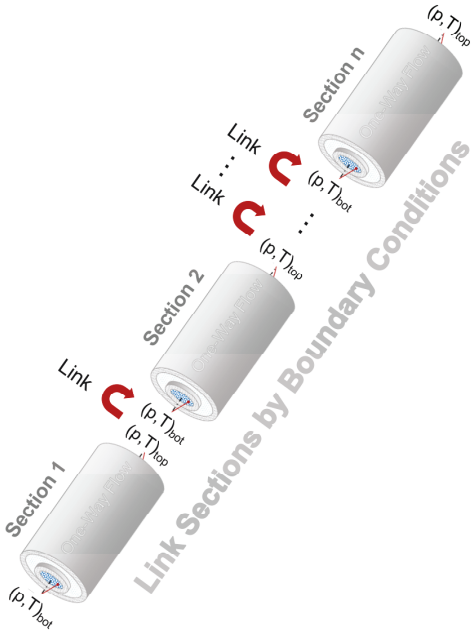

Figure 28: Sections are Linked by Boundary Conditions. [6]

A closer examination of Eq.(45) reveals that it is necessary to replace the specific heat flow, q', with an expression that considers the surrounding borehole wall temperature, the current temperature within the tubing string and the specific thermal resistance:

$$q' = \frac{T_w - T}{R'} \tag{48}$$

The borehole wall temperature, T_w, is calculated with

$$T_w = T_{e,b} - \lambda \gamma_e s \, n(\alpha) \tag{49}$$

where $T_{e,b}$ is the earth temperature at the bottom of the section and γ_e is the geothermal gradient.

Thus, the borehole wall temperature decreases when examining it from the bottom of the well all the way up to the surface; all the while taking into consideration its current location due to the local running coordinate λ and the deviation of the well with $\mathrm{s\,n}\,\alpha$.

Therefore, the temperature equation in its final form may be rewritten as follows:

$$T(\lambda) = \Delta T_{\eta}(\lambda) - \Delta T_{g}(\lambda) - \Delta T_{a}(\lambda) + \Delta T_{e}(\lambda) \tag{50}$$

Term 1 at the right side of Eq.(50) accounts for the Joule-Thomson effect and is defined as

$$\Delta T_{\eta}(\lambda) = \eta\, R'\, c_p\, \dot{m}\, \frac{dp}{d\lambda} \left(1 - e^{-\lambda / R' c_p \dot{m}}\right) \tag{51}$$

Term 2 at the right side of Eq.(50) accounts for the influence of gravity and is defined as

$$\Delta T_{g}(\lambda) = R'\, g\, \dot{m}\, s\, n(\alpha) \left(1 - e^{-\lambda / R' c_p \dot{m}}\right) \tag{52}$$

Term 3 at the right side of Eq.(50) accounts for the influence of acceleration and is defined as

$$\Delta T_{a}(\lambda) = R' \dot{m}\, v\, \frac{dv}{d\lambda} \left(1 - e^{-\lambda / R' c_p \dot{m}}\right) \tag{53}$$

Term 4 at the right side of Eq.(50) accounts for the effects of heat transfer into the formation and is defined as

$$\begin{aligned} \Delta T_{e}(\lambda) = {} & T_{e,b} - \lambda\, \gamma_e\, s\, n(\alpha) - \left(T_{e,b} - T_b\right) e^{-\frac{\lambda}{R'} c_p \dot{m}} \\ & + \gamma_e\, R'\, c_p\, \dot{m} \left(1 - e^{-\lambda / R' c_p \dot{m}}\right) \end{aligned} \tag{54}$$

As a next step, it was necessary to link the steady state borehole to the transient formation surrounding the borehole. The settings which are considered in terms of heat flow between the gas stream and the surrounding formation include the tubing string with potential insulation, the annulus, the completion equipment (including casing, cement, …) and a term responsible for the link to the borehole wall where a transient behaviour of the surrounding formation is assumed (Figure 29).

Thus, the overall thermal resistance can be determined by summing up the specific resistances of each of these settings. The approach includes also resistances caused by conduction, radiation and convection.

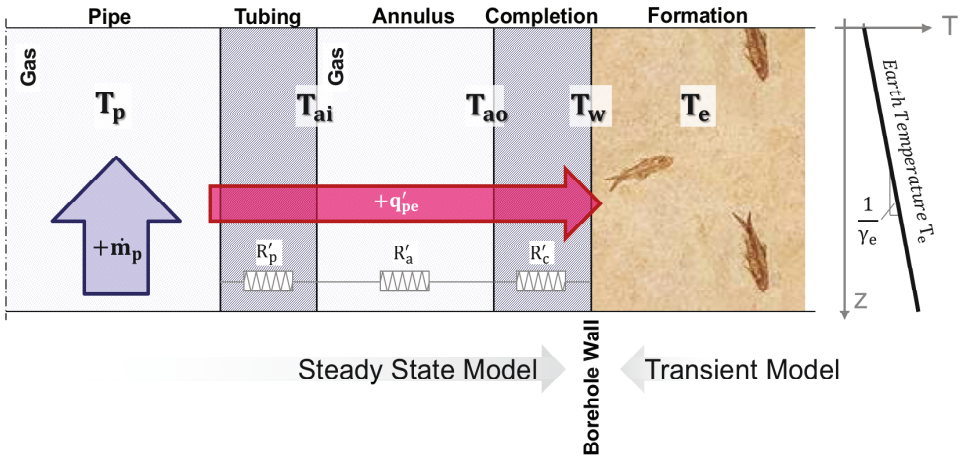

Figure 29: Wellbore Cross-Section. [3]

The routines are based on the following conditions. The Gnielinski [1975] correlation which is valid for Reynolds number values ranging from 10^1 to 10^7 is used to determine the heat transfer coefficient due to forced convection. [26]

The resistance which is caused by free convection is calculated with the Dropkin and Somerscales correlation [1965]. They conducted measurements between enclosed vertical plates to determine values for k_{hc}, the equivalent thermal conductivity of the annular fluid. These values were then correlated as functions of the Grashof number Gr and the Prandtl number Pr. The result expressed as a ratio with k_{ha} is

$$\frac{k_{hc}}{k_{ha}} = 0.049\ (GrPr)^{0.333} Pr^{0.074} \tag{55}$$

with

$$Gr = \frac{(r_{ci} - r_{to})^3 g \rho_{an}^2 \beta (T_{to} - T_{ci})}{\mu_{an}^2} \tag{56}$$

and

$$Pr = \frac{c_{an}\ \mu_{an}}{k_{ha}} \tag{57}$$

Eq.(55) is valid for values of the $GrPr$ product ranging from $5*10^4 < GrPr < 7.17*10^8$ with high-pressure gas wells typically yielding a $GrPr$ product varying roughly from 10^5 to 10^9. [58]

The specific thermal resistance $R´$ is determined by the following equation:

$$R´ = R_t\, L = \frac{1}{U\, A} L = \frac{L}{U\, 2\pi r L} = \frac{1}{U\, 2\pi r} = \frac{1}{U\, \pi d_{BH}} \tag{58}$$

As mentioned before, combining all specific resistances from the various components (tubing, annulus, cement, …) and a term for transient modelling allows the calculation of the overall thermal resistance R' as seen in Eq.(59).

$$R' = R'_p + R'_a + R'_c + H'(t) \tag{59}$$

The last term, $H'(t)$, is a specific resistance depending on time and is used to describe the transient behaviour of the surrounding formation. The transient heat conduction function or g-function, as seen in Eq.(60), is used to determine $H'(t)$.

$$H'(t) = \frac{g(t)}{2\pi k_e} \tag{60}$$

The advantage of this approach is that the transient formation behaviour is connected to the steady state borehole model through the borehole wall temperature, and no numerical simulations are necessary. Solutions are available as infinite line source and as cylindrical heat source models.

3.3 Gas Correlations and Models

For the Entrained Droplet Model and the Heat Transfer Model, numerous publications, methods and models were researched. In the following, the chosen models and correlations for each parameter are introduced and described.

3.3.1 Equation of State

For a proper calculation of the thermodynamic parameters, it was necessary to find a reliable equation of state (EoS).

The equation of state of an ideal gas is defined as

$$pV = nRT \tag{61}$$

The behaviour of a real gas, however, deviates significantly from that of an ideal gas; with possible exceptions of this statement for low pressures and high temperatures. Since these exceptions are not of interest regarding the conditions in a wellbore, the adaptation of the ideal

gas law is absolutely necessary. This is achieved by including a deviation factor, or compressibility factor, z, into Eq.(61).

$$pV = nRTz \tag{62}$$

Thus, for an ideal gas the z-factor is 1. The compressibility factor considers the effects of concepts such as the volume of the gas molecules themselves and the repulsive or attractive forces between molecules.

According to the principle of corresponding states, a relationship between the compressibility factor z and the reduced temperature T_r and reduced pressure p_r exists, as seen in Figure 30. For pure and similar substances, plotting the z-factor versus the reduced pressure yields that they match the same reduced temperature fairly well. [54]

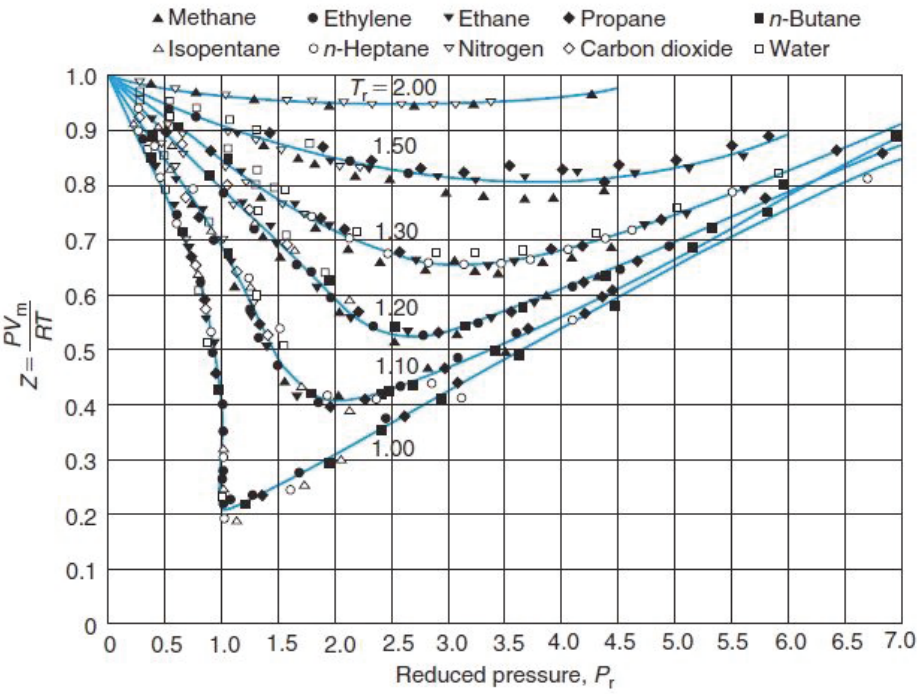

Figure 30: z-Factor vs. Reduced Pressure. [28]

The PE industry standard in terms of z-factor charts was developed by Standing and Katz [1942], as shown in Figure 31. It shows the z-factor as a function of reduced pressure and reduced temperature, and for predicting it, it requires the appropriate temperature and pressure.

However, the composition of the gas which was used to determine the chart is not known. Comparison with experimental data and a study indicate that it was a natural gas mixture without a significant amount of non-hydrocarbon components or C7+ components. [36]

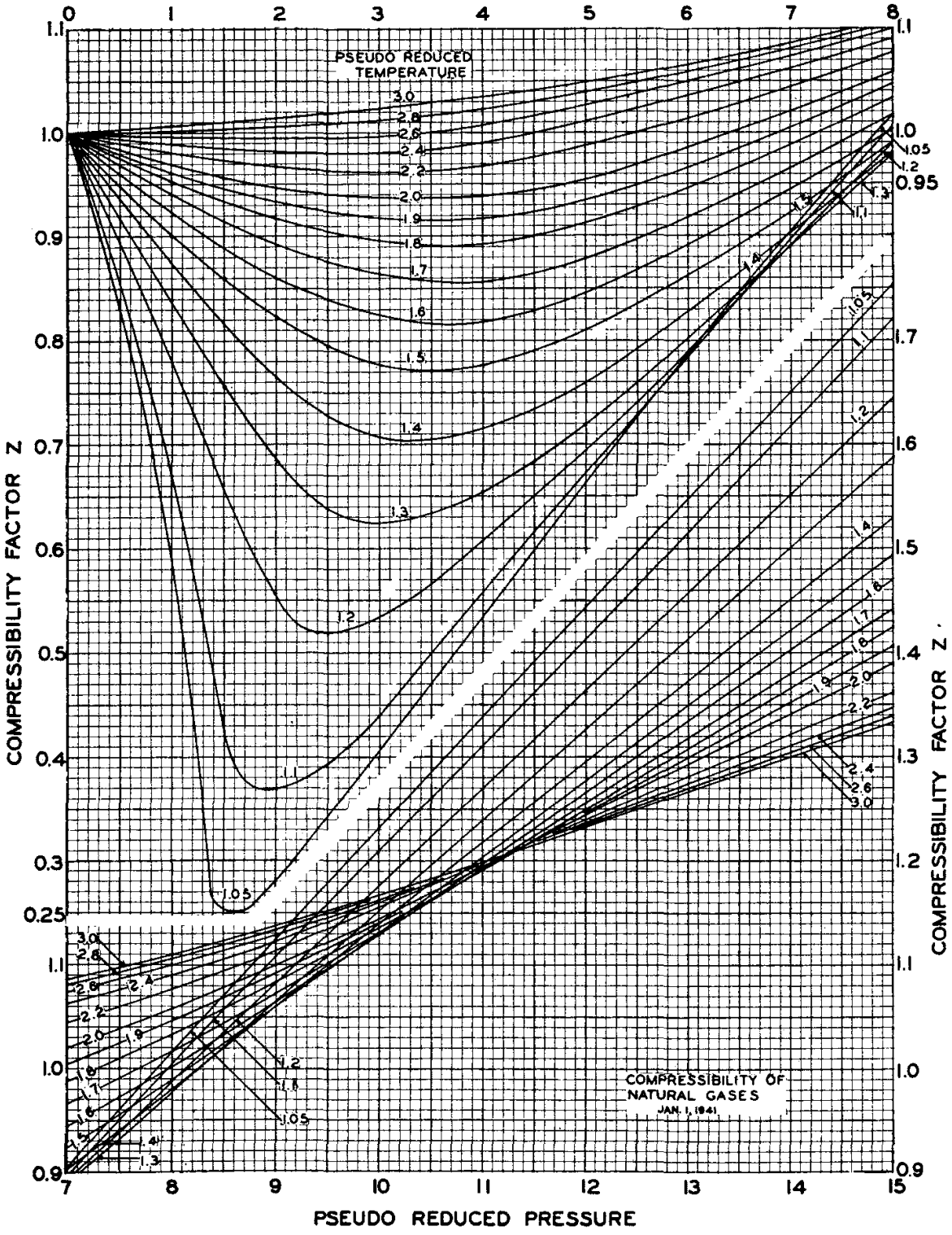

Figure 31: z-Factor Chart by Standing and Katz [1942]. [38]

The reduced temperature and the reduced pressure are defined as follows:

$$T_r = \frac{T}{T_c} \tag{63}$$

$$p_r = \frac{p}{p_c} \tag{64}$$

The critical properties of pure substances are defined and are readily available in the literature.

For mixtures, it is required to estimate the compressibility factor from correlations which in turn depend on the pseudoreduced temperature and the pseudoreduced pressure

$$T_{pr} = \frac{T}{T_{pc}} \tag{65}$$

$$p_{pr} = \frac{p}{p_{pc}} \tag{66}$$

The pseudocritical temperature and the pseudocritical pressure are determined as

$$T_{pc} = \sum y_i \, T_{ci} \tag{67}$$

$$p_{pc} = \sum y_i \, p_{ci} \tag{68}$$

with y_i being the mole fraction of component in the gas mixture. These pseudocritical values should only be used to serve as parameters for corresponding-state correlations, as they possess no physical significance. [31]

Equations (67) and (68) were first suggested by Kay [1936] and are know as *Kay's mixing rule*. Sutton [1985], however, showed that while *Kay's mixing rule* is suitable for associated gas (i.e. natural gas separated from crude oil) which has a specific gas gravity lower than 0.75 and which mostly consists of the components methane to pentane, it is not suited for gas condensates which exhibit a high amount of heptanes-plus and therefore exhibit a higher specific gravity. In this case, pseudocritical properties which are determined with *Kay's mixing rule* are prone to significant error. [30]

Thus, it is prefered to use gas gravity-pseudocritical property relationships depending on the specific gravity of the gas γ_G to determine the pseudo-critical temperature T_{pc} and the pseudo-critical pressure p_{pc} such as the Sutton [1985] correlation:

$$T_{pc} = 169.2 + 349.5\,\gamma_G - 74.0\,\gamma_G^2 \tag{69}$$

$$p_{pc} = 756.8 - 131.0\,\gamma_G - 3.6\,\gamma_G^2 \tag{70}$$

In 2007, Sutton did a review of his previous work. Including the revisions of his formula by other authors and a significant amount of new data, he developed the following updated correlations for gas condensates. [31]

$$T_{pc} = 164.3 + 357.7\,\gamma_G - 67.7\,\gamma_G^2 \tag{71}$$

$$p_{pc} = 744 - 125.4\,\gamma_G + 5.9\,\gamma_G^2 \tag{72}$$

And for associated gas:

$$T_{pc} = 120.1 + 429\,\gamma_G - 62.9\,\gamma_G^2 \tag{73}$$

$$p_{pc} = 671.1 + 14\,\gamma_G - 34.3\,\gamma_G^2 \tag{74}$$

The Sutton [2007] correlation is based on gas samples with specific gas gravities ranging from 0.55 to 2.82 (gas condensates) and 0.55 to 1.86 (associated gas).

It is also possible to account for the influence of impurities such as H_2S, CO_2 and N_2. To this end, the calculation has to be modified as follows according to Standing [1981]:

$$T_{pc}{}^{*} = y_{HC}T_{pcHC} + y_{H_2S}T_{cH_2S} + y_{CO_2}T_{cCO_2} + y_{N_2}T_{cN_2} \tag{75}$$

$$p_{pc}{}^{*} = y_{HC}p_{pcHC} + y_{H_2S}p_{cH_2S} + y_{CO_2}p_{cCO_2} + y_{N_2}p_{cN_2} \tag{76}$$

The method by Wichert and Aziz [1972] modifies these equations further as shown in equations (77) to (79) and allows the final calculation of T_{pc} and p_{pc} with the recognition of impurity influences. Their approach is superior to other methods (such as the ones of Piper et al. [1993] and Elsharkawy and Elkamel [2000]) especially when the levels of impurities are increased, according to Sutton [2007].

$$T_{pc} = T_{pc}{}^{*} - \varepsilon \tag{77}$$

$$p_{pc} = \frac{p_{pc}{}^{*}(T_{pc}{}^{*} - \varepsilon)}{T_{pc}{}^{*} + y_{H_2S}\left(1 - y_{H_2S}\right)\varepsilon} \tag{78}$$

$$\varepsilon = 120\left[\left(y_{CO_2} + y_{H_2S}\right)^{0.9} - \left(y_{CO_2} + y_{H_2S}\right)^{1.6}\right] + 15\left(y_{H_2S}{}^{0.5} - y_{H_2S}{}^{4}\right) \tag{79}$$

Sutton [2007] modified the coefficients and exponents of the deviation parameter ε to tune the equation to the proposed equations (71) through (74). The result can be found Eq.(80).

$$\varepsilon = 107.6\left[(y_{CO_2} + y_{H_2S}) - (y_{CO_2} + y_{H_2S})^{2.2}\right] + 5.9(y_{H_2S}{}^{0.06} - y_{H_2S}{}^{0.68}) \qquad (80)$$

To calculate the z-factor, dedicated correlations are required. The literature shows numerous examples [36]. For this work, the correlation by Dranchuk and Abou-Kassem [1975] was used who proposed a model including eleven constants, A_1 to A_{11}:

$$z = \left[A_1 + \frac{A_2}{T_{pr}} + \frac{A_3}{T_{pr}^3} + \frac{A_4}{T_{pr}^4} + \frac{A_5}{T_{pr}^5}\right]\rho_r + \left[A_6 + \frac{A_7}{T_{pr}} + \frac{A_8}{T_{pr}^2}\right]\rho_r{}^2 - A_9\left[\frac{A_7}{T_{pr}} + \frac{A_8}{T_{pr}^2}\right]\rho_r{}^5 \qquad (81)$$

$$+A_{10}(1 + A_{11}\,\rho_r{}^2)\frac{\rho_r{}^2}{T_{pr}^3}\;\; XP[-A_{11}\,\rho_r{}^2] + 1$$

The reduced density ρ_r is defined as

$$\rho_r = \frac{0.27\,p_{pr}}{zT_{pr}} \qquad (82)$$

The eleven constants A_1 to A_{11} (Table 1) were deduced from the z-factor chart by Standing and Katz [1942] and by fitting the above equation (81) to it.

Table 1: Coefficients for the Dranchuk and Abou-Kassem [1975] z-Factor Correlation. [37]

A_1	0.3265	**A_7**	-0.7361
A_2	-1.0700	**A_8**	0.1844
A_3	-0.5339	**A_9**	0.1056
A_4	0.01569	**A_{10}**	0.6134
A_5	-0.05165	**A_{11}**	0.7210
A_6	0.5475		

As a basis, the Fortran code of their investigation (specifically the ZSTAR subroutine, [59]) including the corrections proposed by Borges [1991] were used in this work [39]. These corrections increased the maximum reduced density value of 2.2 to 3.0. The result of the Dranchuk and Abou-Kassem correlation [1975] can be seen in Figure 32.

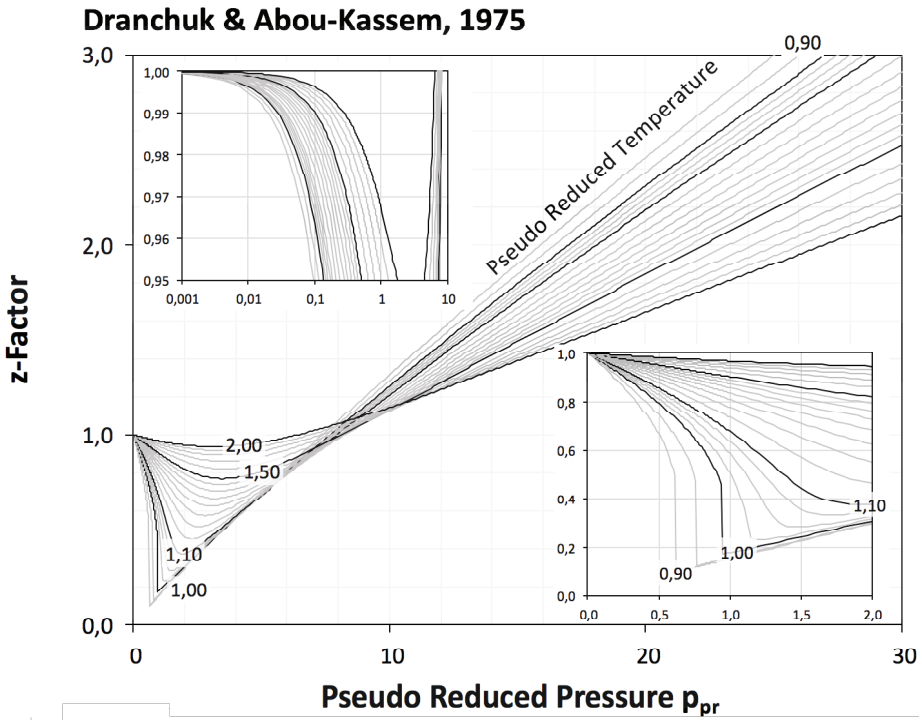

Figure 32: z-Factor values after Dranchuk and Abou-Kassem [1975] including the proposed Corrections by Borges [1991].

3.3.2 Specific Heat Capacity

When dealing with gas flow and heat transfer, it is necessary to accurately estimate the specific isobaric heat capacity of natural gases. Methods for pure and simple mixtures are sufficiently available, but those concerning themselves with natural gases and their possible impurities (such as CO_2, H_2S, N_2) at the required temperature and pressure ranges are required for a realistic simulation. [40]

The approach of Dranchuk and Abou-Kassem [1992] is based on calculating the specific isobaric heat capacity as the sum of the ideal specific isobaric heat capacity and of the specific isobaric heat capacity departure from the ideal state.

$$C_{p_m} = {C_{p_m}}^0 + (C_{p_m} - {C_{p_m}}^0) \tag{83}$$

For the specific isobaric heat capacity departure, they obtained the following equation by fitting the Benedict-Webb-Rubin (BWR) equation to the Standing and Katz [1942] z-factor.

$$(C_{p_m} - {C_{p_m}}^0)/R = \tag{84}$$

$$-1 - 6(A_3/T_{pr}^3)\rho_r - 6A_7/(A_8 T_{pr}^3) + [\frac{6A_7}{A_8 T_{pr}^3} + 3(\frac{A_7}{T_{pr}^3})\rho_r^2]\ e\ \ p\ (-A_8\rho_r^2) +$$

$$[1 + \left(A_1 - \frac{2A_3}{T_{pr}^3}\right)\rho_r + A_4\rho_r^2 - 2\left(\frac{A_7}{T_{pr}^3}\right)\rho_r{}^2(1 + A_8\rho_r^2)\ e\ \ p(-A_8\rho_r^2)]^{\,2}\ /$$

$$[1 + 2(A_1 + \frac{A_2}{T_{pr}} + \frac{A_3}{T_{pr}{}^3})\rho_r + 3(A_4 + A_5/T_{pr})\rho_r^2 + 6(A_5/T_{pr})A_6\rho_r^5 +$$

$$(A_7/T_{pr}^3)\rho_r^2(3 + 3A_8\rho_r^2 - 2A_8{}^2\rho_r^4)\ e\ \ p\ (-A_8\rho_r^2)]$$

The reduced temperature required for the calculations is determined as shown in Eq.(85) and (86), with the help of the previously mentioned mixing rule for molal averaging by Kay [1936].

$$T_{pr} = \frac{T}{T_{pc}} \tag{85}$$

$$T_{pc} = \sum y_i\ T_{ci} \tag{86}$$

The constants which were used for the calculation of the specific isobaric heat capacity departure in Eq.(84) are stated in Table 2. [41]

Table 2: Coefficients for the Specific Isobaric Heat Capacity Departure. [41]

A_1	0.31506237	**A_5**	-0.61232032
A_2	-1.0467099	**A_6**	-0.10488813
A_3	-0.57832729	**A_7**	0.68157001
A_4	0.53530771	**A_8**	0.68446549

The results indicated that it can be applied to sweet and sour natural gases as a generalized correlation. The ideal heat capacity model is valid for specific gravities ranging from 0.55 to 1.0 with temperatures ranging from 300 to 1,500 K. The equation for the specific isobaric heat capacity departure may be used for p_r ranging from 0.2 to 15 and T_r ranging from 1.05 to 3.0.

Another model developed by Lateef and Omeke [2011] uses correlations which take into consideration the individual composition of the gas, its density and its temperature. As an assumption, they stated that natural gases with the same specific gravity have the same components in identical proportions. This means that a mixture of 80 % methane and 20 % ethane has the same specific gravity as a mixture of 90 % methane and 10 % propane. They substantiate that this assumption does not negatively affect the result, yet simplifies the calculation.

The pseudo-critical temperatures and pressures were calculated with *Kay's mixing rule* [29]:

$$T_{pc} = \sum y_i \, T_{ci} \tag{87}$$

$$p_{pc} = \sum y_i \, p_{ci} \tag{88}$$

For the specific gravity and specific heat capacity, the following equations were used [42]:

$$\gamma_G = \sum y_i \gamma_{Gi} \tag{89}$$

$$C_p = \sum y_i C_{pi} \tag{90}$$

The specific heat capacity was then expressed as a function depending on temperature, and after applying a quadratic least square fit, the coefficients were calculated and combined to a final equation as seen in Eq.(91).

$$\begin{aligned} C_p = {} & \left(59.55\gamma_G^2 - 97.86\gamma_G + 56.46\right) + \left(-0.17084\gamma_G^2 + 0.46755\gamma_G - 0.15883\right)T \\ & + \left(1.52903 * 10^{-4}\gamma_G^2 - 3.57387 * 10^{-4}\gamma_G + 1.65604 * 10^{-4}\right)T^2 \\ & + \left(-4.5789 * 10^{-8}\gamma_G^2 + 9.8468 * 10^{-8}\gamma_G - 5.2019 * 10^{-8}\right)T^3 \end{aligned} \tag{91}$$

This calculation is valid for specific gas gravities γ_G ranging from 0.55 to 1 and for temperatures T ranging from 100 to 1,500 K.

However, after a cross-validation with the Brown and Holme [2011] chart, it was noted that a deviation from these values exists. This deviation is defined by the following equation:

$$\frac{C_{p,real}}{C_{p,ideal}} = \left(0.000156p_{pr}^3 - 0.005435p_{pr}^2 + 0.060528p_{pr} + 0.942510\right)^{\frac{\gamma}{0.7}} \tag{92}$$

The final version of the specific heat capacity (in oilfield units) which considers this deviation from the Brown and Holme [2011] chart looks as follows:

$$\begin{aligned} C_{p,real} = {} & \left(0.000156p_{pr}^3 - 0.005435p_{pr}^2 + 0.060528p_{pr} + 0.942510\right)^{\frac{\gamma}{0.7}} \\ & \left[\left(6.0050\gamma_g^2 - 0.0416\gamma_g + 6.1719\right)\right. \\ & + \left(-1.3498 * 10^{-2}\gamma_g^2 + 4.0381 * 10^{-2}\gamma_g - 1.1206 * 10^{-2}\right)T \\ & + \left(8.6856 * 10^{-6}\gamma_g^2 - 2.0784 * 10^{-6}\gamma_g + 9.2702 * 10^{-6}\right)T^2 \\ & \left. + \left(-1.8749 * 10^{-9}\gamma_g^2 + 4.0319 * 10^{-9}\gamma_g - 2.1300 * 10^{-9}\right)T^3\right] \end{aligned} \tag{93}$$

The boundary conditions in this case are a specific gas gravity between 0.55 to 1 and a temperature ranging from 150 to 2,000 °F (65 to 1090 °C). As a result, Figure 33 shows the behaviour of the model of Lateef and Omeke [2011].

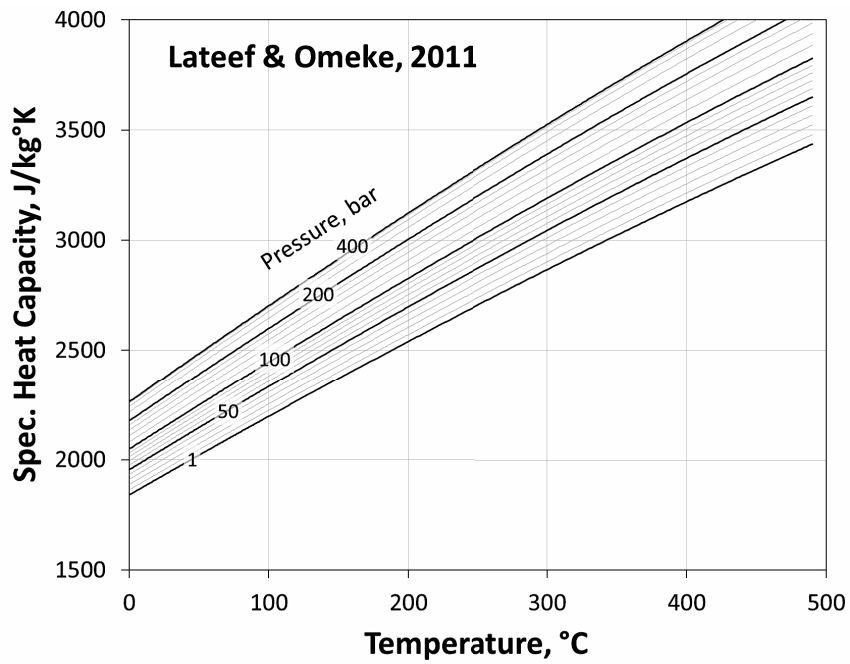

Figure 33: Specific Heat Capacity after Lateef and Omeke [2011].

3.3.3 Density

Based on the Equation of State for real gases,

$$pV = nRTz \tag{94}$$

the number of moles, n, can also be expressed as mass m divided by molar mass M_w

$$n = \frac{m}{M_w} \tag{95}$$

Moreover, volume V is generally defined as

$$V = \frac{m}{\rho} \tag{96}$$

and thus, Eq.(94) can be re-arranged to state the density of gas as

$$\rho_G = \frac{p\,M_w}{R\,T\,z} \tag{97}$$

In such situations where the molar mass M_w is not known and the natural gas composition is not readily available as well, it can be determined based upon the specific gravity of the gas γ_G by using Eq.(98). [24 & 25]

$$M_w = 28.9625\,\gamma_G \tag{98}$$

Figure 34 shows the behaviour of the density depending on temperature and pressure.

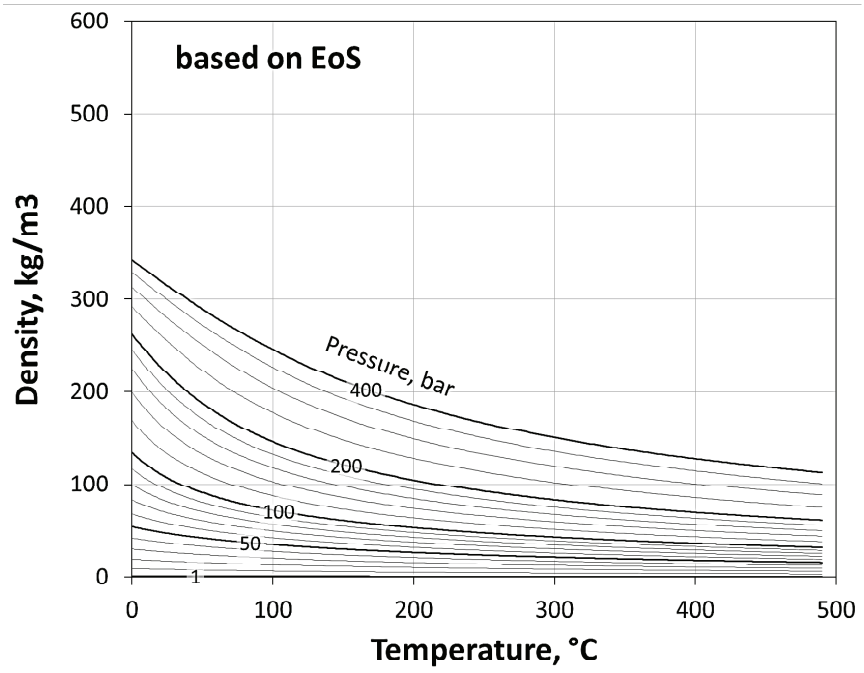

Figure 34: Density vs. Temperature.

As shown in Eq.(97), an increase in pressure results in a higher gas density, while a temperature increase causes a decrease in density.

3.3.4 Dynamic Viscosity

The dynamic viscosity of natural gas at reservoir conditions or at high pressures and temperatures is most important for calculations. However, to obtain accurate dynamic viscosity values, tedious experiments are necessary. Thus, it is common practice to take advantage of the data which has already been obtained and to use it to formulate empirical correlations. The dynamic viscosity of a pure gas depends on pressure and temperature; a gas mixture such as natural gas depends on the composition as well. This is especially true when impurities such as N_2, CO_2 and H_2S are present. Most procedures involve two steps: in the first, the viscosity μ_g at atmospheric pressure is calculated and in the second, the viscosity ratio $\frac{\mu}{\mu_G}$ as a function of T_r and p_r is considered. [44]

$$\mu_G = (A_1 + A_2 T) - (A_3 + A_4 T)\sqrt{M_g} \quad [c \quad] \tag{99}$$

$$\frac{\mu}{\mu_G} = (A_5 + A_6 p_r + A_7 p_r^2)\frac{1}{T_r} + (A_8 + A_9 p_r + A_{10} p_r^2)\frac{1}{T_r^4} + (A_{11} + A_{12} p_r + A_{13} p_r^2) \tag{100}$$

This approach formulated by Gurbanov and Dadash-Zade [1986] and the changes made to the coefficients by Chen and Ruth [1993] were used for this work (Table 3).

Table 3: Coefficients determined by Chen and Ruth [1993] for the Gurbanov and Dadash-Zade [1986] Viscosity Model used in Equations (99) and (100). [44]

A_1	0.0038539
A_2	0.0000356
A_3	0.0004131
A_4	0.0000016
A_5	-0.4888439
A_6	-0.0943952
A_7	0.0199591

A_8	0.8266923
A_9	1.7124100
A_{10}	-0.0700968
A_{11}	1.2076900
A_{12}	0.0301188
A_{13}	-0.0048318

Thanks to these corrections, the range of validity of the Gurbanov and Dadash-Zade [1986] correlation is extended to a reduced pressure p_r of 1 to 15 and a reduced temperature T_r of 1.05 to 2.8. The calculation of the dynamic viscosity model can be seen in Figure 35.

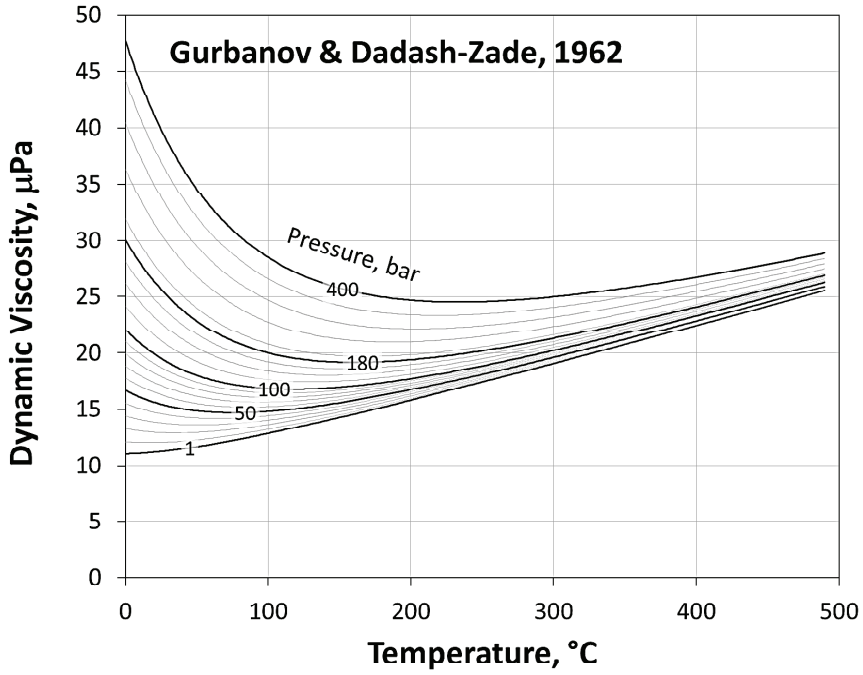

Figure 35: Dynamic Viscosity Model by Gurbanov and Dadash-Zade [1986] ($\gamma_G = 0.7$).

3.3.5 Joule-Thomson Coefficient

The Joule-Thomson effect characterizes the temperature variation which occurs when real fluids expand. This expansion is an irreversible process and also exists during gas production. It should be noted that because of the Joule-Thomson effect, the cooling down of the natural gas on its way from the reservoir to the surface is inevitable due to decreasing pressure and the resulting expansion of the gas during its transport up within the tubing. Thus, even in a perfectly insulated tubing, temperature decreases would be observed. However, depending on the state of the fluid, and on the fluid itself, a warming effect is also possible. Conditions to allow such a warming effect, however, are not likely to be encountered in gas production scenarios. [75]

The Joule-Thomson (JT) coefficient is the rate of temperature change with respect to pressure at constant enthalpy. Using the Maxwell Identities

$$\left(\partial H/\partial p\right)_T = V + T\left(\partial S/\partial p\right)_T \tag{101}$$

and

$$\left(\partial S/\partial p\right)_T = \left(\partial V/\partial T\right)_p \tag{102}$$

the JT coefficient can be derived as

$$c_p\eta = -\left[V - T\left(\partial V/\partial T\right)_p\right] \tag{103}$$

and re-arranged to

$$\eta = \frac{1}{c_p\rho_G}\frac{T}{z}\left(\frac{z}{T}\right)_p \tag{104}$$

As can be seen in Eq.(104), the JT coefficient depends on heat capacity, density, temperature and the z-factor. In detail, the calculation requires the derivative of the z-factor with respect to temperature. In Figure 36, the z-factor model using JT coefficients based on numerical differentiation is shown, as a function of temperature and with pressures ranging from 1 to 400 bar. With increasing temperature, the z-factor shows an increase which strongly depends on the pressure conditions.

In Figure 37, the corresponding JT coefficients are presented. With increasing temperature (0 to 500 °C) and also with increasing pressure (1 to 400 bar), the JT coefficient continuously decreases. While there is a significant difference at low temperatures, from 300 °C onwards the differences are increasingly smaller.

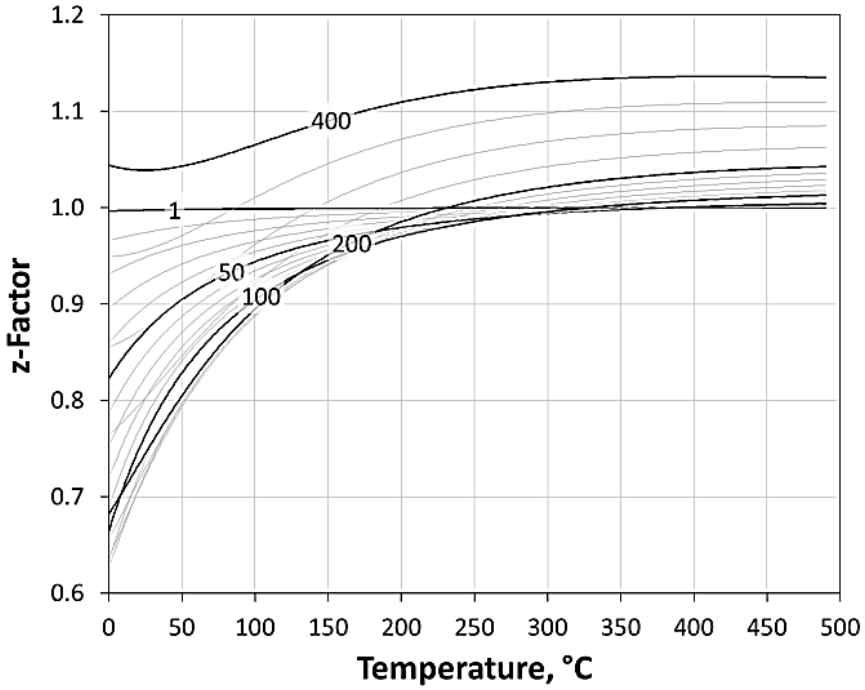

Figure 36: z-Factor vs. Temperature ($\gamma_G = 0.7$).

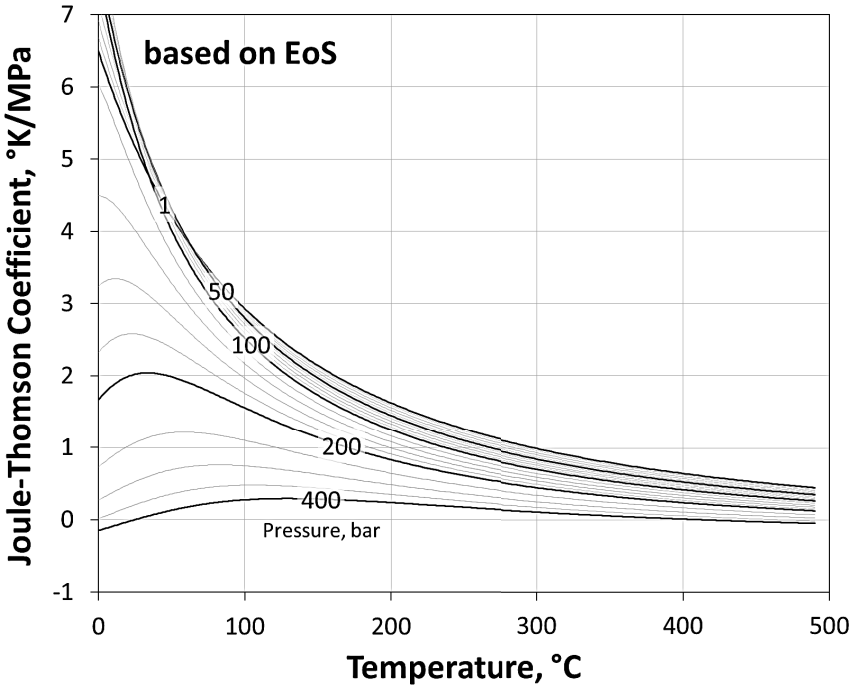

Figure 37: JT Coefficients vs. Temperature ($\gamma_G = 0.7$).

3.3.6 Formation Volume Factor

The formation volume factor for gas is defined as the ratio of the gas volume at reservoir temperature and reservoir pressure to the gas volume at standard temperature and standard pressure.

$$_G = \frac{V_R}{V_{SC}} = \frac{\frac{nRTz}{p}}{\frac{nRT_{SC}z_{SC}}{p_{SC}}} = \frac{T\ z\ p_{SC}}{T_{SC}\ z_{SC}\ p} \tag{105}$$

The standard conditions are $z_{SC} = 1,\ p_{SC} = 101.325\ \text{kPa}$ and $T_{SC} = 288.15$ and thus, the equation can be rewritten as

$$_G = 0.351\frac{zT}{p}\ [\text{Rm}^3/\text{Nm}^3]\text{; p in kPa, T in K} \tag{106}$$

3.4 Water Correlations and Models

Correlations for the behaviour of water under given pressure and temperature conditions were also of importance to ensure a proper simulation of the influence on gas flow. In the next chapters, these correlations are introduced and outlined.

3.4.1 Specific Heat Capacity

As mentioned in Chapter 3.3.2, the specific heat capacity is an important material characteristic. In this work, the calculation of the specific isobaric heat capacity of pure water is based on a curve-fit using available heat capacity data. [61]

The resulting equation of the curve-fit is shown in Eq.(107); the determined coefficients are shown in Table 4.

$$c_{p,W} = A_1 * T^5 + A_2 * T^4 + A_3 * T^3 + A_4 * T^2 + A_5 * T + A_6 \tag{107}$$

This formula is valid for a temperature range of 0 to 200 °C. The parameters A_1 to A_6 are listed in Table 4.

Table 4: Coefficients for the Specific Isobaric Heat Capacity of Water.

A_1	-0.0000000028377
A_2	0.0000017393
A_3	- 0.00035895

A_4	0.042519
A_5	- 2.022
A_6	4210.1

In Figure 38, the specific isobaric heat capacity is plotted versus temperature. In the temperature range of 0 to 200 °C, the specific heat capacity of water varies between 4178 and 4510 J/kg°K.

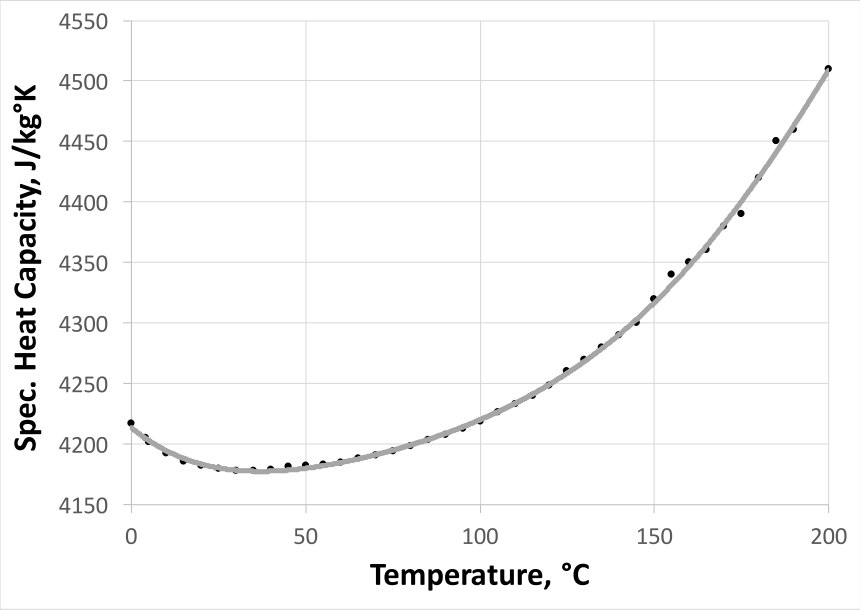

Figure 38: Specific Isobaric Heat Capacity of Water vs. Temperature.

3.4.2 Density

The following formula is used to calculate the saturated density ρ_W of water up to the critical temperature of about 375 °C. It is solely a function of temperature. [46]

$$\rho_W = \frac{A_1}{A_2^{\,1+(1-T/A\,)^{A_4}}} \tag{108}$$

This formula is valid for a temperature range of 273 to 648 K; the required parameters are listed in Table 5.

Table 5: Coefficients for the Saturated Water Density Formula. [46]

A_1	0.14395	A_3	649.727
A_2	0.0112	A_4	0.05107

Figure 39 shows that the density of saturated water decreases steadily with increasing temperature. The highest density is at 0 °C, while at 375 °C or 648 K (the critical temperature of water) a liquid phase no longer occurs.

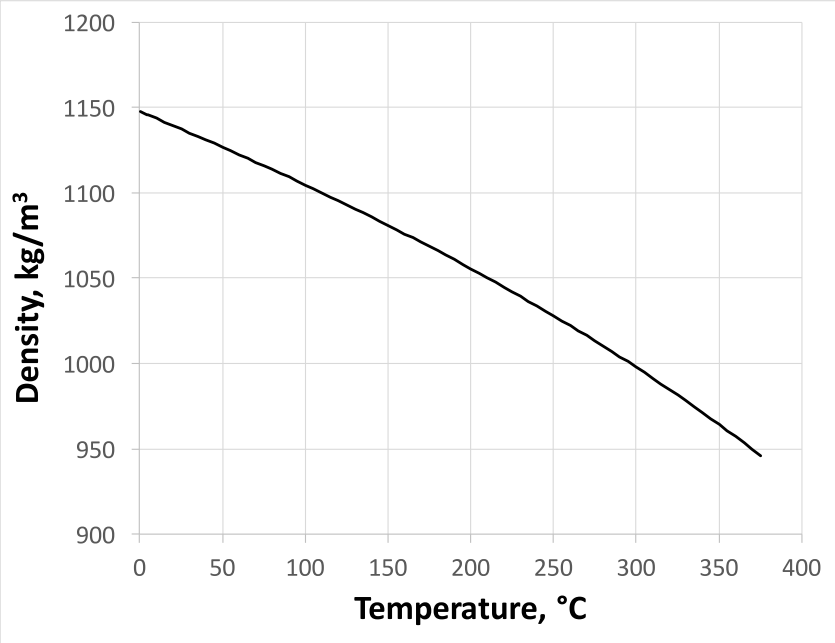

Figure 39: Saturated Water Density vs. Temperature (up to T_c = 375 °C).

3.4.3 Dynamic Viscosity

The water is assumed to be free of contaminants and thus, it is possible to calculate the dynamic viscosity of water μ_W using the Van Wingen correlation. [62]

The Van Wingen correlation is defined as follows:

$$\ln \mu_W = 1.003 - 1.479 * 10^{-2} \left(T * \frac{9}{5} + 32\right) + 1.982 * 10^{-5} \left(T * \frac{9}{5} + 32\right)^2 \text{ [cp]}; \quad \text{T in °C} \tag{109}$$

3.4.4 Surface Tension

For the calculation of the surface tension of water, the following formula by Kestin et al. [1984] is used:

$$\sigma_W = \left(\frac{T_c - T}{T_c}\right)^{1.256} \left[1 - 0.625 \left(\frac{T_c - T}{T_c}\right)\right] \tag{110}$$

The critical temperature T_c for water is 647 K or 374 °C. In Figure 40, the dependency of the surface tension on temperature is shown. Once the water reaches the critical temperature of 375 °C, the surface tension becomes zero. Turner et al. [1969] used a constant value of 0.06 N/m which holds true for a temperature of about 96 °C.

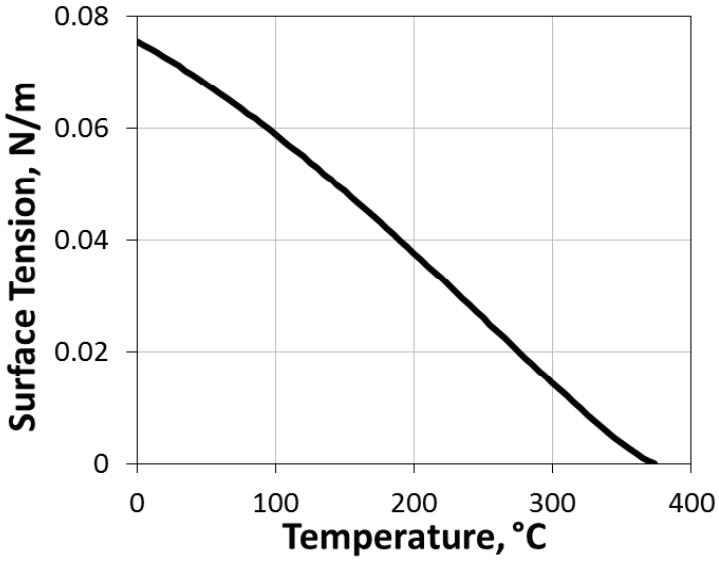

Figure 40: Water Surface Tension vs. Temperature (up to T_c = 375 °C).

3.4.5 Formation Volume Factor

The formation volume factor of water can be estimated using the following correlation by McCain [1991]. The values provided by this correlation agree with existing data to within 2 % for temperatures up to about 130 °C and pressures up to about 350 bar.

$$B_W = (1 + A_1)(1 + A_2) \tag{111}$$

with

$$A_1 = -1.00010 * 10^{-2} + 1.33391 * 10^{-4}\,(T * \frac{9}{5} + 32) + 5.50654 * 10^{-7}\,(T * \frac{9}{5} + 32)^2;\ T \text{ in °C}$$

$$A_2 = -1.95301 * 10^{-9}(14.5037p)\left(T * \frac{9}{5} + 32\right) - 1.72834 * 10^{-13}(14.5037p)^2\left(T * \frac{9}{5} + 32\right)$$
$$-3.58922 * 10^{-7}(14.5037p) - 2.25341 * 10^{-10}(14.5037p)^2;\quad T \text{ in °C, p in bar}$$

3.4.6 Solubility

The solubility of gas in water is calculated as follows according to Ahmed [2007]

$$R_{G/W} = 0.178(A_3 + A_4 p + A_5 p^2)\ [m^3/m^3];\ p \text{ in bar} \tag{112}$$

with

$$_3 = 2.12 + 3.45 * 10^{-3} \left(T * \frac{9}{5} + 32\right) - 3.59 * 10^{-5} \left(T * \frac{9}{5} + 32\right)^2; \text{ T in °C}$$

$$_4 = 0.0107 - 5.26 * 10^{-5} \left(T * \frac{9}{5} + 32\right) + 1.48 * 10^{-7} \left(T * \frac{9}{5} + 32\right)^2; \text{ T in °C}$$

$$_5 = 8.75 * 10^{-7} + 3.9 * 10^{-9} \left(T * \frac{9}{5} + 32\right) - 1.02 * 10^{-11} \left(T * \frac{9}{5} + 32\right)^2; \text{ T in °C}$$

3.5 Two Phase Flow Model

In the scope of this work, the water lifting capability of the produced gas according to the Turner equation is investigated. In order to use the Turner equation in a meaningful way, mist flow (which is discussed further in Chapter 3.5.4) has to be the prevailing flow regime.

Two phase flow of gas and water is simulated with increasing volumes of water. In the following chapters, the necessary formulas to link gas properties and water properties are presented.

3.5.1 Linking Gas and Water Properties

As previously mentioned, certain properties of the two fluids natural gas and liquid water have to be connected to allow for reasonable simulation results.

3.5.1.1 Specific Heat Capacity

The specific heat capacity of a mixture $c_{p,mix}$ can be calculated by considering the respective specific heat capacity and the respective weight fractions of each constituent of the mixture. [65, pp.83–85]

The parameters $\dot{m}_G$, $\dot{m}_W$ and $\dot{m}_{mix}$ are discussed in Chapter 3.5.2 in more detail.

$$c_{p,mix} = c_{p,G} \frac{\dot{m}_G}{\dot{m}_{mix}} + c_{p,W} \frac{\dot{m}_W}{\dot{m}_{mix}} \tag{113}$$

3.5.1.2 Density

The density of the two phase system ρ_{mix} is calculated using the mixture mass flow rate $\dot{m}_{mix}$ and the mixture volumetric flow rate $\dot{V}_{mix}$. The definitions of these flow rates ($\dot{m}_{mix}$ and $\dot{V}_{mix}$) are discussed in Chapter 3.5.2 in more detail.

$$\rho_{mix} = \frac{\dot{m}_{mix}}{\dot{V}_{mix}} \tag{114}$$

3.5.1.3 Dynamic Viscosity

The average dynamic viscosity of the gas-water system μ_{mix} is determined by using the respective dynamic viscosity μ_G and μ_W and also the respective phase saturation parameters S_G and S_W. [24 & 25]

The viscosity and the phase saturations are calculated as follows. The parameters $\dot{V}_G$ and $\dot{V}_W$ are discussed in Chapter 3.5.2 in more detail.

$$\mu_{mix} = S_G * \mu_G + S_W * \mu_W \tag{115}$$

$$S_G = \frac{\dot{V}_G}{\dot{V}_{mix}} \tag{116}$$

$$S_W = \frac{\dot{V}_W}{\dot{V}_{mix}} \tag{117}$$

3.5.2 Two Phase Flow Rates

The mass flow rate $\dot{m}$ which was mentioned in Eq.(40) can also be extended to account for multiphase flow as follows. [24 & 25]

The two different phases considered are gas and water. As a prerequisite, the respective densities and volumetric flow rates at standard conditions have to be known to calculate the total mass flow rate $\dot{m}$.

$$\dot{m}_{mix} = \sum \rho_i^S \dot{V}_i^S = \rho_G^S \dot{V}_G^S + \rho_W^S \dot{V}_W^S = \text{const.} \tag{118}$$

Eq.(118) can also be used with the specific gas gravity instead of the gas density.

$$\dot{m}_{mix} = \dot{m}_G + \dot{m}_W \tag{119}$$

with

$$\dot{m}_G = \gamma_G \rho_A^S \dot{V}_G^S \tag{120}$$

$$\dot{m}_W = \rho_W^S \dot{V}_W^S \tag{121}$$

and with $\rho_A^S = 1.275\ \mathrm{kg/m^3}$ and $\rho_W^S = 999.972\ \mathrm{kg/m^3}$. As input, the specific gas gravity γ_G, the volumetric gas flow rate $\dot{V}_G^S$ and the volumetric water flow rate $\dot{V}_W^S$ are required. Assigning the volumetric water flow rate the value of zero ($\dot{V}_W^S = 0\ \mathrm{Nm^3/d}$) has the effect of reducing this set of equations back to Single Phase Modelling. [24 & 25]

The total volumetric flow rate of the mixture $\dot{V}_{mix}$ is measured as

$$\dot{V}_{mix} = \dot{V}_G + \dot{V}_W \tag{122}$$

with

$$\dot{V}_G = (\dot{V}_G^S - R_{G/W}\dot{V}_W^S)_{\ G} \tag{123}$$

$$\dot{V}_W = \dot{V}_W^S{}_{\ W} \tag{124}$$

3.5.3 Velocities

Other effects to consider in multiphase flow are different velocities of the phases such as the superficial velocity, the actual velocity and the slip velocity, and new concepts such as liquid holdup. This chapter aims to give an overview over these velocities and their definitions and meanings.

The superficial velocity v_S is the velocity of a fluid travelling through a pipe and is defined as volumetric fluid flow rate of fluid divided by the total cross-section of the pipe. In multiphase flow, this represents not a real, physical velocity but rather a convenient way for analysis and comparison.

In other words, the superficial velocity is the velocity with which the fluid would travel if it was the only fluid within the pipe. Since each phase occupies an actual cross-section that is smaller than the total cross-section, the superficial velocity of a phase is always smaller than the real velocity of that phase. [74]

$$v_{S,L} = \frac{\text{Volumetr c flo rate of l qu d}}{\text{Total cross-sect on of p pe}} = \frac{\dot{V}_W}{A_P} \tag{125}$$

$$v_{S,G} = \frac{\text{Volumetr c flo rate of gas}}{\text{Total cross-sect on of p pe}} = \frac{\dot{V}_G}{A_P} \tag{126}$$

The actual velocity v is defined as volumetric fluid flow rate divided by the fluid cross-section of the pipe. It denotes the actual velocity of the respective fluid in the pipe.

$$v_L = \frac{\text{Volumetr c flo rate of l qu d}}{\text{L qu d cross-sect on of p pe}} \tag{127}$$

$$v_G = \frac{\text{Volumetr c flo rate of gas}}{\text{Gas cross-sect on of p pe}} \tag{128}$$

The slip velocity v_{slip} is the difference between the velocities of the lighter fluid and of the heavier fluid in a pipe. The difference mostly depends on the density difference. [74]

$$v_{slip} = v_G - v_L \tag{129}$$

Also, the so-called no-slip liquid holdup λ_L can be calculated as a function of the superficial velocities of each phase. It is straightforward to calculate if the volumetric flow rate for each phase is known, as shown in equations (125) and (126). [50]

$$\lambda_L = \frac{V_{S,L}}{V_{S,L} + V_{S,G}} \tag{130}$$

Another important concept to consider in multiphase flow is liquid holdup with slip. Since each fluid travels at different speeds due to buoyancy differences and other factors, this effect can be calculated with the parameter H_L. The heavier phase moves slower, or is more held up, than the lighter phase. Also, the holdup of a fluid is not equivalent to the proportion of the total flow rate, or cut, of that fluid. [49]

$$H_L = \frac{\text{Volume of liquid in pipe element}}{\text{Volume of pipe element}} \tag{131}$$

Therefore, if a pipe is completely filled with gas, H_L equals 0. If it is completely filled with liquid, H_L equals 1. Increasing liquid holdup thus means an increasing amount of water is present within the pipe.

Consequently, the gas holdup or void fraction H_G can be calculated with the following formula:

$$H_G = 1 - H_L \tag{132}$$

However, liquid holdup values cannot be calculated analytically. It depends on parameters such as gas and liquid properties, flow pattern, pipe diameter and pipe inclination and has to be determined using empirical correlations. Mostly due to the aforementioned buoyancy differences, gas usually travels faster than liquid and therefore, slippage between the phases is caused. As a consequence, the current fluid volume fractions at any given pipe location can't be determined from input conditions alone. [70]

As shown in Figure 41, with increasing liquid holdup H_L, the overall density increases accordingly while the liquid and gas densities are constant. Moreover, the liquid velocity decreases with increasing holdup and the gas velocity exhibits a noticeable increase, especially at holdup fractions greater than 0.8.

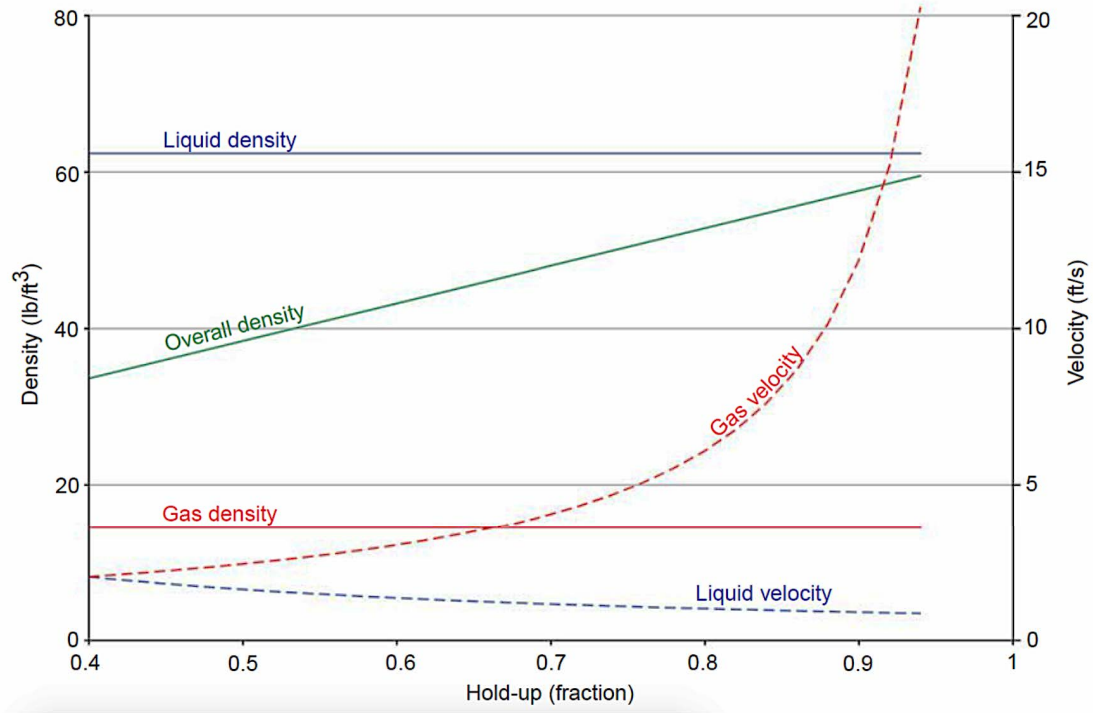

Figure 41: Influence of Liquid Holdup on the respective Velocities and Densities. [51]

3.5.4 Flow Patterns

Multiphase flow also generates the need to address the issue of flow patterns. Depending on whether the pipe is horizontal or vertical, the flow regimes differ accordingly. These regimes depend on flow rates, fluid parameters and several more features, and exhibit great differences in terms of how liquids are moving along.

In horizontal flow, the multiphase mixture separates due to density differences. The heavier fluid gravitates to the bottom, while the lighter fluid stays on top. Figure 42 shows a typical flow regime chart for horizontal flow. Depending on the classification which was used to create such maps, the borders between the individual flow patterns vary and also the naming system is not standardized.

As can be seen in Figure 42, at high gas-liquid ratios, the fluid is transported as a mist along the pipe (referred to as “Annular” and “Dispersed”). [52]

Horizontal flow patterns such as the one shown in Figure 42 by Baker [1954] use complex parameters, such as the Martinelli parameter, the Froude number and often parameters developed by the respective authors.

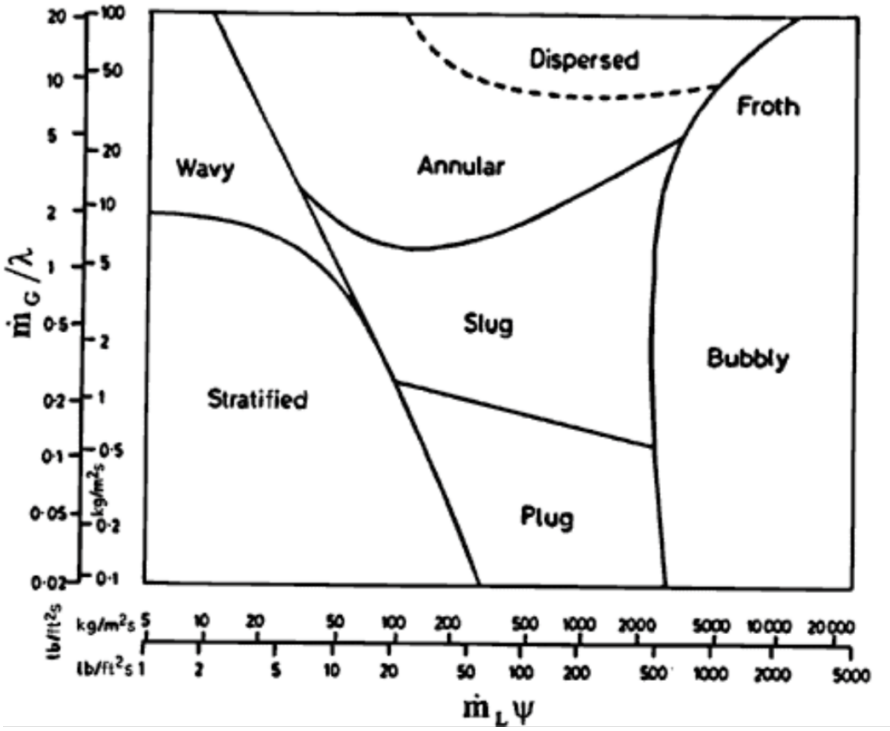

Figure 42: Flow Regime Chart for Horizontal Flow. [66]

In vertical flow, the occurring regime depends on parameters such as flow rate, density, surface tension, pipe geometry, superficial velocity and flow velocity. For gas production operations, mist flow with a continuous gas phase and entrained liquid droplets is preferable in gas production operations.

The Entrained Droplet Model by Turner et al. [1969] is based on the assumption that mist flow is the prevailing flow regime and as a consequence, the methodology and results in this work are only valid for gas wells with mist flow regimes.

Mist flow is charaterized by high gas flow rates. The shear of the gas flow thins the annular liquid film until it is destroyed and all the liquid is entrained as droplets in the continuous gas phase. These droplets are often too small to be seen with the human eye and require special lighting or magnification. [69]

Two methods by Duns and Ros [1963] and by Orkiszewski [1967] to determine flow patterns are discussed in this chapter.

3.5.4.1 Vertical Flow Patterns according to Duns and Ros [1963]

Duns and Ros [1963] describe three regions in their work, as shown in Figure 43. In Region I, the liquid phase is the continuous phase and contains bubble flow, plug flow, and a part of the froth flow. Region II encompasses the remaining froth flow part and slug flow. Here, liquid phases and gas phases alternate.

Finally in Region III, mist flow can be found which is where Turner's equation is valid. In mist flow, the gas phase is continuous. [68]

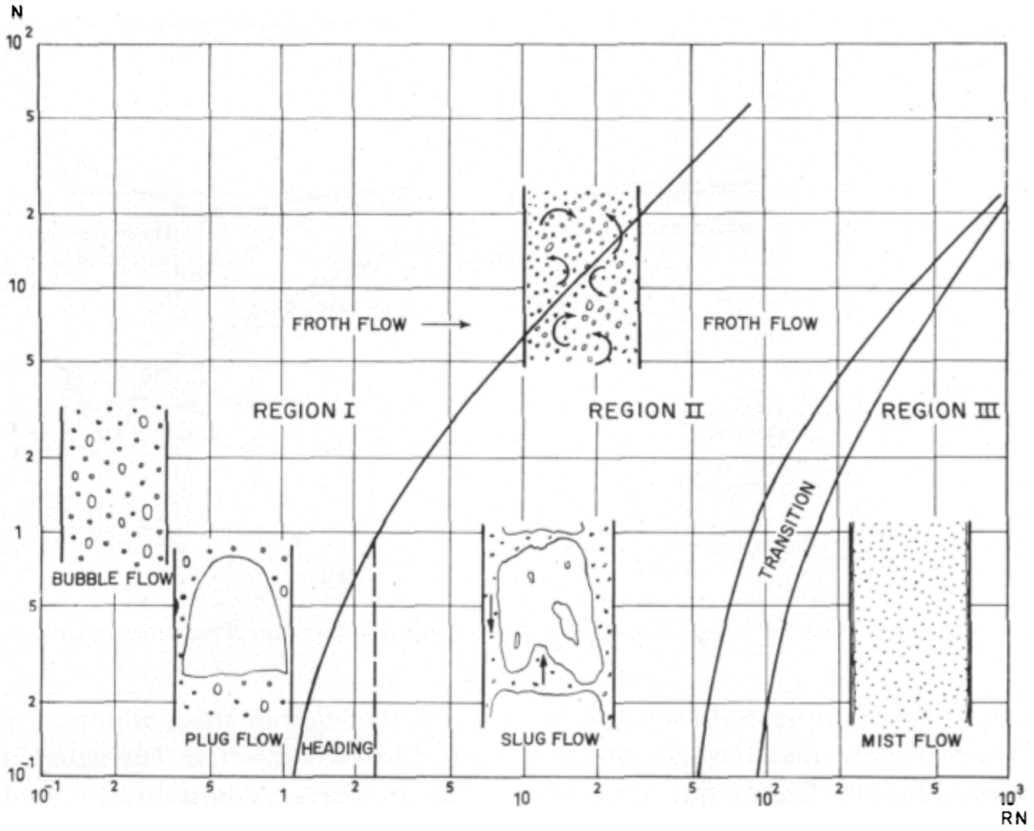

Figure 43: Flow Regime Chart for Vertical Flow according to Duns and Ros [1963].

To be able to investigate the location of calculated values within this chart, this flow regime chart was reproduced as shown in Figure 44. Region I which is characterized by bubble flow is bound by the grey line A_1. Between A_1 and A_2, Region II with prevailing slug flow can be found. This is followed by a transition zone which is located between lines A_2 and A_3. The region on the right-hand side of line A_3 is mist flow, where gas is the continuous phases and where Turner's equation is valid.

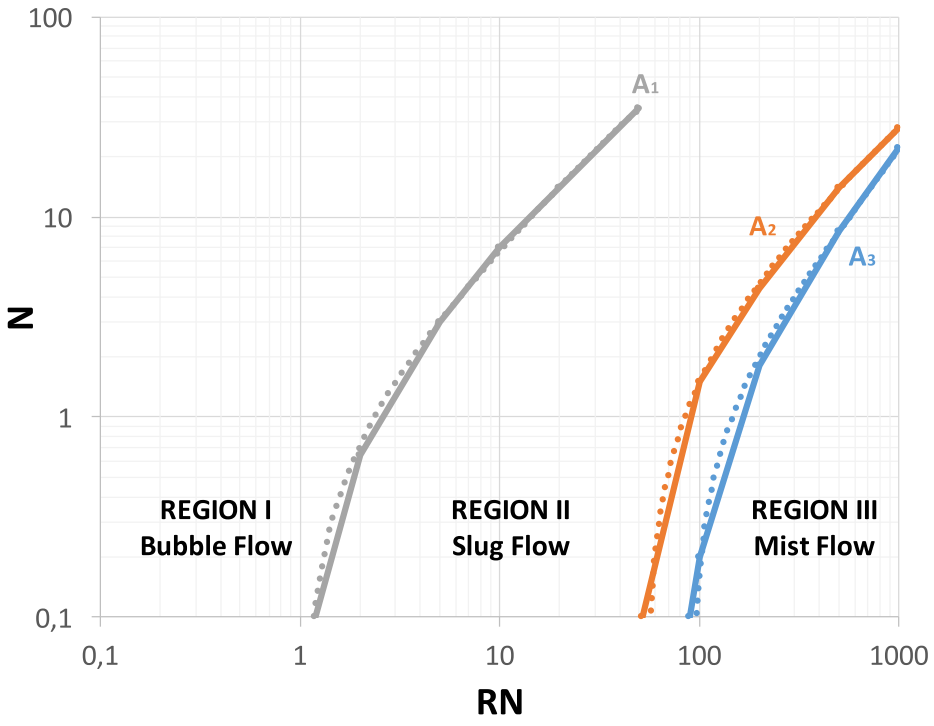

Figure 44: Reproduced Flow Regime Chart for Vertical Flow.

The equations which describe the separation lines are listed below. They were obtained using second degree polynomial functions.

Line A_1:

$$\mathrm{N} = -0{,}00103489\,\mathrm{RN}^2 + 0{,}76752270\,\mathrm{RN} - 0{,}80155700 \tag{133}$$

Line A_2:

$$\mathrm{N} = -0{,}00000285\,\mathrm{RN}^2 + 0{,}03261801\,\mathrm{RN} - 1{,}73790276 \tag{134}$$

Line A_3:

$$\mathrm{N} = 0{,}00000734\,\mathrm{RN}^2 + 0{,}01620020\,\mathrm{RN} - 1{,}52351818 \tag{135}$$

To determine the prevailing flow regime, the two parameters RN and N have to be calculated. The x-axis displays the RN-parameter, while the y-axis shows the N-parameter. The RN-parameter is also referred to as *gas velocity number*, while the N-parameter is the *liquid velocity number*.

These two parameters are defined as follows:

$$RN = v_{S,G} \sqrt[4]{\frac{\rho_L}{g\,\sigma_L}} \tag{136}$$

$$N = v_{S,L} \sqrt[4]{\frac{\rho_L}{g\,\sigma_L}} \tag{137}$$

3.5.4.2 Vertical Flow Patterns according to Orkiszewski [1967]

Orkiszewski [1967] differentiates between bubble flow, slug flow, annular-slug transition and annular-mist flow. In bubble flow, the gas is distributed as small bubbles with varying diameters and has very little influence on the pressure gradient. In slug flow, the liquid phase is still continuous but stable bubbles with a size and shape up to the pipe diameter can form. The transition flow regime is characterized by a predominant gas phase and entrained liquid slugs. The mist flow has a continuous gas phase and the liquid phase is entrained as small droplets which are carried along the gas stream. [67]

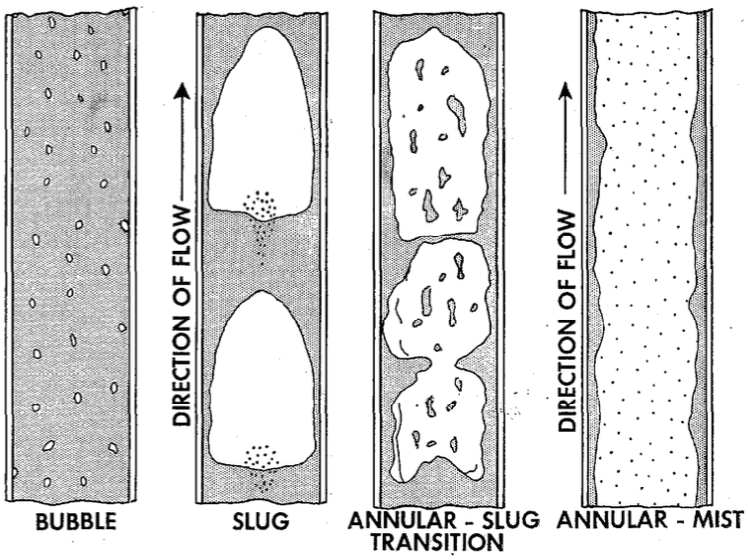

Figure 45: Flow Regime Chart for Vertical Flow according to Orkiszewski [1967].

As shown in Table 6, Orkiszewski [1967] defined the following limits for the related flow regime. These limits are calculated as shown below and depend on parameters such as volumetric flow rates, the pipe geometry, the liquid density, the liquid surface tension and so on.

Table 6: Flow Regimes and the Definition of their Limits. [67]

Flow Regime	Limits
Bubble	$\frac{\dot{V}_G}{\dot{V}_{mix}} < L_B$
Slug	$\frac{\dot{V}_G}{\dot{V}_{mix}} > L_B \; ; \; v_{G,D} < L_S$
Transition	$L_M > v_{G,D} > L_S$
Mist	$v_{G,D} > L_M$

The required parameters are defined as follows. The gas velocity $v_{G,D}$, the bubble-slug boundary L_B, the transition-mist boundary L_M and the slug-transition boundary L_S are all dimensionless.

$$v_{G,D} = \frac{\dot{V}_G}{A_P} \sqrt[4]{\frac{\rho_L}{g\,\sigma_L}} \tag{138}$$

$$L_B = 1.071 - (0.2218 \frac{\dot{V}_{mix}^2}{A_P^2 d_P}) \tag{139}$$

$$L_S = 50 + 36 \frac{v_{G,D}\,\dot{V}_W}{\dot{V}_G} \tag{140}$$

$$L_M = 75 + 84 \left(\frac{v_G\,\dot{V}_W}{\dot{V}_G} \right)^{0.75} \tag{141}$$

4 Results

All previously mentioned concepts, models and correlations were combined and programmed into a versatile tool which was realized in MS Excel using Visual Basic (see Appendix B). The tool allows as a main result the calculation of pressure and temperature values for every point within the wellbore. This in turn enables, among all other desired parameters, the determination of the actual fluid velocity v, the critical velocity v_c and the Turner velocity v_T. The Turner velocity v_T is calculated based on the formula for the critical velocity v_c, but uses Turner's original values from 1969. The critical velocity v_c is calculated by using the accurate values for each point in depth and thus, it is more representative than the Turner velocity v_T.

$$v = \frac{\dot{m}}{A\,\rho} \tag{142}$$

$$v_c = \left[\frac{4\,g\,\sigma_L\,We_c\,(\rho_L - \rho_G)}{3\,C_D\,\rho_G^2\,s\,n(\alpha)}\right]^{1/4} \tag{143}$$

The mass flow rate $\dot{m}$ depends on the volumetric flow rate and the density at the surface. As mentioned in Chapter 3.2, the mass flow rate is assumed to be constant and no losses of mass occur.

Moreover, the tool calculates numerous parameters for each point in depth. These parameters include the following as seen in Table 7. Additionally, the mass flow rate and the density at standard conditions are calculated for both gas and water.

Table 7: Parameters calculated by the MS Excel Tool.

Basic Parameters	Earth temperature Casing wall temperature Annulus temperature Tubing wall temperature Fluid temperature Pressure in tubing Pressure in annulus Fluid velocity Critical velocity Turner velocity Flow regime parameters after Duns and Ros [1968]
Flow Parameters	Fluid density Fluid viscosity Heat capacity Thermal conductivity Joule-Tomson coefficient Friction factor Pressure losses (friction, hydrostatic, acceleration)

Non-Dimensional and Thermal Parameters	Prandtl number Reynolds number Nusselt number Grashof number Thermal conductivities and resistances for individual components

The required input parameters are listed in Table 8. All of these parameters can be adjusted to reflect any desired scenario. This is done in Chapter 4.3, where six different scenarios are investigated.

Table 8: Input Parameters required by the MS Excel Tool.

Earth Parameters	Surface temperature Geothermal gradient
Production Parameters	Specific gas gravity Bottom hole flowing temperature Bottom hole flowing pressure* Wellhead flowing pressure* Gas production rate* Water production rate
Borehole Parameters	Borehole depth Borehole diameter Casing OD Casing wall thickness Tubing OD Tubing wall thickness Insulation thickness Cement conductivity Casing conductivity Tubing conductivity Insulation conductivity Emissivity coefficient
Annular Parameters	Fluid in annulus above packer Nusselt number
Simulation Parameters	Number of iterations Section length

Concerning the three production parameters (Bottom hole flowing pressure, Wellhead flowing pressure, Gas production rate) which are marked with an asterisk (*), the procedure works as follows. Two of these three parameters have to be supplied, and depending on the provided values, the magnitude of the third (missing) parameter which is marked as *t.b.d.* (to be determined) in the respective tables (Tables 10-15) is calculated.

To allow for better comparability, the following parameters remain the same for all scenarios presented in this work:

- Surface temperature: 15 °C
- Geothermal gradient: 3 °C/100 m
- Bottom hole flowing temperature: 105 °C
- Borehole depth: 3000 m (vertical well)
- Borehole diameter: 8.5 inch
- Casing OD: 7 inch
- Casing wall thickness: 0.28 inch
- Section length: 50 m

Also, several assumptions had to be made. Phase changes from liquid phases to gaseous phases are not considered (e.g. between oil or condensate and natural gas, or between water and steam). Additionally, water is assumed to stay liquid up to temperatures of 200 °C. Moreover, if a liquid phase exists, it will be water and not oil or condensate. Finally, the simulations were conducted for a vertical well.

The emissivity coefficient of steel is assumed to be 0.5, which depends on factors such as age, corrosion, etc. according to several values found in the literature. [72]

The thermal conductivity for steel is 16 W/m°K and 0.045 W/m°K for fiberglass (GFK). [73]

Finally, the natural gas considered in this work is a dry gas, meaning that it does not form a liquid phase at production conditions [60]. However, for the testing of Turner's equation, water will be added for simulation purposes.

4.1 Constant Flow Rate

In a first analysis, the tool was used to examine the behaviour of a vertical wellbore drilled to a gas reservoir in a depth of 3000 m. The initial conditions of this scenario include a reservoir pressure of 300 bar and, due to a geothermal gradient of 3°/100m, a reservoir temperature of 105 °C.

A constant production rate of 100,000 Nm^3 per day is assumed. No water or condensate is being produced.

The material used for casing and tubing is steel with an emissivity ε of 0.50. To demonstrate the influence of heat loss, the insulation thickness varies between 0 and 1 inch in steps of 0.2 inch; perfect insulation was simulated as well.

The chosen insulation material is rigid polyurethane foam with a thermal conductivity of 0.02 W/m°K. Further details are provided in Table 9. [3]

Table 9: Summary of Data.

Spec. Gravity of Gas, -	0.7
Borehole Diameter, inch	8.5
Casing Outer Diameter, inch	7
Casing Wall Thickness, inch	0.28
Tubing Outer Diameter, inch	2.375
Tubing Wall Thickness, inch	0.2175
Insulation Conductivity, W/m°K	0.02
Cement Conductivity, W/m°K	2
Casing Conductivity, W/m°K	16 (steel)
Tubing Conductivity, W/m°K	16 (steel)

The results of the simulation are shown in the following figures as a function of depth. Figure 46a shows that the temperature of the surrounding formation (dashed line) increases linearly with depth in accordance with the geothermal gradient until it reaches the 105 °C of the reservoir. The other lines indicate the temperature behaviour of the gas depending on the insulation thickness.

Without any insulation, the temperature is reduced from 105 °C to 25 °C at the surface. This represents a significant temperature reduction and an irrecoverable loss of heat energy into the surrounding formation. This issue can be somewhat remedied by using insulation.

With the use of (unobtainable) perfect insulation, the surface temperature still reads about 89 °C. The cooling is caused by the inevitable outcome of the Joule-Thomson effect due to the expansion of the gas.

Comparing this result to an insulation of 1 inch, the wellhead temperature still reads about 55 °C. Thus, with this measure, a temperature increase of 30 °C compared to the no-insulation-scenario can be achieved. This is a significant difference with noticeable influences on the gas properties.

The temperature changes influence other parameters too, as was expected. In Figure 46b, a pressure variation of about 6 bar can be observed between the variations of no insulation and 1 inch insulation.

Actual and critical gas velocities (Figure 47c and Figure 47d) also exhibit noticeable variations. While the differences in actual gas velocities between no insulation and perfect insulation (roughly 0.9 m/s), and between no insulation and 1 inch insulation (about 0.3 m/s) may seem small, this additional actual velocity can be of great value; especially towards the end of the lifetime of a gas well.

The critical gas velocity varies as well. It shows that an increase in insulation thickness also increases the critical gas velocity by a minor amount. This critical velocity increase, however, is smaller than the actual gas velocity increase gained by insulation and is therefore offset by this change.

The velocity ratios between actual gas velocity and critical gas velocity indicate as well that the variations turn out to be in favor of increasing actual gas velocities. While the critical velocities increase as well, they do so at a slower pace and thus, a positive trend towards higher actual gas velocities can be observed.

This shows that better insulation is preferable due to higher gas velocities and higher gas temperatures at the wellhead. Higher temperatures result in higher pressure readings and also a higher flowrate, and also more favorable gas properties.

Finally, according to Eq.(110), the surface tension solely depends on temperature (Figure 47e). Thus, this parameter is sensitive to any changes caused by insulation variations and behaves accordingly.

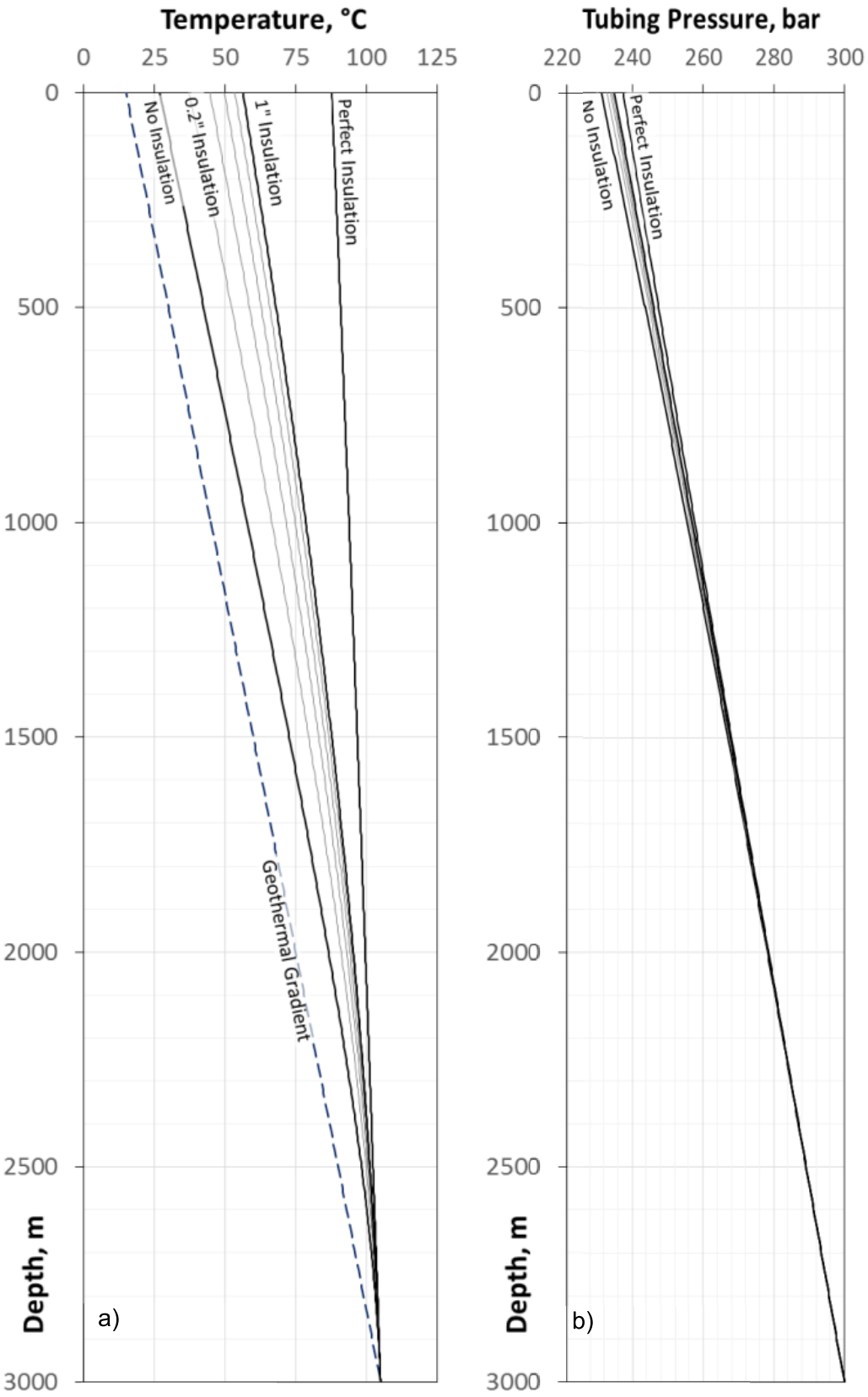

Figure 46: Simulation Results (Temperature and Pressure) for Constant Flow Rate.

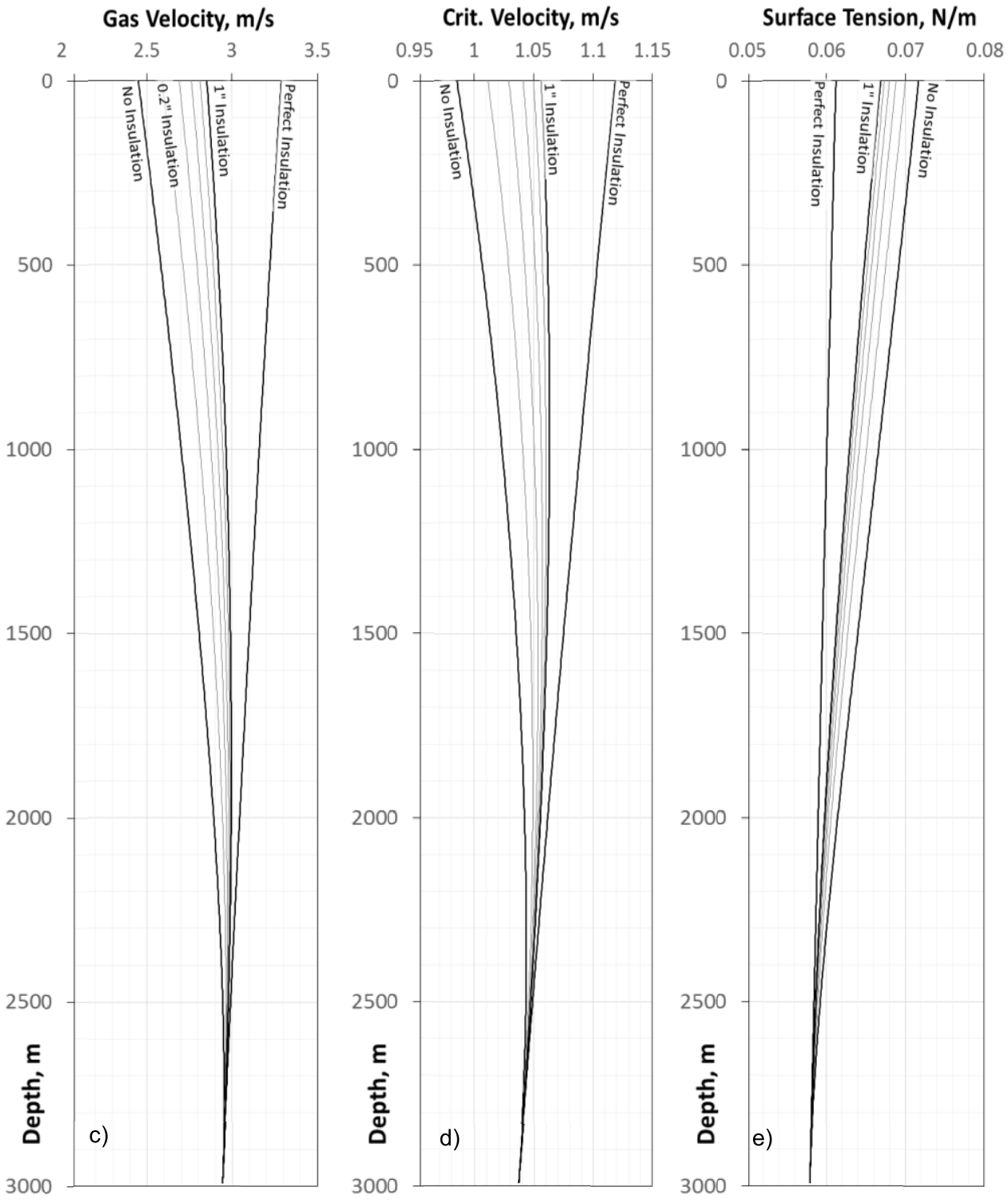

Figure 47: Simulation Results (Velocities and Surface Tension) for Constant Flow Rate.

4.2 Constant Wellhead Pressure

For the second analysis, a wellhead pressure of 80 bar was taken as a desired constant value which is a more reasonable setting in terms of real-life applications. Figure 48 shows on the y-axis the required reservoir pressure to achieve the prerequisite of 80 bar wellhead pressure as a function of the gas flow rate (x-axis). Also plotted are the curves for 0 inch, 1 inch and perfect insulation. The results demonstrate that an increase in flow rate requires a higher reservoir pressure to maintain 80 bar at the wellhead. Again, the well is assumed to be vertical and to produce no liquids.

Up to a certain gas flow rate (roughly 100,000 Nm^3/day), a difference between the three insulation variations can be detected: Better insulation requires a lower reservoir pressure while still being able to achieve 80 bar all the way up at the surface.

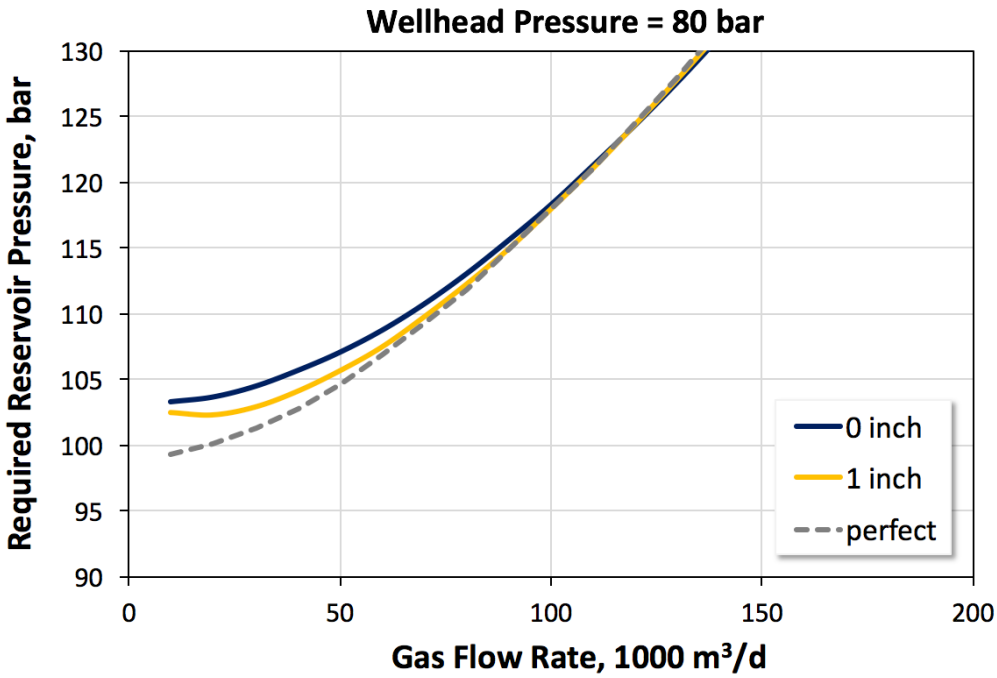

Figure 48: Simulation Results of Required Reservoir Pressure for Constant Wellhead Pressure.

Figure 49 shows the gas temperature at the wellhead (y-axis) as a function of the gas flow rate (x-axis). What can be observed is that an increase in flow rate yields an increased wellhead gas temperature. This behaviour can be attributed to the subsequent increase in flow velocity and the decreased interaction time of the gas with the surrounding formation in terms of heat transfer.

The increase in gas temperature at the wellhead is especially noticeable for the 1 inch insulation. The perfect insulation shows an overall high temperature which slowly decreases; this effect can be attributed to the JT effect which clearly demonstrates that neglecting the influence of the JT effect can cause misleading and non-representative results.

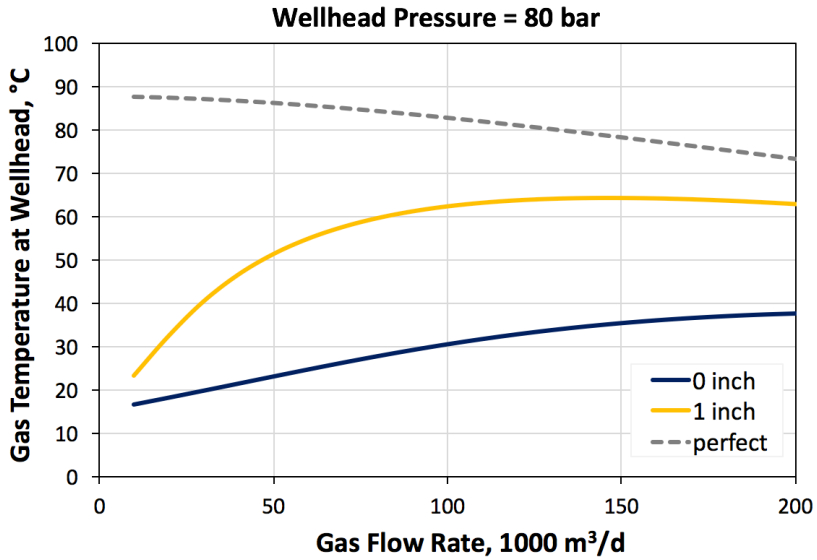

Figure 49: Simulation Results of Gas Temperature at the Wellhead for Constant Wellhead Pressure.

Figure 50 shows the increase in required minimum gas velocity with increasing gas flow rate. The variations due to different insulation scenarios are rather minor in this setting.

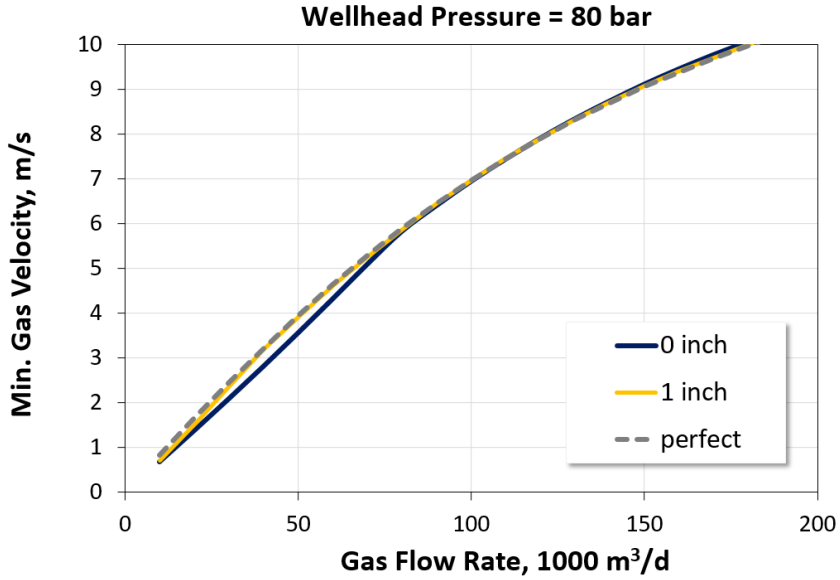

Figure 50: Simulation Results of Minimum Gas Velocity for Constant Wellhead Pressure

4.3 Scenario Variations

In the third and final analysis, six scenarios with realistic aspects and problems which gas well engineers might face are simulated. Since this work is based on the concept presented by Turner et al. [1969], it was ensured that the design of the scenarios enables the application of the *Turner equation*. Specifically, this means that mist flow or near-mist flow conditions have to be the case.

The scenarios are investigated by applying the MS Excel Tool and by simulating the effects of insulation, increased water production and other problems associated with liquid loading.

Moreover, based on this reasoning, the default specific gas gravity is 0.6 and the default outer diameter of the tubing is 2 3/8 inch.

Concerning the water production rate, this is realized as a proportional value of the gas production rate. The unit for the water rate is *Ncm^3 of water per Nm^3 of gas* (or Ncm^3/Nm^3 in short). This means that e.g. a water cut of 50 Ncm^3/Nm^3 coupled with a gas production rate of 150,000 Nm^3/d results in a daily water production of 7.5 Nm^3.

Also, the annular fluid in the following six scenarios is assumed to be gas. The simulation was carried out for water as annular fluid as well, but the results yielded only minor differences between those two annular fluids.

Moreover, each of these six scenarios are calculated by varying several parameters. The results of these variations in each scenario are discussed after the investigation of a so-called “reference case”. This reference case is the variation with the most representative value-set and it is discussed in more detail.

The pressure loss calculations are performed by taking friction, hydrostatic and acceleration losses into account. However, the acceleration pressure losses turn out to be less than 1 bar for a 3000 m deep vertical well in all six scenarios.

The flow regime conditions are plotted in the flow pattern chart by Duns and Ros [1963]. This is of special importance as Turner’s equation was developed and conceived for mist flow regimes.

4.3.1 Scenario 1

In the first scenario, the influence of an increasing amount of produced water is simulated. This represents a realistic setting since an increased water production is a phenomenon that is occuring on all gas wells during their lifetime.

The 3,000 m vertical well in this scenario is assumed to have a wellhead flowing pressure of 60 bar and a planned daily gas production rate of 400,000 m^3. Moreoever, the well has to deal with water production rates ranging from 0 to 100 Ncm^3 per Nm^3 of gas; this means that 21 variations concerning the water production rates are simulated. Thus, the required bottom hole flowing pressure to reach these gas rates under these conditions is calculated for 21 variations.

Table 10 shows all parameters of this scenario.

Table 10: Setup of Properties for Scenario 1.

Properties	Scenario 1
Spec. Gravity of Gas, -	0.6
Bottom Hole Flowing Pressure, bar	t.b.d.
Wellhead Flowing Pressure, bar	60
Gas Production Rate, Nm^3/d	400000
Water Production Rate, Ncm^3/Nm^3	0, 5, 10...100
Tubing Outer Diameter, inch	2 3/8
Tubing Wall Thickness, inch	0.2175
Insulation Thickness, inch	0
Cement Conductivity, W/m°K	2
Casing Conductivity, W/m°K	16 (steel)
Tubing Conductivity, W/m°K	16 (steel)
Insulation Conductivity, W/m°K	0.02
Annular Fluid (Water / Gas)	G
ignore JT effect?	no
ignore formation heat transfer?	no
ignore kinetic energy term?	no

As shown in Figure 51, the reference case with a water production rate of 50 Ncm^3/Nm^3 starts at the bottom of the well in the transition region (yellow color) and experiences a mist flow regime near the surface (red color), with a required bottom hole flowing pressure (BHFP) of about 195 bar. This means that the Turner equation is sufficiently valid for velocity calculations which are shown in Figure 52.

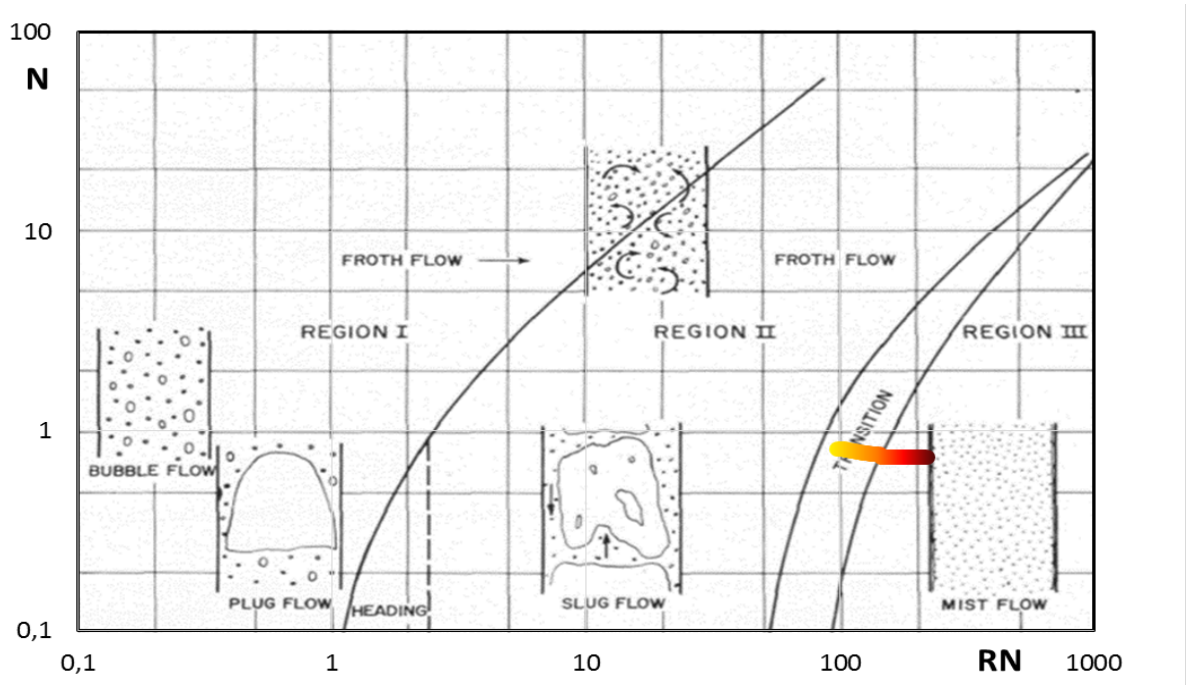

Figure 51: Flow Pattern Chart of the Reference Case according to Duns and Ros [1963].

In Figure 52, the temperature of the surrounding earth, T_e, is indicated as a red dashed line and behaves according to the geothermal gradient. As shown, the earth temperature and the fluid temperature, T, both are 105 °C at the depth of 3,000 m. At the surface, T_e equals the surface temperature of 15 °C while the fluid has a temperature of 18.3 °C. This significant cooling down was not hindered by any insulation.

The tubing pressure, p, at the wellhead is 60 bar, as specified. To obtain a flowrate of 400,000 Nm^3, a bottomhole flowing pressure of 195 bar was determined. As discussed in the next paragraphs, the largest pressure losses occur due to friction losses (about 108 bar). Hydrostatic pressure losses account for about 28 bar and the acceleration losses are minor with less than 1 bar.

The velocity v of the fluid stream varies between 15 and 36 m/s. This speed clearly exceeds both the critical velocity v_C and the Turner velocity v_T which range between 1 and 3 m/s. Therefore, liquid loading under these conditions is not to be expected.

The fluid density den has its highest value at the bottom of the well and it is 123 kg/m^3. Going up the tubing, the density steadily decreases and is 52 kg/m^3 at the surface.

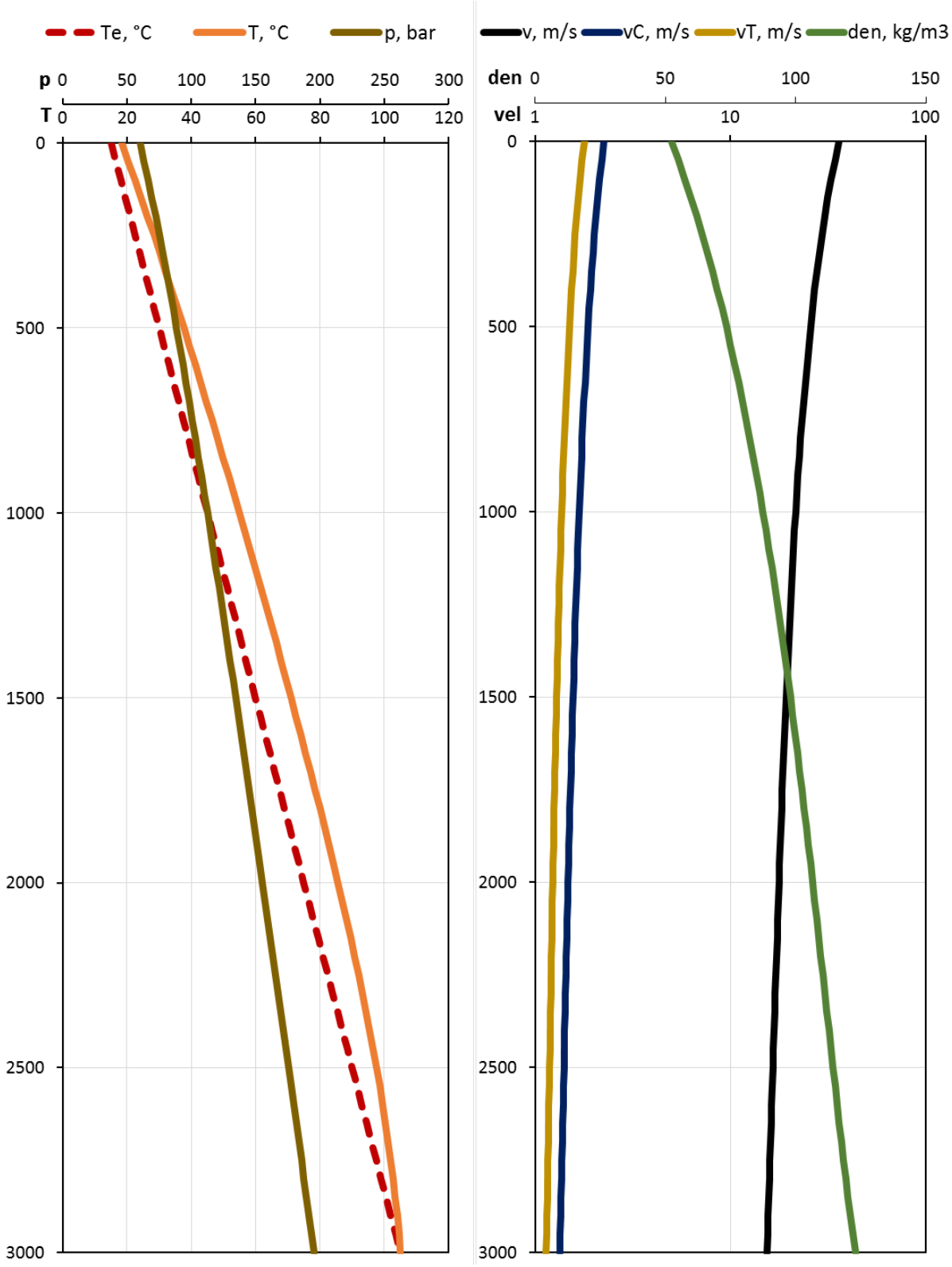

Figure 52: Temperature, Pressure, Velocity and Density Curves of the Reference Case.

In Figure 53, each dot on the yellow line belongs to a dot on the red line. The dots on the yellow line mark the flow regime at the bottom of the well (at 3,000 m depth) while dots on the red line indicate the flow conditions at the top of the well, near the wellhead. In total, 21 variations with different water production rates ranging from 0 to 100 Ncm^3/Nm^3 are shown in this graph. Thus, it can be seen that at the top of the wells for each of the variations, the flow regime was determined to be mist flow while the bottom of the well experiences a range of mist flow, transition and slug/froth flow. An increasing water production rate causes the flow regime at the bottom to change from mist flow to transitional and even into froth flow.

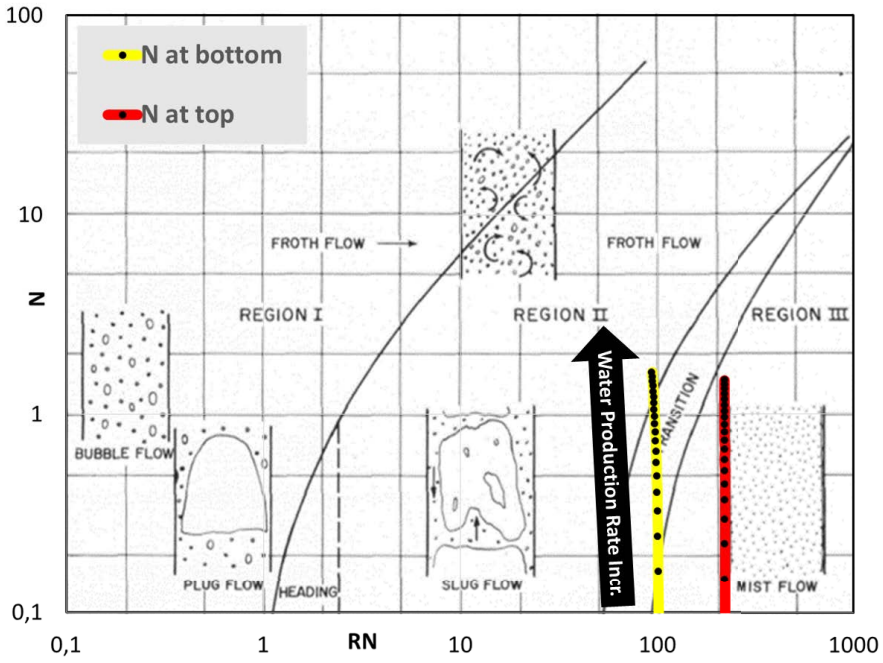

Figure 53: Duns and Ros [1963] Flow Pattern Chart of all Scenario Variations.

Pressure losses as a function of on an ever-increasing water production rate are shown in Figure 54. The total pressure losses ΔP_total due to hydrostatic, friction and acceleration effects for a gas production rate of 400,000 m^3 per day range from 126 to 144 bar. Again, friction pressure losses $\Delta P\_fr\ ct\ on$ account for the largest fraction, ranging from 101 to 113 bar. Hydrostatic pressure ΔP_hydro losses amount to 25 to 30 bar. Finally, the acceleration losses are minor with 0.3 to 0.4 bar. In general, the behaviour is rather linear and as expected. With an increasing amount of water, the pressure losses increase accordingly.

In Figure 55, it can be seen that higher water cuts require a higher bottomhole flowing pressure $p\ HF$ to compensate for the increased weight of the fluid stream. Finally, an increased water cut also results in a decrease of fluid temperature at the wellhead (Tf, WH); however, this influence is quite small.

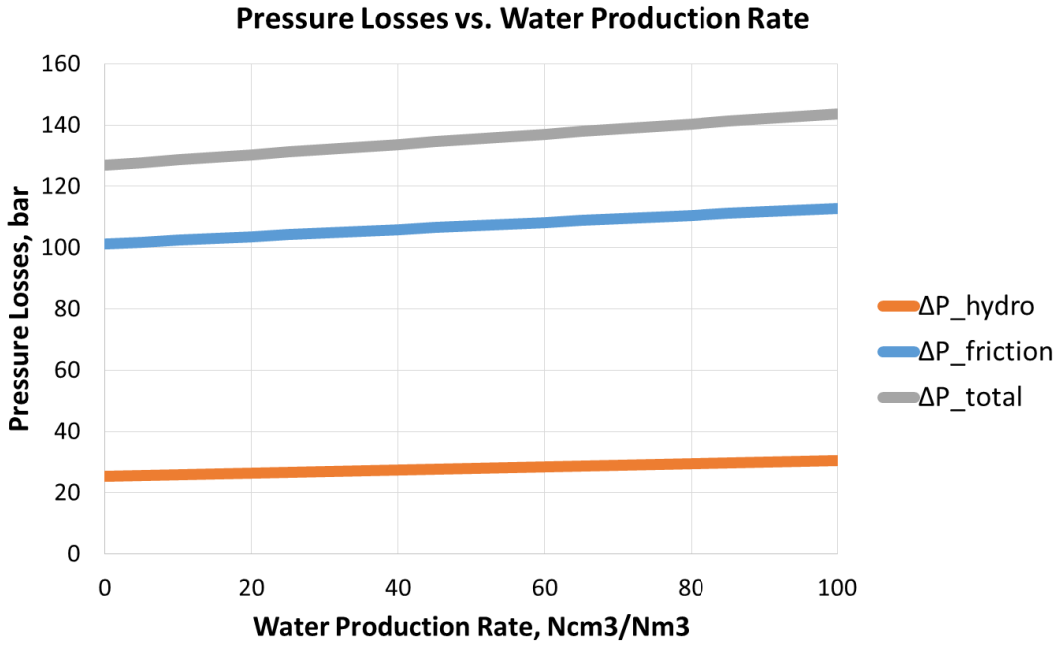

Figure 54: Pressure Losses vs. Water Production Rate.

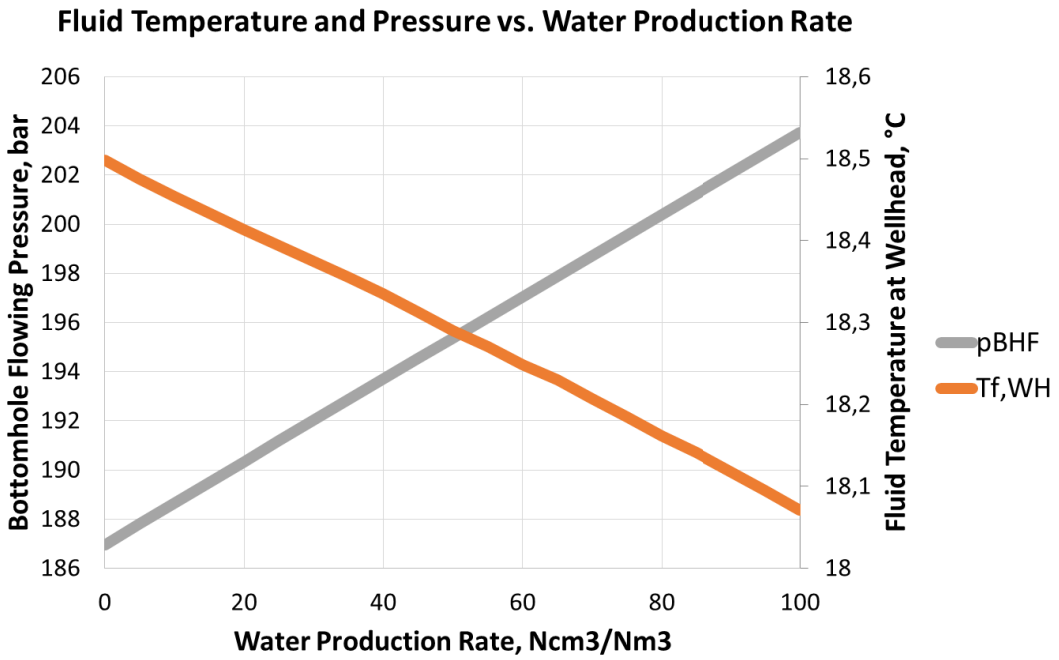

Figure 55: Wellhead Fluid Temperature and Bottomhole Flowing Pressure vs. Water Production Rate.

4.3.2 Scenario 2

In the second scenario, a decreasing bottomhole flowing pressure is simulated. The bottomhole pressure is varied between 300 and 100 bar, in 10 bar steps. Since reservoir pressure decline is an inevitable process, the results are applicable to real-world scenarios.

The simulation is done in combination with a water production rate of 50 Ncm^3/Nm^3. The desired wellhead pressure is set at 80 bar, with a tubing OD of 2 3/8 inch and without insulation. Again, the specific gas gravity is set at 0.6.

Table 11 shows all parameters of this scenario.

Table 11: Setup of Properties for Scenario 2.

Properties	Scenario 2
Spec. Gravity of Gas, -	0.6
Bottom Hole Flowing Pressure, bar	300, 290, 280...100
Wellhead Flowing Pressure, bar	80
Gas Production Rate, Nm^3/d	t.b.d.
Water Production Rate, Ncm^3/Nm^3	50
Tubing Outer Diameter, inch	2 3/8
Tubing Wall Thickness, inch	0.2175
Insulation Thickness, inch	0
Cement Conductivity, W/m°K	2
Casing Conductivity, W/m°K	16 (steel)
Tubing Conductivity, W/m°K	16 (steel)
Insulation Conductivity, W/m°K	0.02
Annular Fluid (Water / Gas)	G
ignore JT effect?	no
ignore formation heat transfer?	no
ignore kinetic energy term?	no

Figure 56 shows a similar behaviour like the reference case in scenario 1. This reference case has a bottomhole flowing pressure of 200 bar and the aforementioned 50 Ncm^3/Nm^3 water cut. With these parameters, the well experiences a flow regime classified as transition between slug/froth flow and mist flow from top of the well (red color) to the bottom (yellow color). Therefore, the Turner equation is not entirely applicable but can still be used as a guideline to interprete critical velocities.

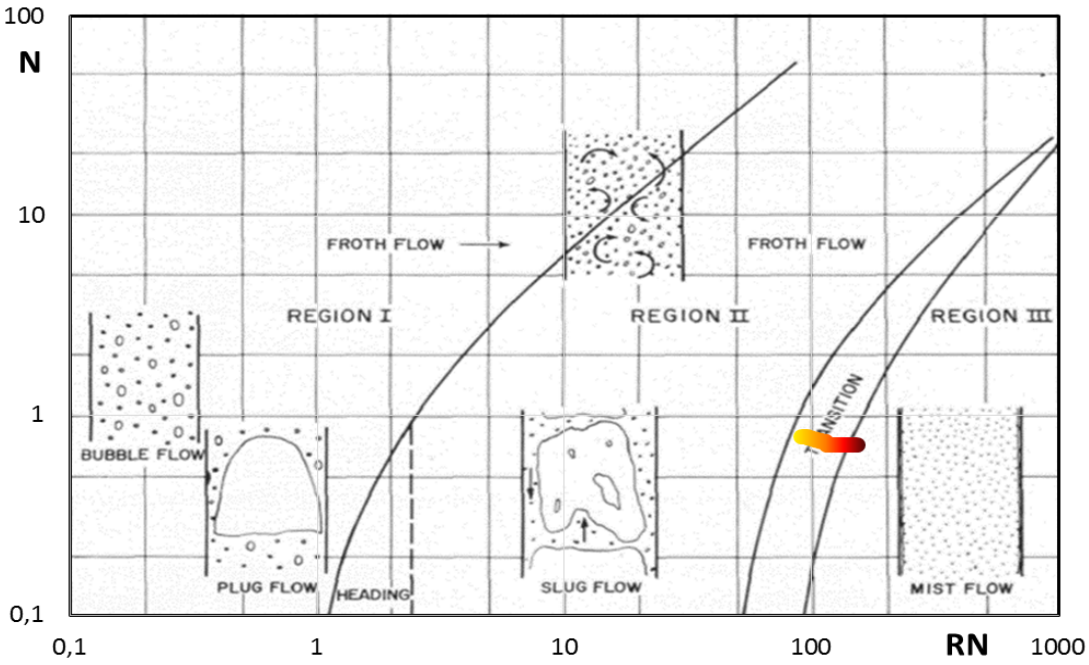

Figure 56: Flow Pattern Chart of the Reference Case according to Duns and Ros [1963].

In Figure 57, the dashed red line represents the earth temperature, T_e. It can be seen that it heavily influences the fluid temperature, T, since the tubing is not insulated and heat exchange with the surrounding formation is unhindered. After starting at 105 °C, the fluid temperature decreases continuously until it reaches about 21 °C at the wellhead.

In this reference case, the pressure p at the wellhead is set at 80 bar, while the bottomhole flowing pressure is 200 bar. Taking the water production rate of 50 Ncm^3/Nm^3 into account, this scenario yields a flowrate of about 383,000 Nm^3/d. To allow for this gas flowrate, a friction pressure loss of 90 bar in total has to be overcome. The hydrostatic term is about 31 bar and the acceleration losses are small with about 0.2 bar.

The fluid velocity v shows a range of 14 to 25 m/s over the entire range of the wellbore. The critical (v_C) and Turner velocity (v_T) are 1.3 to 1.9 m/s and 1.1 to 1.5 m/s, respectively. Again, it can be seen that the actual fluid velocity easily surpasses those two parameters and fluid removal is to be expected.

From bottom to top, the density of the gas-water mixture $dens$ varies between 71 and 126 kg/m^3 and shows a gradual decline.

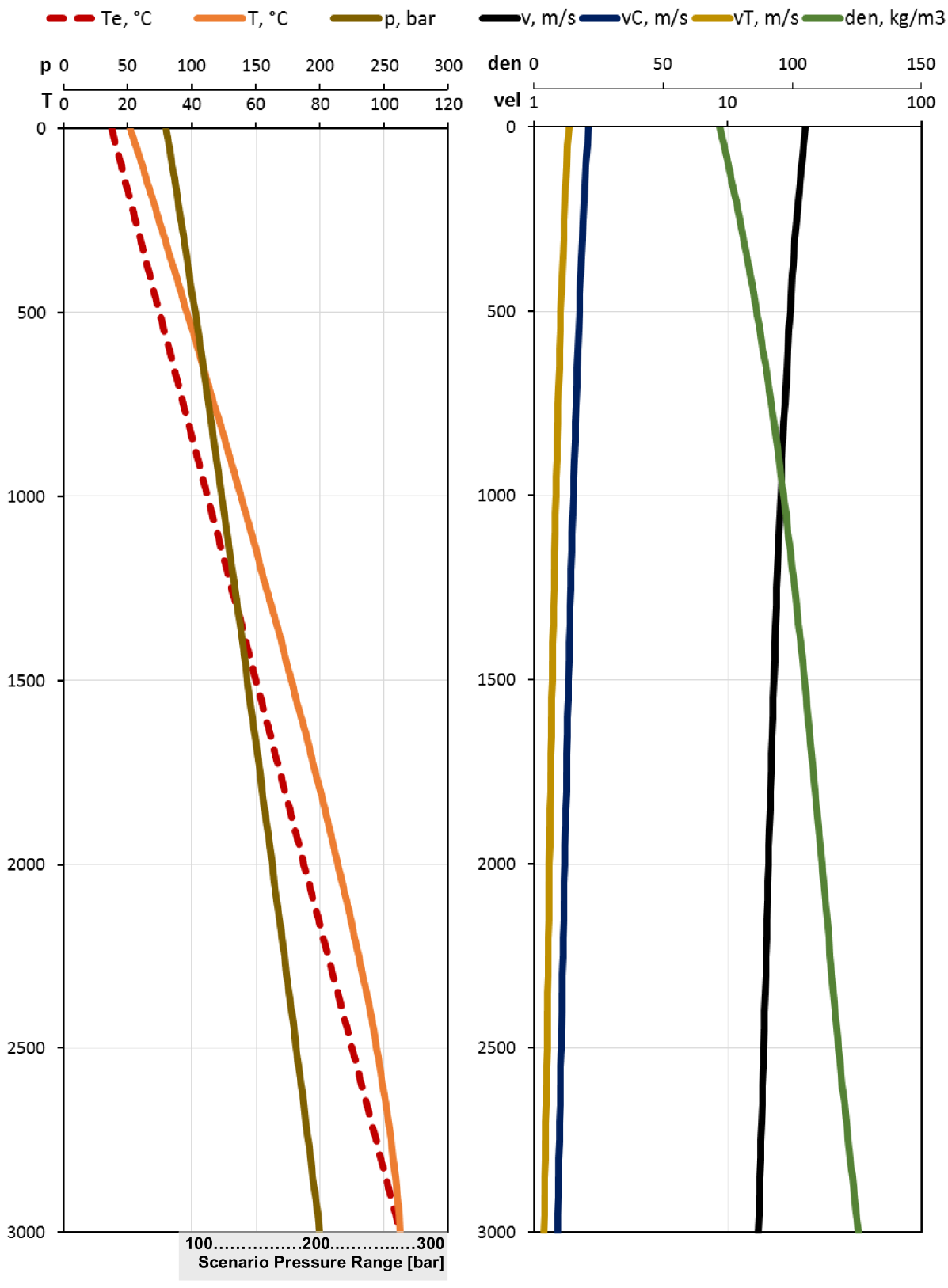

Figure 57: Temperature, Pressure, Velocity and Density Curves of the Reference Case.

Figure 58 shows the top (red) and bottom (yellow) flow regime conditions of 21 variations in bottomhole flowing pressure and accordingly, in gas production rate. With decreasing bottomhole flowing pressure, the flow regimes move into the slug flow region, with almost no difference between top and bottom. At higher bottomhole flowing pressures starting at about 140 bar, the difference becomes more pronounced and the flow regime within the tubing varies between mist flow and transition flow.

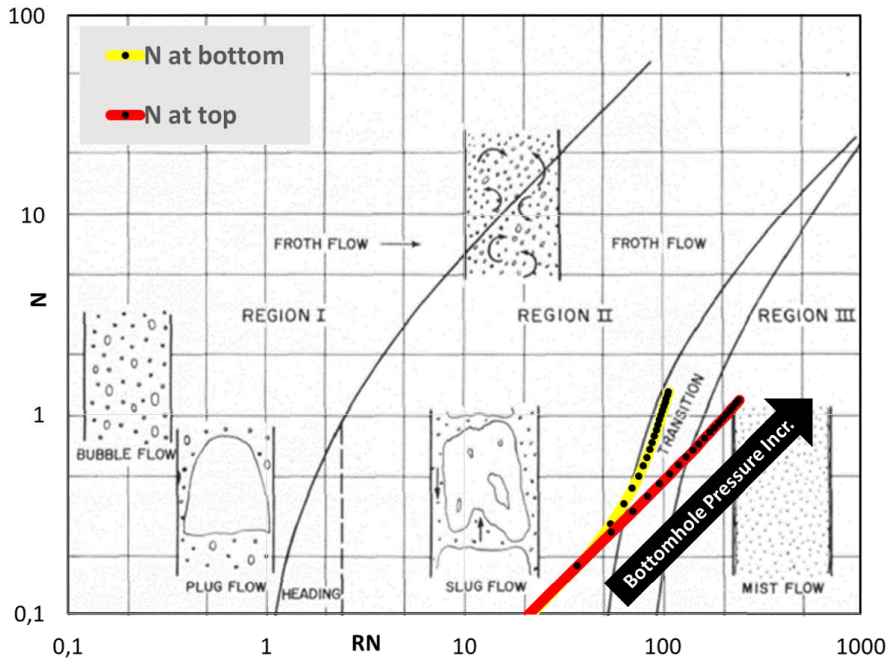

Figure 58: Duns and Ros [1963] Flow Pattern Chart of all Scenario Variations.

Figure 59 shows the pressure losses of the 21 variations as a function of the daily gas production rate. Over the range of 8,000 to 640,000 Nm^3/d of gas production, the losses increase with increasing gas rate. The hydrostatic losses ΔP_hydro vary between about 20 to 40 bar and the friction losses $\Delta P\_fr\ ct\ on$ amount to 10 to 180 bar. Thus, the entire pressure losses ΔP_total range from 30 to 220 bar. As shown, the hydrostatic losses increase only slowly, with friction losses being responsible for the largest part for the additional pressure losses.

In Figure 60, the bottom hole flowing pressure (left vertical axis) and the wellhead fluid temperature (right vertical axis) are plotted against the daily gas production rate. Interestingly, the fluid temperature at the wellhead, Tf,WH, initially increases, reaches its maximum temperature of 22.3 °C at a gas rate of 240,000 Nm^3/d and then declines. The bottomhole flowing pressure ($p\ \ HF$) steadily increases to sustain a higher flowrate of gas.

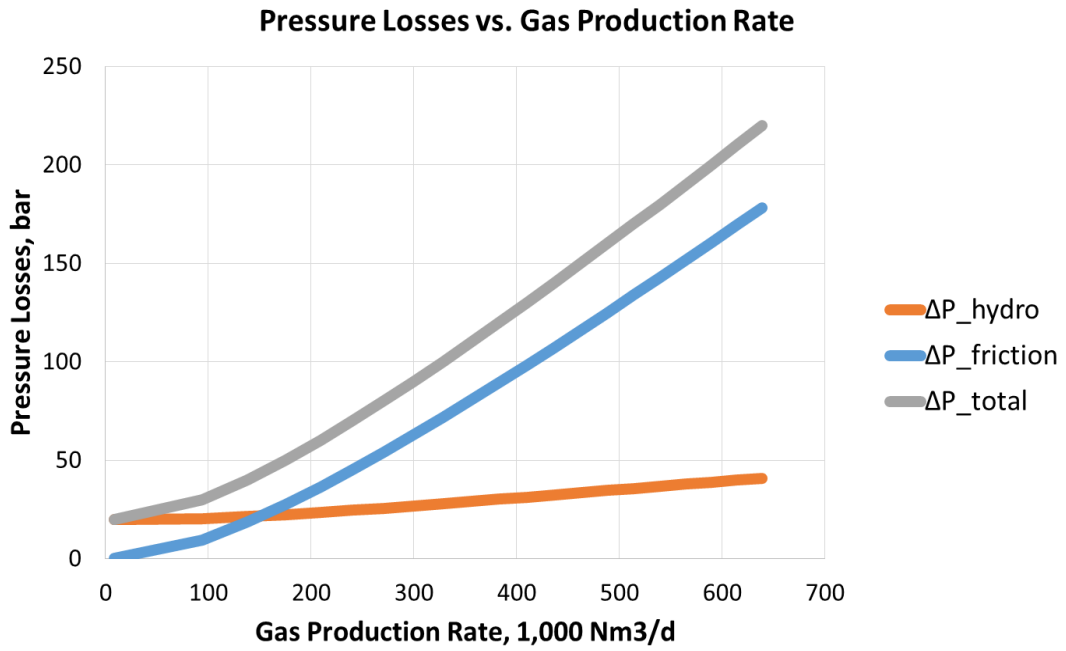

Figure 59: Pressure Losses vs. Gas Production Rate.

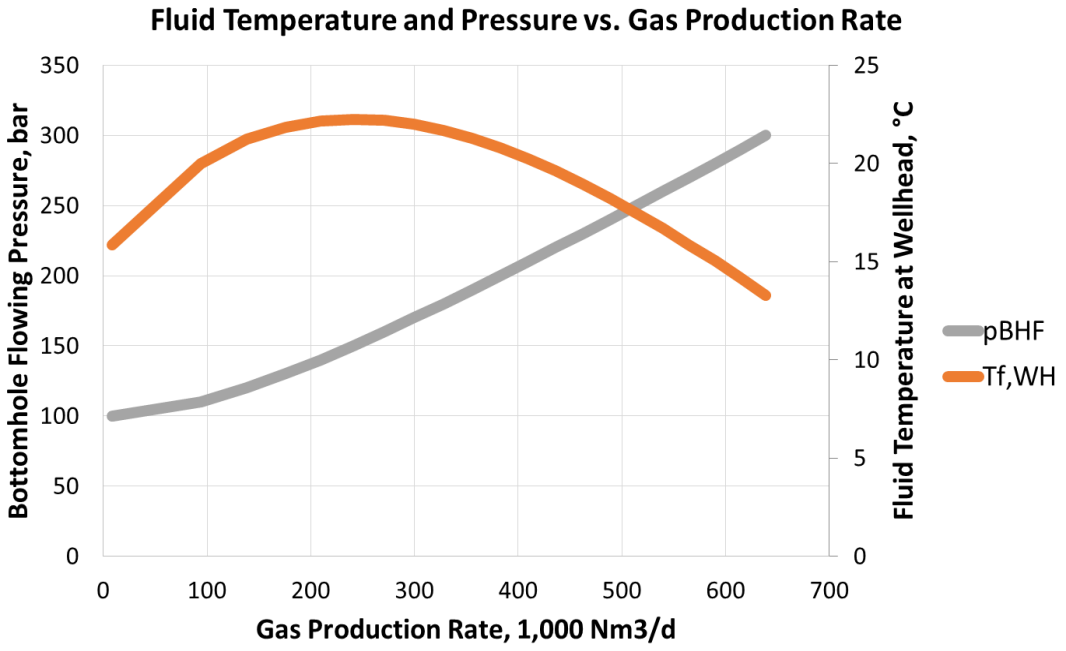

Figure 60: Wellhead Fluid Temperature and Bottomhole Flowing Pressure vs. Gas Production Rate.

4.3.3 Scenario 3

In the third scenario, the influence of the specific gravity of the gas on the gas production rate is investigated. The specific gas gravity is varied between the common values of 0.55 through to 0.75.

The bottomhole flowing pressure is set at 200 bar and the wellhead flowing pressure at 60 bar. This is coupled with a water production rate of 50 Ncm^3/Nm^3 since almost all gas wells experience liquid production.

Table 12 shows the parameters of this scenario.

Table 12: Setup of Properties for Scenario 3.

Properties	Scenario 3
Spec. Gravity of Gas, -	0.55, 0.56, 0.57...0.75
Bottom Hole Flowing Pressure, bar	200
Wellhead Flowing Pressure, bar	60
Gas Production Rate, Nm^3/d	t.b.d.
Water Production Rate, Ncm^3/Nm^3	50
Tubing Outer Diameter, inch	2 3/8
Tubing Wall Thickness, inch	0.2175
Insulation Thickness, inch	0
Cement Conductivity, W/m°K	2
Casing Conductivity, W/m°K	16 (steel)
Tubing Conductivity, W/m°K	16 (steel)
Insulation Conductivity, W/m°K	0.02
Annular Fluid (Water / Gas)	G
ignore JT effect?	no
ignore formation heat transfer?	no
ignore kinetic energy term?	no

Figure 61 depicts the flow regime along the entire wellbore from bottom (yellow) to top (red) with a specific gas gravity of 0.65. The water cut of 50 Ncm^3/Nm^3 once again results in a combination of mist flow at the top of the well and transition flow at the bottom. The bottomhole flowing pressure is 200 bar which combined with a wellhead flowing pressure of 60 bar yields a daily gas production rate of 396,000 Nm^3. In total, this means a daily water production of about 20 Nm^3.

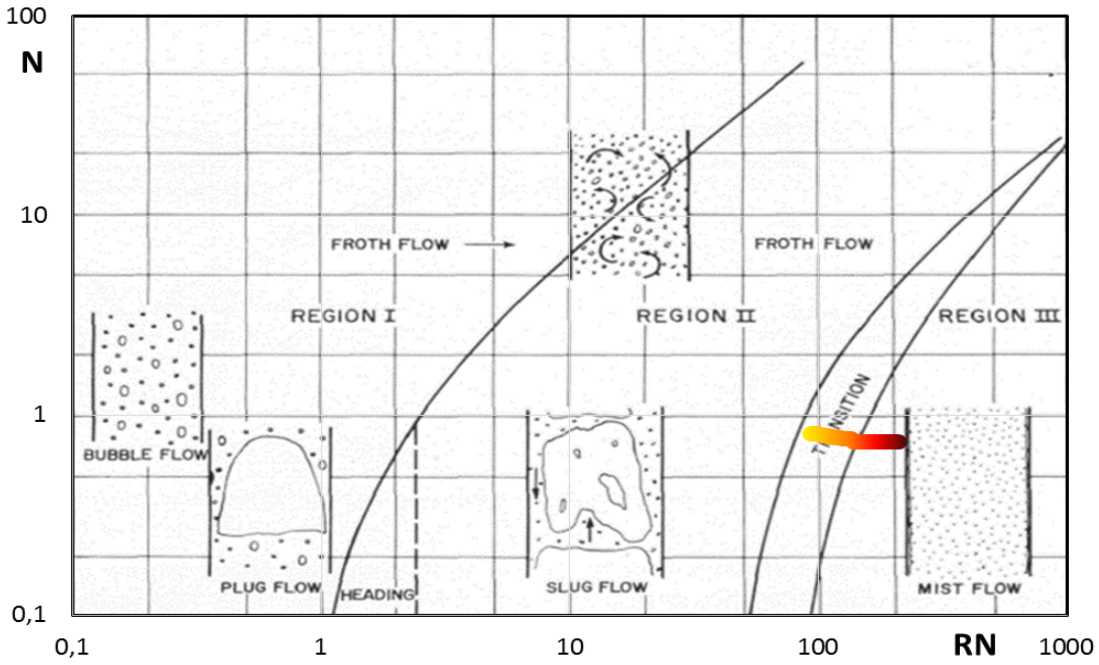

Figure 61: Flow Pattern Chart of the Reference Case according to Duns and Ros [1963].

Figure 62 shows the specified pressure behaviour p of 200 bar bottomhole pressure and 60 bar wellhead pressure. The friction pressure losses are in the order of 109 bar and the hydrostatic losses amount to 32 bar; the acceleration losses represent 0.4 bar. With the specific gas gravity being 0.65, the well is able to deliver 396,000 Nm^3 of gas and 20 Nm^3 of water.

Concerning temperature, the tubing in this scenario is not insulated and heat loss into the formation is facilitated. The fluid temperature T declines from 105 °C at 3000 m depth to 16.5 °C at the surface.

The velocity of the gas and water mixture v varies between 14 and 35 m/s, with the highest velocity at the top of the wellbore, near the wellhead. The Turner velocity v_T again is small by comparison and exhibits values ranging from 1.1 to 1.7 m/s. The critical velocity v_C behaves similarly and reaches speeds of 1.3 to 2.1 m/s. Thus, liquid removal from the wellbore is guaranteed under these conditions.

The fluid density $dens$ behaves as expected and gradually decreases from bottom to top, demonstrating values from 138 to 58 kg/m^3.

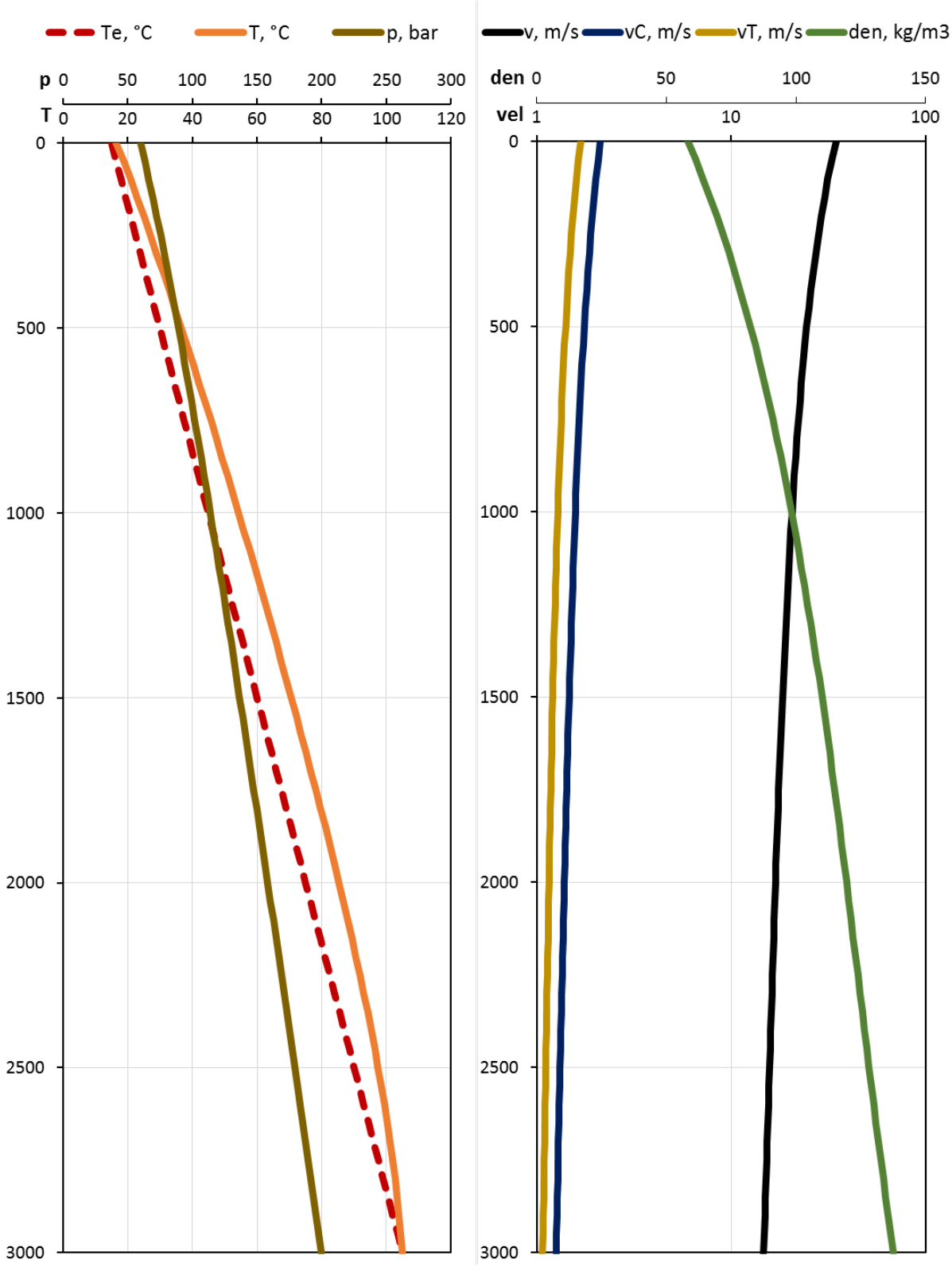

Figure 62: Temperature, Pressure, Velocity and Density Curves of the Reference Case.

Figure 63 visualizes a rather narrow distribution of flow regimes. It seems that while specific gravity variations have a noticeable influence, it is not pronounced enough to cause significant fluctuations in the flow regime. As with the previous scenarios, the prevailing flow patterns are mist flow (near the top, red) and transitional flow (at the bottom of the well, yellow). The increase in specific gravity pushes the flow regime towards the slug and transitional region. This is in line with the gas production rates which vary between 369,000 Nm^3/d for a specific gas gravity of 0.75 and 429,000 Nm^3/d for a specific gas gravity of 0.55.

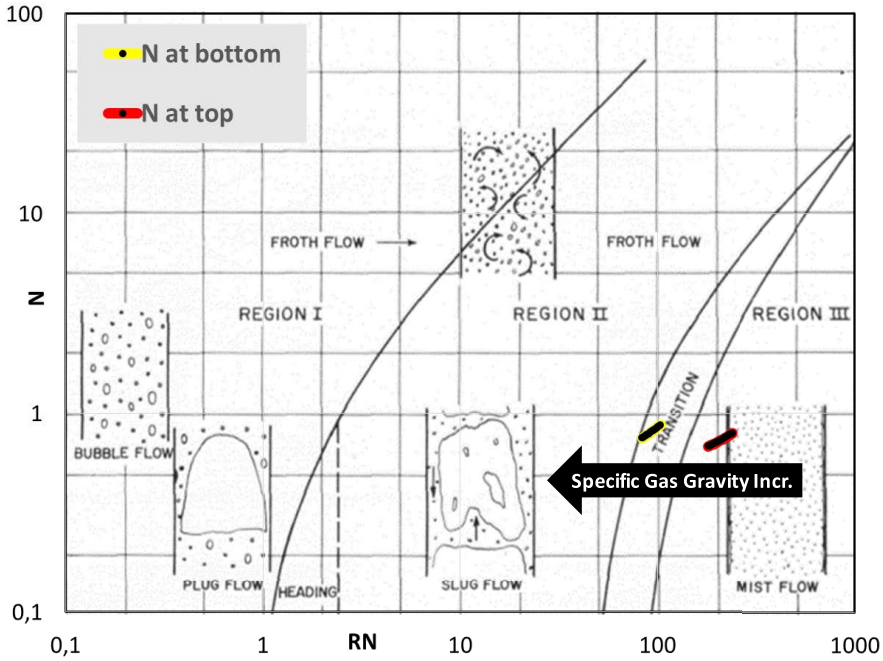

Figure 63: Duns and Ros [1963] Flow Pattern Chart of all Scenario Variations.

In Figure 64, the pressure losses are plotted against the gas production rate which is in the range of 360,000 to 430,000 Nm^3/d. Since the pressure values at the wellhead and the bottom of the wellbore are predefined, the total pressure loss ΔP_total remains constant. However, it can be observed that with increasing flowrate and simultaneously decreasing specific gas gravity, the friction pressure losses $\Delta P\_fr\ ct\ on$ increase while the hydrostatic pressure losses ΔP_hydro decrease. As before, the acceleration term is almost negligible.

Figure 65 shows the bottomhole flowing pressure $p\ HF$ and the fluid temperature at the wellhead Tf, WH versus the daily gas production rate. The bottomhole pressure was set constant. The temperature, however, increases with increasing gas flowrates. This can be attributed to the circumstance that higher flowrates necessitate higher fluid velocities and thus, less time for the fluid to interact with its surroundings and lose heat energy into the formation. The temperature difference between gas rates of 360,000 to 430,000 Nm^3/d is about 6 °C.

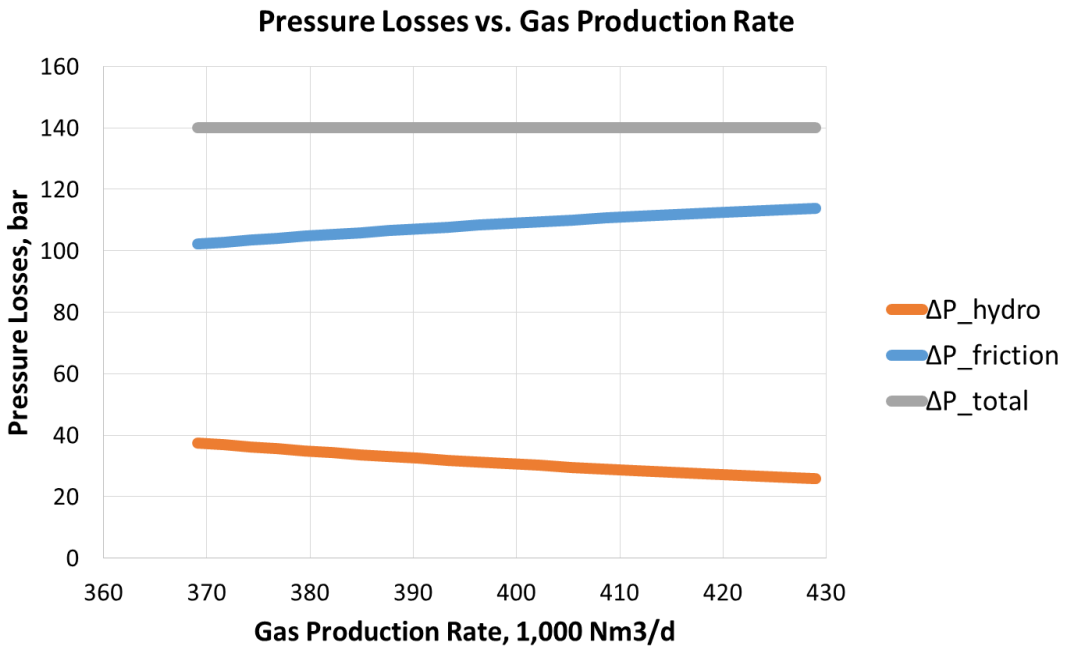

Figure 64: Pressure Losses vs. Gas Production Rate.

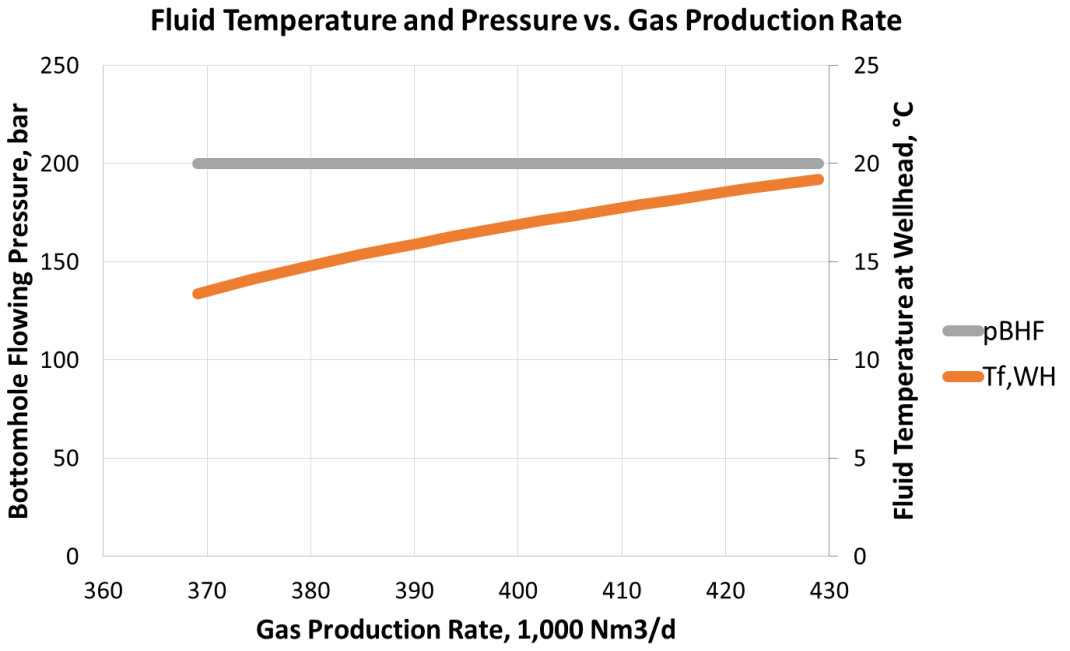

Figure 65: Wellhead Fluid Temperature and Bottomhole Flowing Pressure vs. Gas Production Rate.

4.3.4 Scenario 4

In the fourth scenario, the influence of insulation on the required bottomhole flowing pressure for certain gas production rates is investigated. The insulation thickness is varied between 0 and 1 inch of insulation, in steps of 0.05 inch. The insulation material has a conductivity of 0.02 W/m°K. Also, perfect insulation is simulated by ignoring formation heat transfer. The gas production rates are varied between 100,000 and 350,000 Nm^3/d.

Table 13 shows all parameters of this scenario.

Table 13: Setup of Properties for Scenario 4.

Properties	Scenario 4
Spec. Gravity of Gas, -	0.6
Bottom Hole Flowing Pressure, bar	t.b.d.
Wellhead Flowing Pressure, bar	60
Gas Production Rate, Nm^3/d	100000, 350000
Water Production Rate, Ncm^3/Nm^3	50
Tubing Outer Diameter, inch	2 3/8
Tubing Wall Thickness, inch	0.2175
Insulation Thickness, inch	0, 0.05, 0.10...1 and perfect
Cement Conductivity, W/m°K	2
Casing Conductivity, W/m°K	16 (steel)
Tubing Conductivity, W/m°K	16 (steel)
Insulation Conductivity, W/m°K	0.02
Annular Fluid (Water / Gas)	G
ignore JT effect?	no
ignore formation heat transfer?	no / yes (for perfect insulation)
ignore kinetic energy term?	no

In Figure 66, the flow pattern for a wellhead flowing pressure of 60 bar and a daily gas production rate of 350,000 Nm^3 is shown. The insulation thickness is 0.5 inch and the specific gas gravity is 0.6. The bottomhole flowing pressure required to allow for such a gas rate under the given conditions is determined to be about 182 bar. Also, a water production rate of 60 Ncm^3/Nm^3 is assumed, causing a daily amount of produced water of 21 Nm^3.

Given these circumstances, the flow regime is changing during its way up the tubing from transition (green color) to mist flow (blue color).

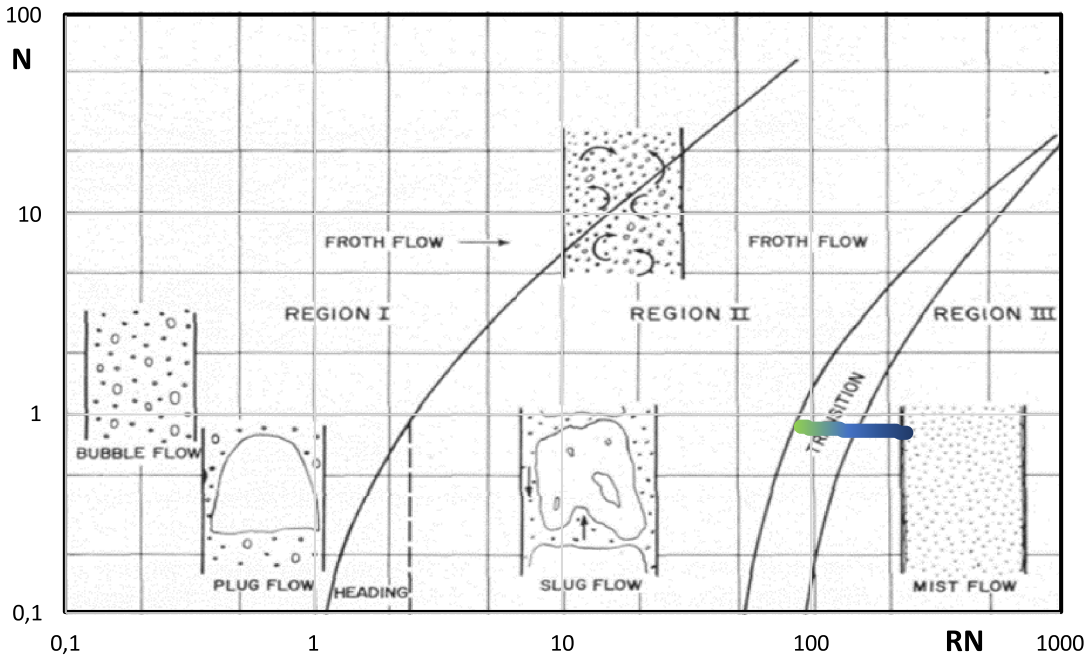

Figure 66: Flow Pattern Chart of the Reference Case according to Duns and Ros [1963].

As can be seen in Figure 67, while the formation temperature T_e behaves as it does in the previous scenarios, the fluid temperature T in the tubing at the wellhead is significantly higher than before due to the influence of the insulation. The fluid temperature still decreases, but the reduction from 105 °C at the bottom of the well to almost 62 °C at the surface is much smaller than in the previous uninsulated situations.

To sustain a wellhead pressure p of 60 bar, a gas production rate of 350,000 Nm^3/d and a water production rate of 21 Nm^3/d, the flowing bottomhole pressure is required to be at least 182 bar. The pressure difference of about 122 bar consists of friction losses in the order of 98 bar and hydrostatic losses of 24 bar.

Concerning the velocities, the fluid velocity v ranges from 14 to 38 m/s and easily surpasses the critical v_C and Turner velocities v_T which range from 1.4 to 2.4 m/s and 1.2 to 2.0 m/s, respectively. Again, liquid loading is not expected to occur under these conditions.

The density $dens$ of the gas-water mixture varies between 43 and 116 kg/m^3. As in the previous scenarios, it declines from bottom to top of the wellbore.

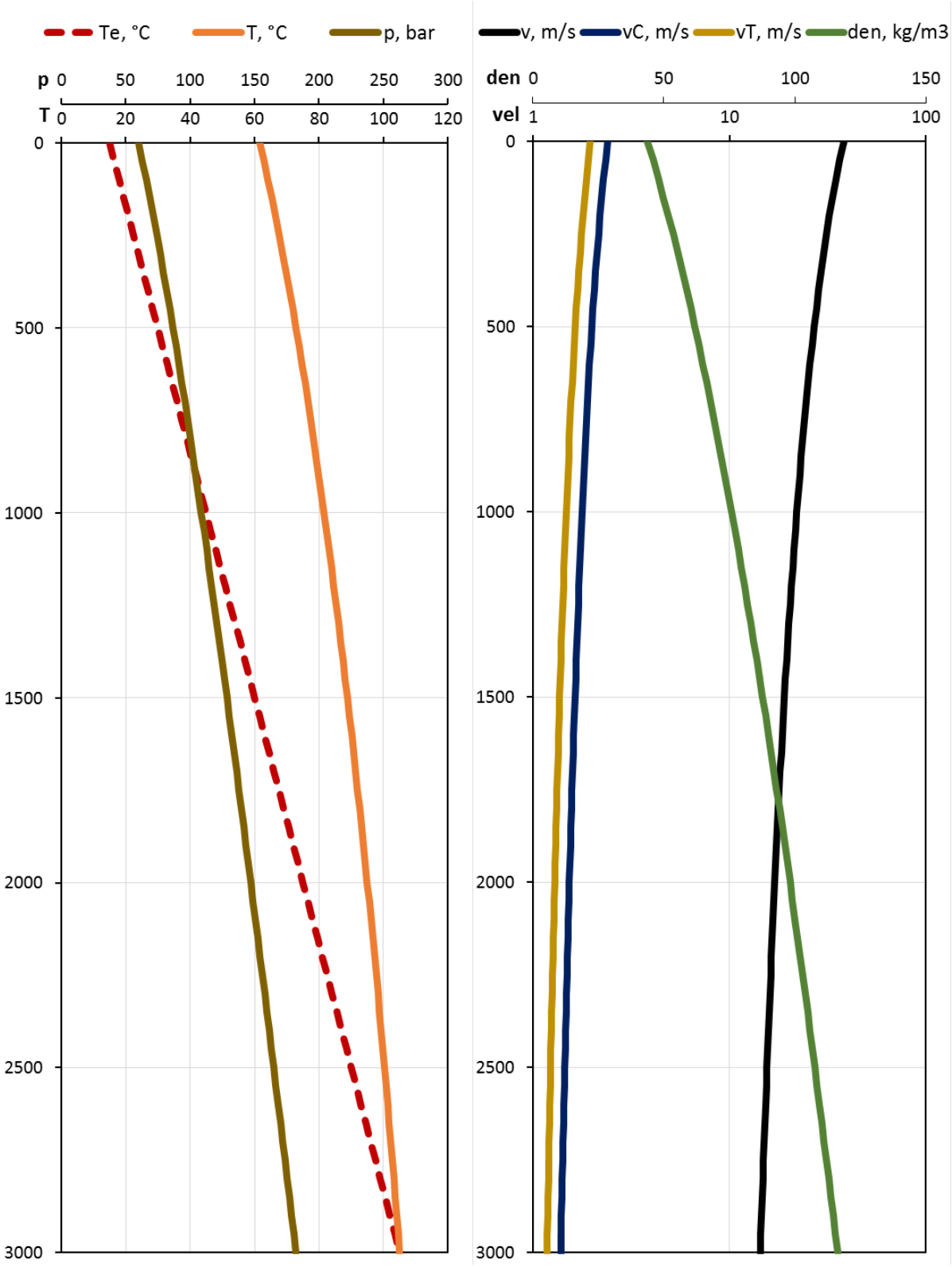

Figure 67: Temperature, Pressure, Velocity and Density Curves of the Reference Case.

Figure 68 shows 22 flow regime conditions for a daily gas production rate of 100,000 Nm^3 and 22 flow regime conditions for a daily gas production rate of 350,000 Nm^3, with varying insulation thicknesses. The flow regime conditions for the lower gas production rate of 100,000 Nm^3/d are located on the border of slug flow to the transition area (yellow and red color). On the other hand, the flow patterns for the gas production rate of 350,000 Nm^3/d are transition flow to mist flow (green to blue), varying with the insulation thickness, and have a N-value close to 1.

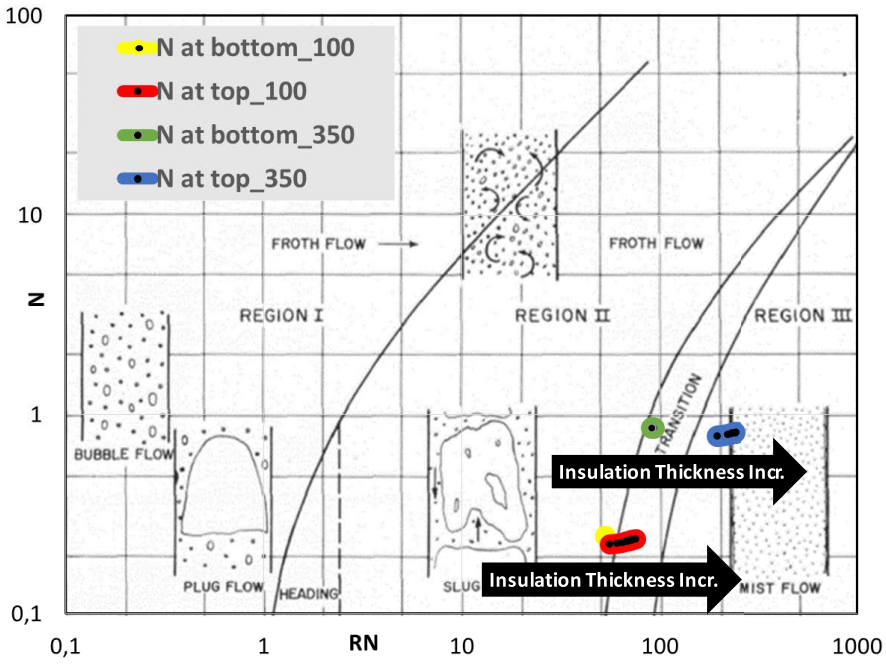

Figure 68: Duns and Ros [1963] Flow Pattern Chart of all Scenario Variations.

Figure 69 compares the pressure losses as a function of the insulation thickness for the two different gas production rates (100,000 and 350,000 Nm^3/d). As can be seen, the friction pressure losses $\Delta P\_fr\ ct\ on$ for the higher flowrate scenarios increase to a much greater extent than the hydrostatic pressure losses ΔP_hydro do. For the lower flowrate scenarios, the friction and hydrostatic losses each account for about 50 % of the total losses. In the higher flowrate scenarios, the friction losses are responsible for about 80 % of the total losses ΔP_total.

Figure 70 depicts the bottomhole flowing pressure $p\ HF$ and the fluid temperature at the wellhead Tf,WH versus the insulation thickness. The bottomhole pressure shows only minor changes and remains relatively constant. The effect of insulation on the fluid temperature is much more pronounced, however. It continuously increases with increasing insulation until reaching a plateau at about 0.5 inch (for the 350,000 Nm^3/d gas rate) and at about 0.7 inch (for the 100,000 Nm^3/d gas rate). The sudden increase at the end is in case of perfect insulation (marked as P^*), and it amounts to 9 °C for the lower gas rate and to 2.5 °C for the higher rate.

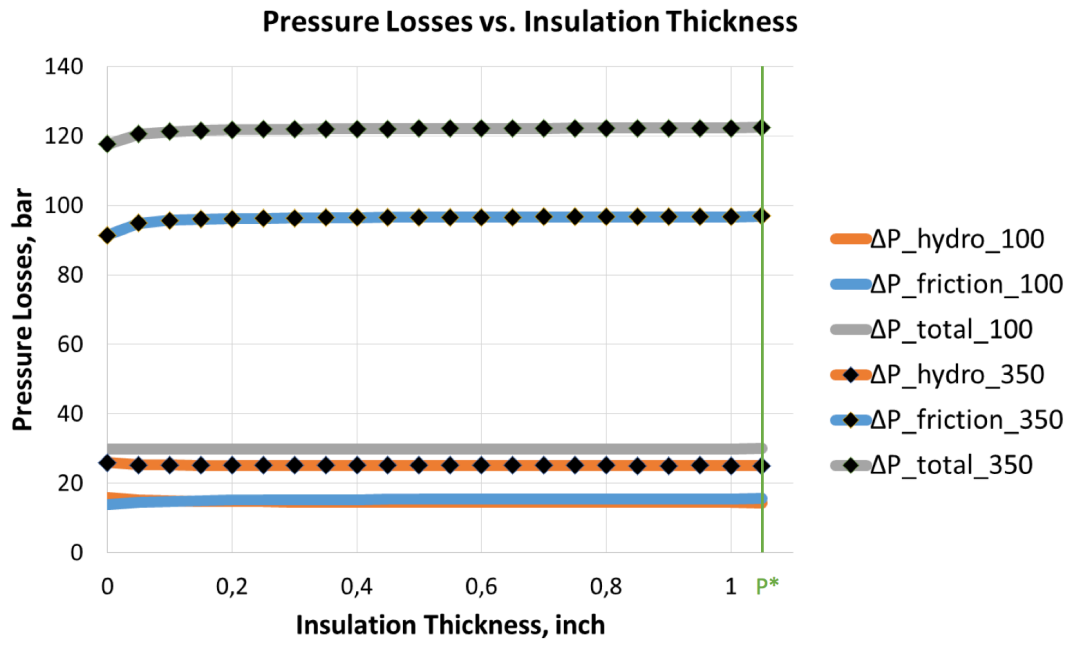

Figure 69: Pressure Losses vs. Insulation Thickness (P* = perfect insulation).

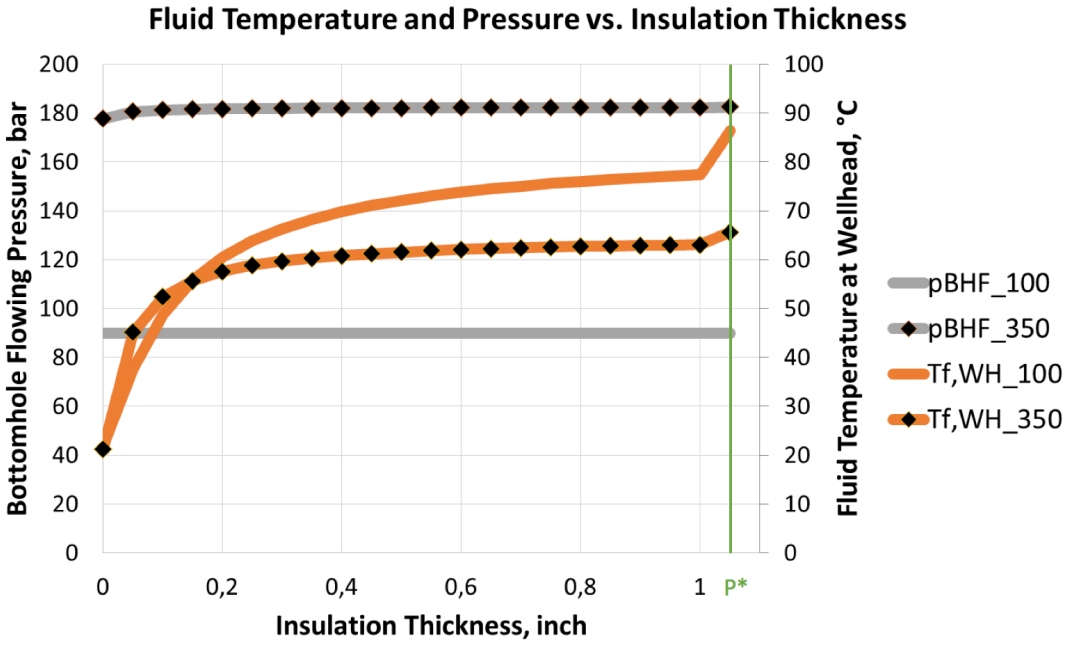

Figure 70: Wellhead Fluid Temperature and Bottomhole Flowing Pressure vs. Insulation Thickness (P* = perfect insulation).

4.3.5 Scenario 5

In the fifth scenario, the influence of ten different water production rates (from 10 to 100 Ncm^3/Nm^3, in steps of 10 Ncm^3/Nm^3) on the gas production rate is tested. Each of these ten different water production rates are evaluated for four tubing outer diameters and their respective wall thicknesses (see Appendix C) to test the influence of available flow area on the gas production rate.

The bottomhole flowing pressure is 140 bar and the wellhead flowing pressure is 80 bar; the specific gas gravity is 0.6. Insulation is non-existent and the formation heat transfer is being considered.

Table 14 shows the parameters of this scenario.

Table 14: Setup of Properties for Scenario 5.

Properties	Scenario 5
Spec. Gravity of Gas, -	0.6
Bottom Hole Flowing Pressure, bar	140
Wellhead Flowing Pressure, bar	80
Gas Production Rate, Nm^3/d	t.b.d.
Water Production Rate, Ncm^3/Nm^3	10, 20, 30...100
Tubing Outer Diameter, inch	2 3/8, 2 7/8, 3.5, 4
Tubing Wall Thickness, inch	0.2175, 0.22, 0.25, 0.26
Insulation Thickness, inch	0
Cement Conductivity, W/m°K	2
Casing Conductivity, W/m°K	16 (steel)
Tubing Conductivity, W/m°K	16 (steel)
Insulation Conductivity, W/m°K	0.02
Annular Fluid (Water / Gas)	G
ignore JT effect?	no
ignore formation heat transfer?	no
ignore kinetic energy term?	no

Figure 71 shows the flow pattern of the reference case for a bottom hole flowing pressure of 140 bar, a wellhead flowing pressure of 80 bar and a water production rate of 50 Ncm^3/Nm^3. The resulting gas flow rate for a tubing with an outer diameter of 2 3/8 inch and without insulation is 210,000 Nm^3/d, and a water flow rate of 10.5 Nm^3/d. The flow pattern verges on the boundary between slug flow (yellow, bottom of well) and transition flow (red, top of well).

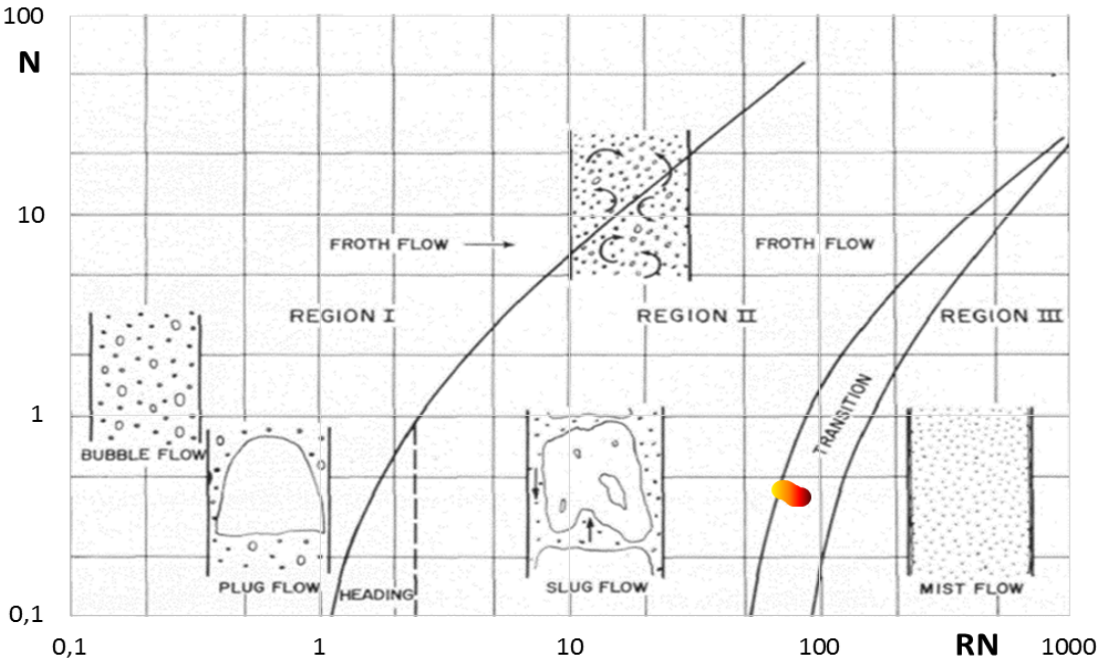

Figure 71: Flow Pattern Chart of the Reference Case according to Duns and Ros [1963].

Figure 72 shows for the reference case that without insulation, the fluid temperature T declines drastically and a significant amount of heat energy is lost into the surrounding formation. The fluid temperature T is 22.2 °C at the wellhead.

The pressure is set at 140 bar bottomhole flowing pressure and 80 bar wellhead flowing pressure. The pressure losses can be split into the two major contributors, with friction losses accounting for 37 bar and hydrostatic losses for 23 bar. This is caused by a gas production rate of 210,000 Nm^3/d and and a water flow rate of 10.5 Nm^3/d.

The fluid velocity v is about 11 to 14 m/s, again with the highest value occuring near the wellhead. The critical velocity v_C ranges from 1.6 to 1.9 m/s and is higher than the Turner velocity v_T which amounts to 1.4 to 1.5 m/s. While the lowest fluid velocity still exceeds the highest critical velocity value by a factor of 5, under these conditions the well may experience load up problems should the bottomhole flowing pressure decrease or the water cut increase. However, at these circumstances the well is still fully able to transport all liquids up to the surface.

The fluid density $dens$ varies between 71 and 89 kg/m^3.

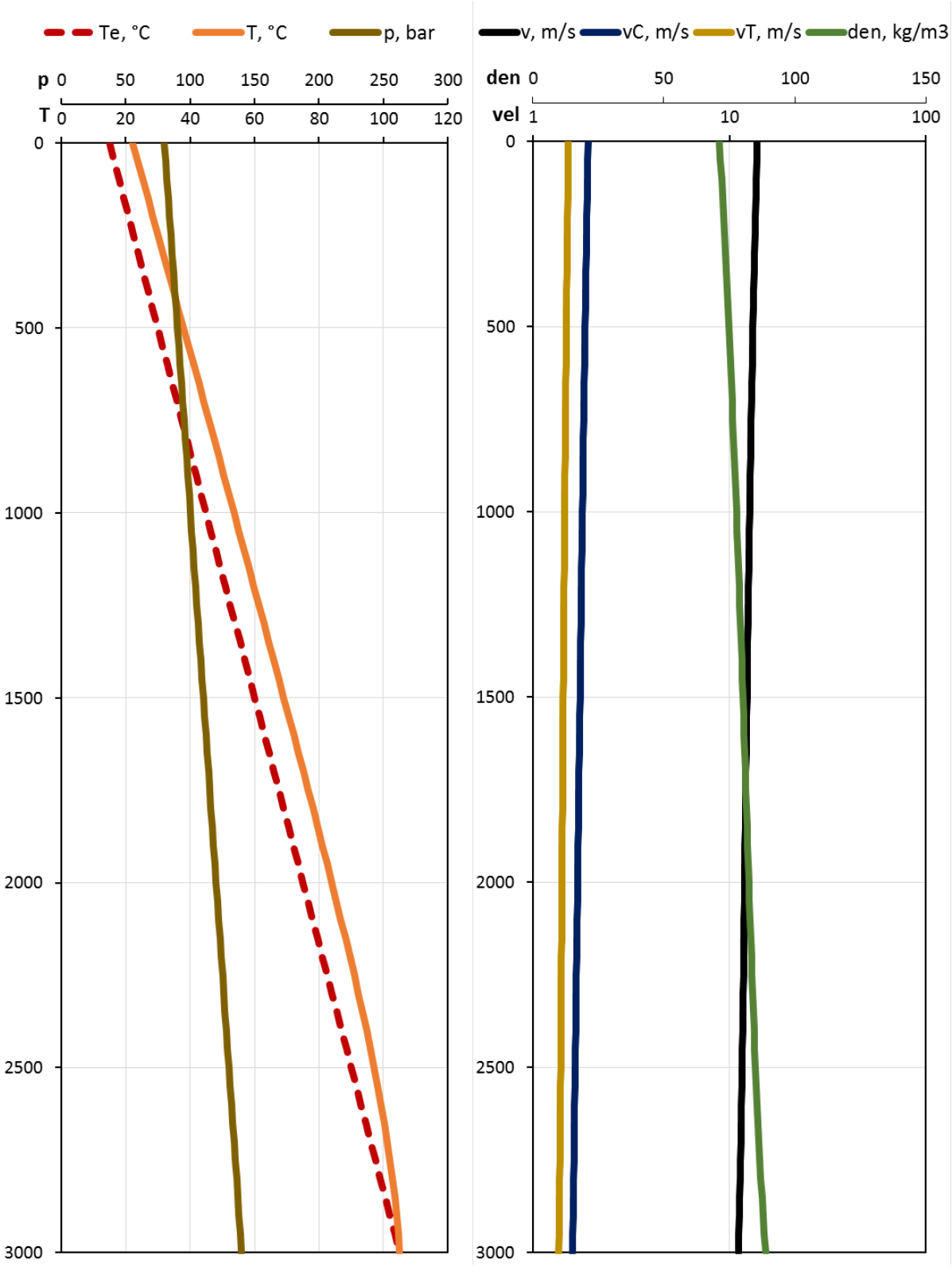

Figure 72: Temperature, Pressure, Velocity and Density Curves of the Reference Case.

Figure 73 displays 40 different flow regime conditions. They are calculated for ten different water production rates with four different tubing outer diameters and their respective wall thicknesses. The gas production rates vary greatly, from about 220,000 Nm^3/d for the 2 3/8 inch tubing up to 900,000 Nm^3/d if a 4 inch tubing is installed. The flow regime for all these variations is nearly the same, however, which is mist flow and transition flow.

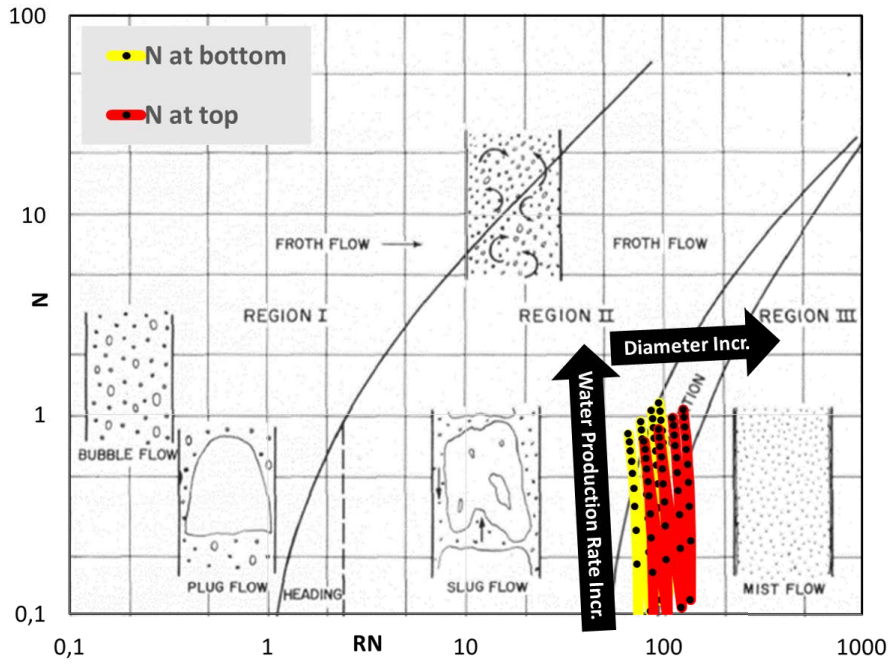

Figure 73: Duns and Ros [1963] Flow Pattern Chart of all Scenario Variations.

Figure 74 shows the pressure losses as a function of the water production rate. It can be seen that an increasing amount of water expectably increases the hydrostatic pressure losses ΔP_hydro. At the same time, friction pressure losses $\Delta P\_fr\ ct\ on$ decrease. This behaviour is true for all four diameter variations.

In Figure 75, the wellhead fluid temperature Tf, WH is plotted versus the water production rate. The result is that the higher the water cut, the warmer the gas-water mixture is at the wellhead. This is interesting since with increasing water cut, the gas production decreases and therefore, the velocity as well which generates a better opportunity for heat loss into the cool surrounding formation. The underlying cause for this may be the larger heat capacity of water compared to gas.

Lastly, Figure 76 shows the aforementioned relationship that increased water production rates necessarily also result in decreased gas production rates $Qgas$. According to the simulation, this effect is more pronounced in larger (4 inch) tubings than in smaller (2 3/8 inch) tubings.

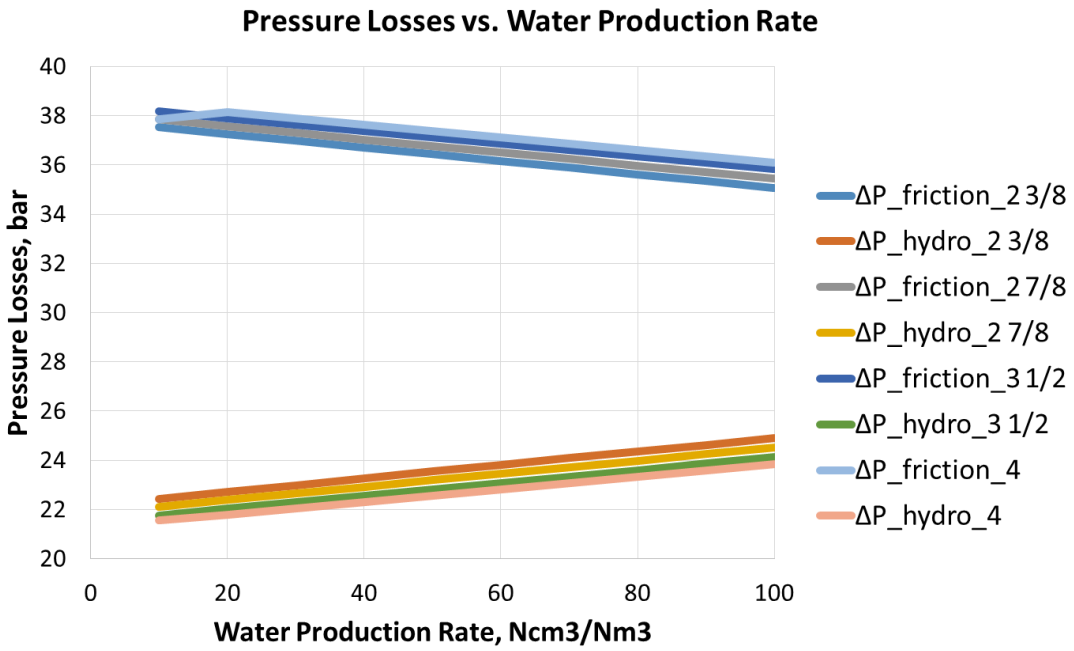

Figure 74: Pressure Losses vs. Water Production Rate.

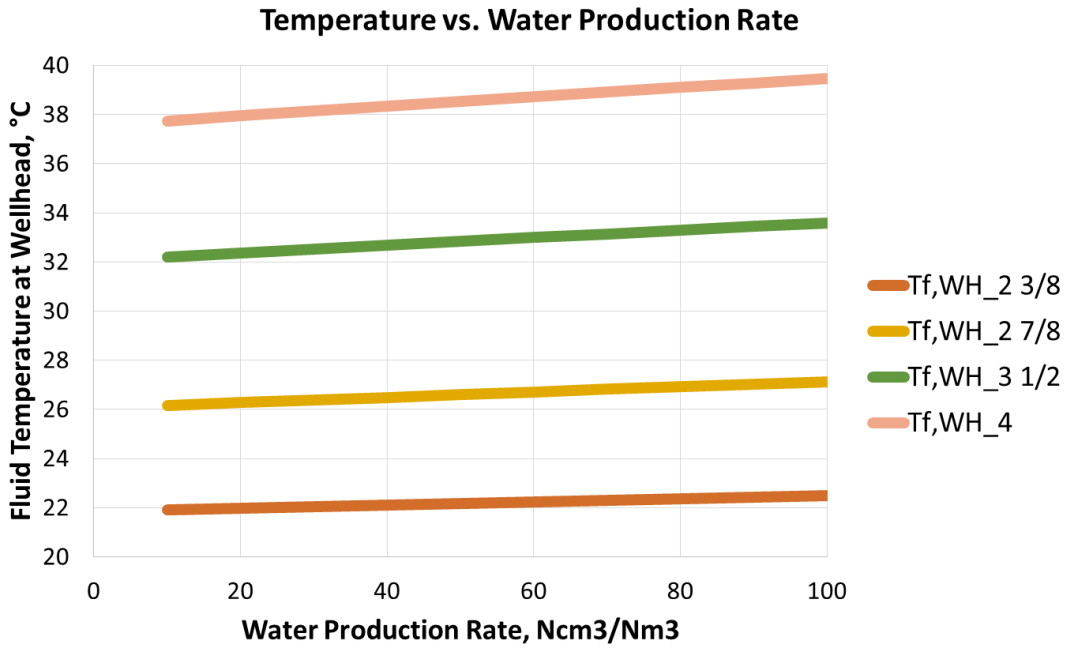

Figure 75: Wellhead Fluid Temperature vs. Water Production Rate.

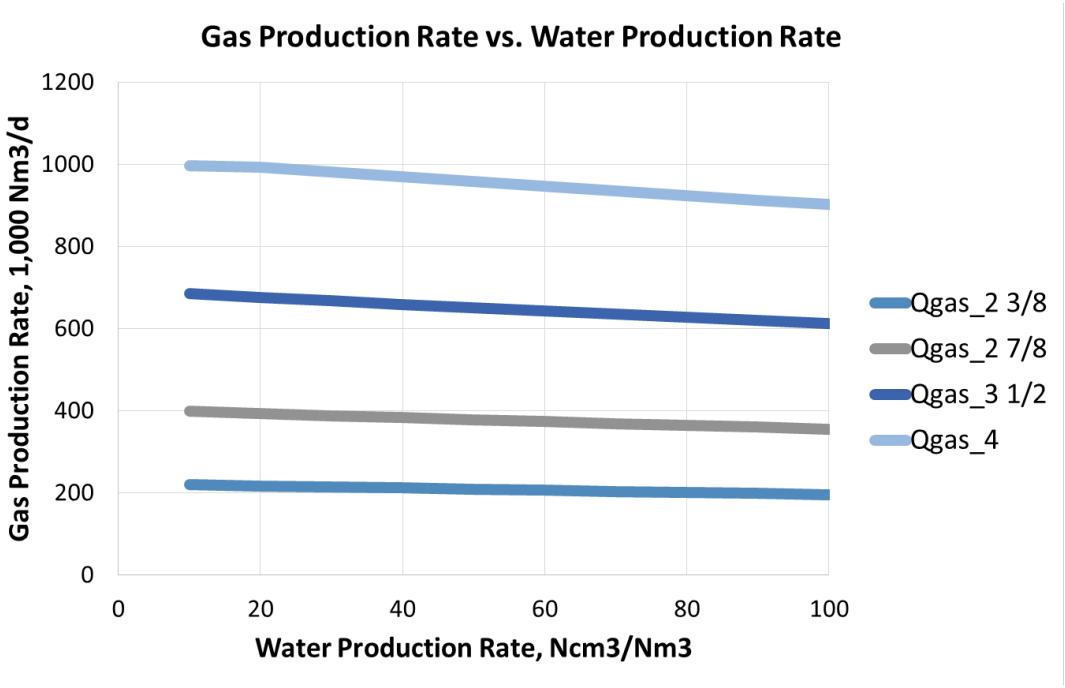

Figure 76: Gas Production Rate vs. Water Production Rate.

4.3.6 Scenario 6

In the sixth and final scenario, using different bottomhole flowing pressures (300 to 100 bar) and a gas production rate of 200,000 Nm^3/d, the resulting wellhead flowing pressure is determined based on two different sets on tubing material.

One setting is calculated with a regular steel tubing with a heat conductivity of 16 W/m°K and the other setting is calculated with a fiberglass, or GFK, tubing with a much lower heat conductivity of 0.045 W/m°K. The results are likely to favor the variation with the fiberglass tubing since it acts as an insulator; both tubing types are assumed to not have any extra insulation.

Table 15 shows all other parameters of this scenario.

Table 15: Setup of Properties for Scenario 6.

Properties	Scenario 6
Spec. Gravity of Gas, -	0.6
Bottom Hole Flowing Pressure, bar	300, 290, 280...100
Wellhead Flowing Pressure, bar	t.b.d.
Gas Production Rate, Nm^3/d	200000
Water Production Rate, Ncm^3/Nm^3	50
Tubing Outer Diameter, inch	2 3/8
Tubing Wall Thickness, inch	0.2175
Insulation Thickness, inch	0
Cement Conductivity, W/m°K	2
Casing Conductivity, W/m°K	16 (steel)
Tubing Conductivity, W/m°K	16 (steel) / 0.045 (GFK)
Insulation Conductivity, W/m°K	0.02
Annular Fluid (Water / Gas)	G
ignore JT effect?	no
ignore formation heat transfer?	no
ignore kinetic energy term?	no

In Figure 77, the bottomhole flowing pressure is 200 bar and the desired gas production rate is 200,000 Nm^3/d. Using a GFK tubing and assuming a water rate of 50 Ncm^3/Nm^3, the wellhead flowing pressure for these conditions is determined to be 148 bar. In this case, the flow pattern would be transition flow (green, bottom of the well) to mist flow (blue, top of the well). In comparison, for a steel tubing and the same conditions, the wellhead flowing pressure would be slightly smaller, namely 140 bar.

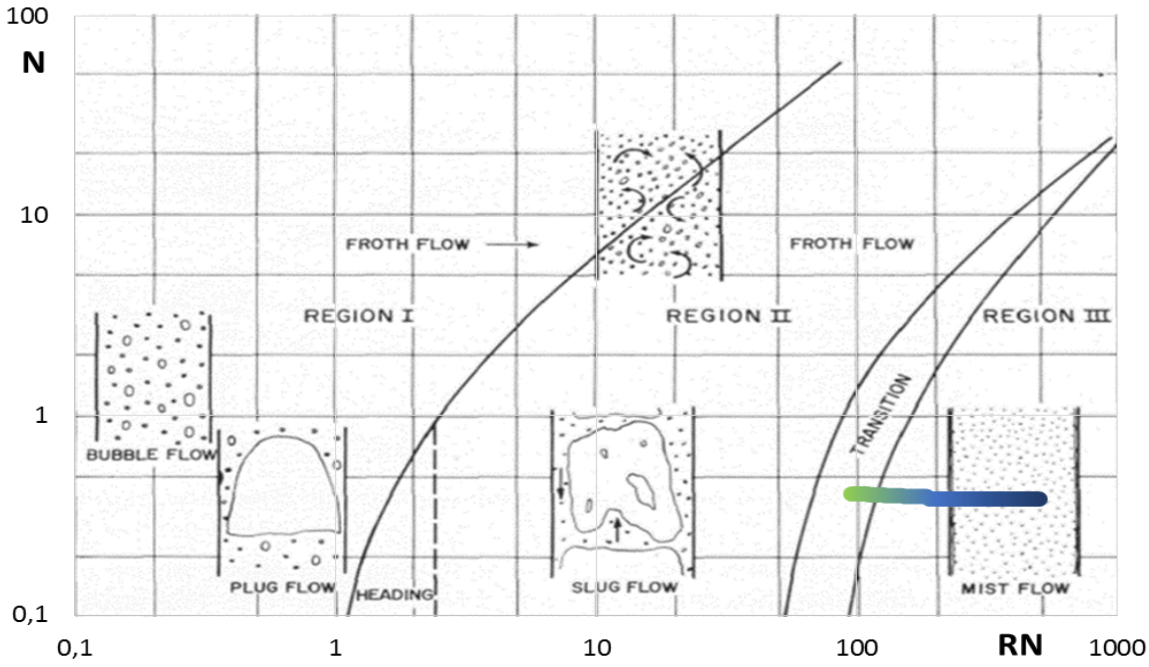

Figure 77: Flow Pattern Chart of the Reference Case according to Duns and Ros [1963].

In Figure 78, the insulating properties of the GFK tubing can be seen clearly. The fluid temperature T is 105 °C at 3000 m depth and decreases slowly on its way to the surface, being 61 °C at the wellhead. Compared to other variations using the steel tubing, this is a significant improvement.

The total pressure losses p are 52 bar, and cause a pressure reduction of the flowing bottomhole pressure of 200 bar to about 148 bar at the wellhead. The friction term is responsible for 22 bar, while the hydrostatic term is 30 bar. This is the case for a gas production rate of 200,000 Nm^3/d.

Concerning the velocity values, the fluid velocity v is rather low with 7 to 9 m/s. The critical velocity v_C ranges from 1.3 to 1.5 m/s while the Turner velocity v_T is calculated to be 1.1 to 1.2 m/s. Again, the conditions allow for continuous liquid removal and liquid loading is not expected to occur under these conditions.

The fluid density $dens$ ranges from 109 to 126 kg/m^3.

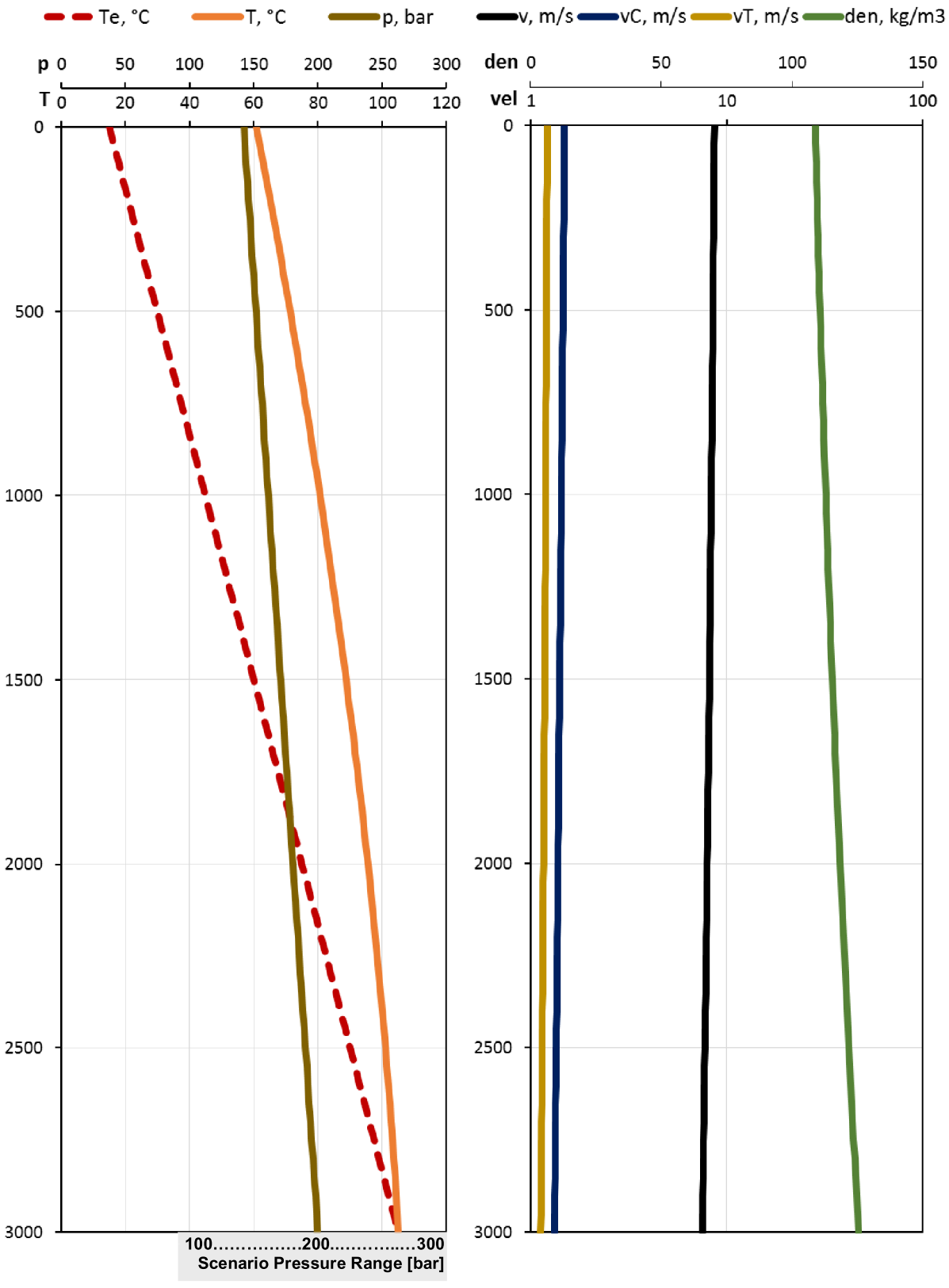

Figure 78: Temperature, Pressure, Velocity and Density Curves of the Reference Case.

Figure 79 shows a larger variation in flow regimes. While the GFK tubing has a valuable effect e.g. on fluid temperature preservation, it does not noticeably influence the occuring flow pattern (green and blue) compared to the steel tubing (yellow and red). The simulation shows that for all 40 variations, the flow regime varies between slug flow and transition flow, with some top sections achieving mist flow. Interestingly, compared to Scenario 2, the increasing BHFP leads to a less favorable flow regime. This is because at lower BHFP, the gas velocity to maintain the required 200,000 Nm^3/d has to be much higher which results in mist flow.

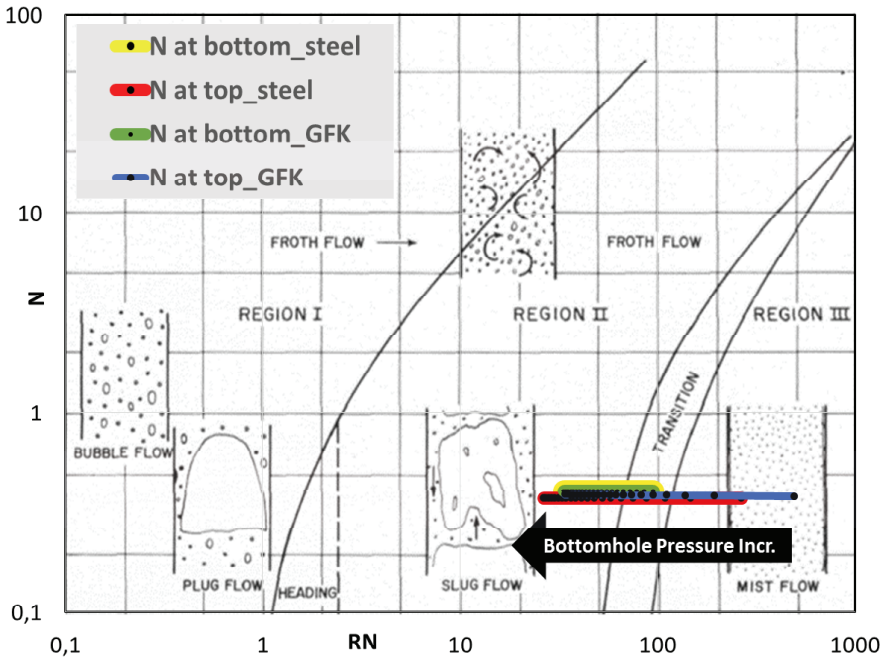

Figure 79: Duns and Ros [1963] Flow Pattern Chart of all Scenario Variations.

Figure 80 displays pressure losses as a function of the flowing bottomhole pressure. It can be seen that a small difference between steel and GFK tubing is detectable. With increasing bottomhole pressure, hydrostatic losses ΔP_hydro increase significantly while the friction losses $\Delta P\_fr\ ct\ on$ decrease. The acceleration losses are negligible. In this scenario, for the GFK tubing, the total pressure losses ΔP_total are 170 bar and 150 bar for the steel tubing.

Figure 81 relates the wellhead flowing pressure $p\ HF$ and the wellhead fluid temperature Tf, WH to the flowing bottomhole pressure. As mentioned, the wellhead pressure is nearly the same for both tubing materials. The temperature shows a significant difference depending on the type of tubing. For the GFK tubing, the wellhead temperature varies between 47 and 65 °C depending on the bottomhole pressure. The steel tubing allows for much lower wellhead temperatures, namely 16 to 20 °C. Thus, the GFK tubing has a pronounced effect on fluid temperatures and heat preservation.

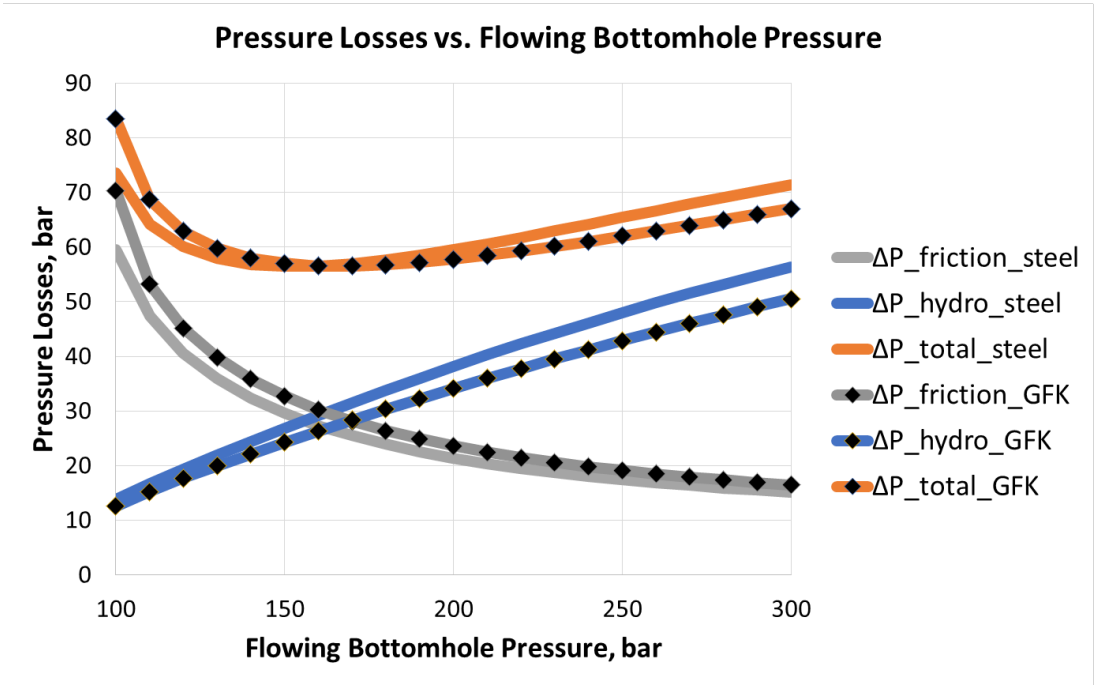

Figure 80: Pressure Losses vs. Flowing Bottomhole Pressure.

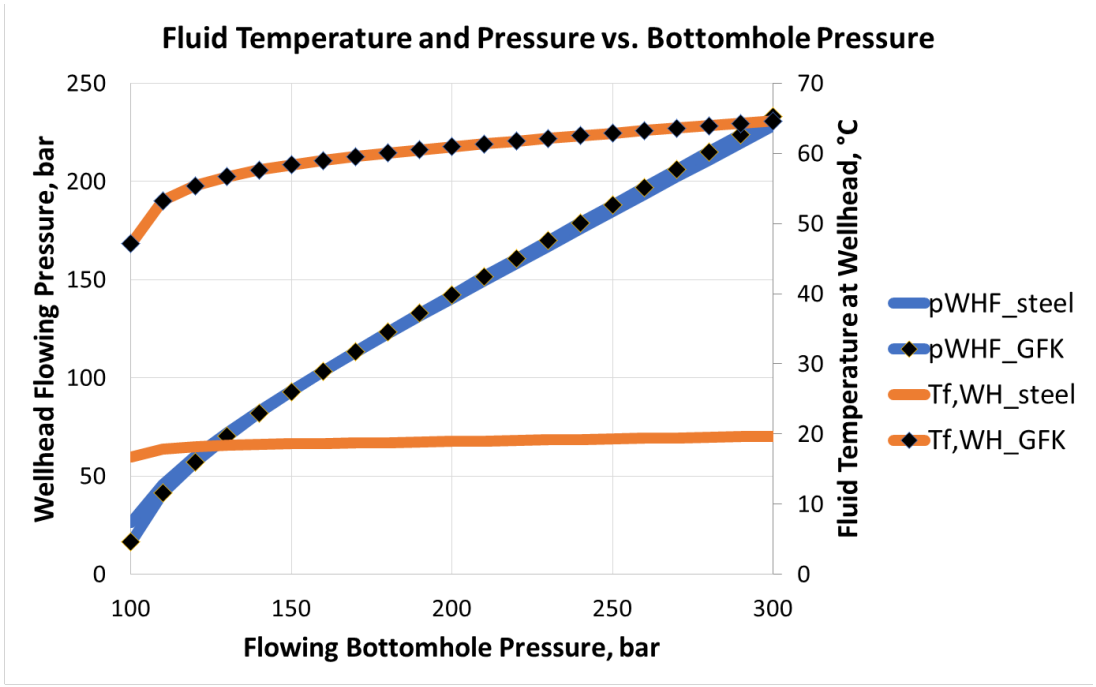

Figure 81: Wellhead Fluid Temperature and Flowing Pressure vs. Flowing Bottomhole Pressure.

5 Conclusion

The main outcome of this work is the possibility to calculate pressure and temperature conditions for every point within the wellbore. This in turn facilitates the accurate determination of required parameters for every point in depth and the opportunity to use this knowledge as a starting point for further evaluations.

Additionally, it is possible to quantify the influence of insulation and of the resulting higher temperature on parameters such as density, fluid velocity and pressure, and all others depending on them. This is the starting point for a great opportunity in terms of gaining a better understanding of heat flow within the borehole, such as to which extent it may be reduced and what measures may prove to be useful in tackling this issue.

Moreover, the approach can be helpful in determining the optimal conditions for gas production, and to demonstrate the benefits of insulation and its resulting influence on liquids in the wellbore. Consequently, this can even lead to reduced costs thanks to a reduced need for artificial lift methods including workovers and to improved ultimate recovery factors by postponing the economic limit of a gas well.

The results of this work are as follows. It has been shown that fluid temperature reductions caused by the geothermal gradient can be mitigated by equipping the tubing with insulating properties. This mitigation of heat energy loss has several desirable effects such as significantly higher fluid temperatures at the wellhead, less pressure losses and higher gas stream velocities along the entire tubing.

This in turn means that a certain gas rate can be maintained for a longer period of time thanks to these consequences which is a highly desirable outcome. Also, even with comparably low gas flow rates where the interaction time between fluid and surrounding formation is much longer, it is possible to achieve higher temperatures along with all previously mentioned benefits.

Another interesting result is the visualization of the prevailing flow regimes following the classification by Duns and Ros [1963]. Most scenarios plot in the mist flow area and therefore exhibit good fluid unloading capabilities. The influence of certain parameters (such as water production rate, BHFP, specific gas gravity, …) on the prevailing flow pattern has been demonstrated and allows a better understanding of how to successfully manipulate a gas well to ensure mist flow.

Moreover, the velocity limits specified by the critical and the Turner velocity allow a possible prediction whether a gas well is near load-up conditions or not. The calculation and the comparison of the critical velocities (which are more accurate and informative than the Turner velocities as they are calculated based on actual parameters instead of average values) show that the Turner velocity values tend to underestimate the values determined by the critical velocity formula. In the simulated reference cases, the actual gas velocity is still considerably larger than the critical or the Turner velocity.

The total pressure losses are comprised of the friction, hydrostatic and acceleration losses. The acceleration losses are minor and never exceed 1 bar in total. Thus, the hydrostatic and the friction losses are mainly responsible for the pressure changes. The hydrostatic pressure losses are usually smaller than the friction pressure losses which can be accountable for up to 80 % of the total losses. In low-flowrate scenarios, however, the friction losses play a smaller role and can be surpassed by the hydrostatic losses.

The insulating properties of GFK tubings as compared to regular steel tubings were also tested and found to be significant, especially when comparing the resulting wellhead fluid temperatures.

To sum up, the MS Excel Tool allows to gain a deeper understanding of how several parameters such as temperature, pressure and density behave under certain conditions, how the flow regimes in such scenarios look like and how all of these interlinked parameters can be influenced by adding insulating properties to the production tubing.

The use of insulation clearly results in improved conditions for the successful removal of liquids from the wellbore and also in significantly more favorable temperature conditions. Thus, a large potential for future improvements may be hidden in the increased propagation of this knowledge.

6 Discussion

As mentioned, the validity of the results depends upon the flow regime which has to be mist flow as a prerequisite for the Entrained Droplet Model to be applicable. If this condition is not met, the applicability of this work is of doubtful meaningfulness.

For future work, more research on the continuous film model will most likely make the obtained results more accurate and representative. Also, the consideration of multiphase modelling and phase changes (from liquid to gaseous phases, and vice versa; including considerations such as the enthalpy of evaporation) may improve the predicted results. The influence of skin which is developing over time and the JT effect of the gas entering the wellbore from the reservoir may potentially also have an impact on the accuracy and validity of obtained results.

Moreover, if workover interventions can be eliminated or at the very least postponed, this effect reduces the risk of lost-time incidents and directly contributes to the HSE record of an operator.

Also, considerations such as the preserving of heat and the increase in ultimate recovery may not be on the agenda of the recently booming fracking industry. However, all companies with thoughtful and future-oriented strategies should consider the benefits presented in this work.

More research on the subject of additional possible insulation methods may prove to be useful. There is a wide range of possibilities; such as coating the tubing or casing, use of insulating cement slurries, installing vacuum insulated tubings and pulling a vacuum on the casing annulus. [48] Also, heating the tubing may prove to be useful.

The use of GFK tubings clearly demonstrates that they have a significant positive effect in terms of preserving the fluid temperature on its way from bottom to surface which in turn also results in better and more favorable fluid and fluid flow properties.

The focus during the simulation was put on vertical wells and their flow regimes. For future work, extending the simulation to cover deviated wells will prove use; especially when considering that this is how most wells are being drilled nowadays.

Last but not least, an economic evaluation of this approach may yield interesting results. This can be used to answer the question if and when the additional cost of insulation will be amortised by increased gas production. This also depends on the applied insulation method.

7 References

[1] BP (2015): BP Statistical Review of World Energy 2015. http://www.bp.com/en/global/corporate/energy-economics/statistical-review-of-world-energy.html (accessed: 2015-10-01)

[2] Österreichisches Bundesministerium für Wissenschaft, Forschung und Wirtschaft (2014): Energieland Österreich. http://www.bmwfw.gv.at/EnergieUndBergbau/Energieeffizienz/Documents/Energieland%20Österreich.pdf (accessed: 2015-10-03)

[3] Fruhwirth, R.K., Hofstätter, H. (2015): Modelling of Wellbore Heat Transfer for Optimising Oil & Gas Production. Powerpoint presentation

[4] Langbauer, C. (2014): Advanced Well Completion, Liquid Load Up of Gas Wells. Powerpoint presentation

[5] Simpson, D. (2006): Low-pressure gas well deliquification requires different approaches. Oil and Gas Journal, Feb. 27 2006, pp.41-50

[6] Fruhwirth, R.K., Hofstätter, H., Schwaiger, G. (2015): Modelling of Wellbore Heat Transfer for Gas Production. 26th International Symposium on Transport Phenomena in Leoben

[7] Lea, J.F., Nickens, H.V., Wells, M.R. (2008): Gas Well Deliquification. Second edition, Gulf Professional Publishing, Elsevier Inc

[8] Turner, R.G., Hubbard, M.G., Dukler, A.E. (1969): Analysis and Prediction of Minimum Flow Rate for the Continuous Removal of Liquids from Gas Wells. Society of Petroleum Engineers. doi:10.2118/2198-PA

[9] Hewitt, G.F. (1961): Analysis of Annular Two-Phase Flow: Application of the Dukler Analysis to a Vertical Upward Flow in a Tube. R-4033 Atomic Energy Royal Establishment, Harwell, England

[10] Dukler, A.E. (1960): Fluid Mechanics and Heat Transfer in Vertical Falling Film Systems. Chem. Eng. Prog. 56, No. 30

[11] Coleman, S.B., Clay, H.B., McCurdy, D.G., Norris, H.L. (1991): A New Look at Predicting Gas-Well Load-Up. Society of Petroleum Engineers. doi:10.2118/20280-PA

[12] Li, M., Li, S.L., Sun, L.T. (2002): New View on Continuous-Removal Liquids from Gas Wells. Society of Petroleum Engineers. doi:10.2118/75455-PA

[13] Lea, J.F., Nickens, H.V. (2004): Solving Gas-Well Liquid-Loading Problems. Society of Petroleum Engineers. doi: 10.2118/72092-JPT

[14] Luan, G., He, S. (2012): A New Model for the Accurate Prediction of Liquid Loading in Low-Pressure Gas Wells. Society of Petroleum Engineers. doi:10.2118/158385-PA

[15] Li, J., Almudairis, F., Zhang, H. (2014): Prediction of Critical Gas Velocity of Liquid Unloading for Entire Well Deviation. International Petroleum Technology Conference. doi:10.2523/IPTC-17846-MS

[16] Holman, J.P. (2002): Heat Transfer. McGraw-Hill. ISBN-10:0078447852

[17] Cheng, N.S. (2008): Formulas for friction factor in transitional regimes. Journal of Hydraulic Engineering, ASCE, 134(9), 1357-1362

[18] Moody, L.F. (1944): Friction factors for pipe flow. Transactions of the ASME 66(8), 671-684

[19] Nikuradse, J. (1933): Strömungsgesetze in Rauen Rohren. V.D.I. Forschungsheft (Berlin) 361: 1-22

[20] https://upload.wikimedia.org/wikipedia/commons/thumb/8/8f/Darcy_friction_factor_for_sand-roughened_pipes%2C_Nikuradse_%281933%29.svg/1599px-Darcy_friction_factor_for_sand-roughened_pipes%2C_Nikuradse_%281933%29.svg.png (accessed: 2015-11-27)

[21] http://www.esru.strath.ac.uk/EandE/Web_sites/13-14/Jacket_Substructures/jackets/images/Shape_CoefficientC.jpg (accessed: 2015-10-09)

[22] Hinze, J.O. (1949): Critical Speeds and Sizes of Liquid Globules. Applied Scientific Research, Volume 1, Issue 1, pp.273-288

[23] http://www.livescience.com/7809-raindrops-fall-sizes.html (accessed: 2015-10-13)

[24] Michel, G., Civan, F. (2006): Modelling Nonisothermal Rapid Multiphase Flow in Wells under Nonequilibrium Conditions. Society of Petroleum Engineers. doi:10.2118/102231-MS

[25] Michel, G., Civan, F. (2008): Modelling Nonisothermal Rapid Multiphase Flow in Wells under Nonequilibrium Conditions. Society of Petroleum Engineers. doi:10.2118/102231-PA

[26] Gnielinski, V. (1975): Berechnung mittlerer Wärme- und Stoffübergangskoeffizienten an laminar und turbulent überströmten Einzelkörpern mit Hilfe einer einheitlichen Gleichung. Forschung im Ingenierwesen, Volume 41, pp145-153

[27] Dropkin, D., Somerscales, E. (1965): Heat Transfer by Natural Convection in Liquids Confined by Two Parallel Plates Which Are Inclined at Various Angles With Respect to the Horizontal. ASME digital collection, Journal of Heat Transfer, Volume 87, Issue 1. pp77-84. doi:10.1115/1.3689057

[28] Mortimer, R.G. (2008): Physical Chemistry. Elsevier Academic Press, p.34

[29] Kay, W.B. (1936): Density of Hydrocarbon Gases and Vapors. Industrial Engineering Chemistry, Vol. 28, pp.1014-1019

[30] Sutton, R.P. (1985): Compressibility Factors for High-Molecular-Weight Reservoir Gases. Society of Petroleum Engineers. doi:10.2118/14265-MS

[31] Sutton, R.P. (2007): Fundamental PVT Calculations for Associated and Gas/Condensate Natural-Gas Systems. Society of Petroleum Engineers. doi:10.2118/97099-PA

[32] Standing, M.B. (1981): Volumetric and Phase Behavior of Oil Hydrocarbon Systems, ninth printing. Richardson, Texas. SPE

[33] Wichert, E., Aziz, K. (1972): Calculation of Z's for Sour Gases. Hydrocarbon Processing, Vol. 5, pp.119-122

[34] Piper, L.D., McCain, W.D. Jr., Corredor, J.H. (1993): Compressibility Factors for Naturally Occurring Petroleum Gases. Society of Petroleum Engineers. doi:10.2118/26668-MS

[35] Elsharkawy, A.M., Elkamel, A. (2000): Compressibility Factor for Sour Gas Reservoirs. Society of Petroleum Engineers. doi:10.2118/64284-MS

[36] Kumar, N. (2004): Compressibility Factor for Natural and Sour Reservoir Gases by Correlations and Cubic Equations of State. Masters Thesis, Texas Tech University, Lubbock, TX, USA

[37] Dranchuk, P.M., Abou-Kassem, J.H. (1975): Calculations of Z Factors For Natural Gases Using Equations of State. Petroleum Society of Canada. doi:10.2118/75-03-03

[38] Standing, M.B., Katz, D.L. (1942): Density of Natural Gases. In Transactions of the American Institute of Mining and Metallurgical Engineers, No. 142, SPE-942140-G, pp.140-149

[39] Borges, P.R. (1991): Correction improves Z-factor Values for High Gas Density. Oil & Gas Journal, Volume 55

[40] Dranchuk, P.M., Abou-Kassem, J.H. (1992): Computer Calculation of Heat Capacity of Natural Gases over a wide Range of Pressure and Temperature. The Canadian Journal of Chemical Engineering, Volume 70: 350–355. doi: 10.1002/cjce.5450700220

[41] Dranchuk, P.M., Purvis, R.A., Robinson, D.B. (1973): Computer Calculation of Natural Gas Compressibility Factors Using The Standing And Katz Correlation. Petroleum Society of CIM, Paper No. 73-112

[42] Lateef, A.K., Omeke, J. (2011): Specific Heat Capacity of Natural Gas, Expressed as a Function of Its Specific Gravity and Temperature. Society of Petroleum Engineers. doi:10.2118/150808-MS

[43] Brown, L., Holme, T. (2011): Chemistry for Engineering Students. Cengage Learning. ISBN-10:1285199022

[44] Chen, Z.A., Ruth, D.W. (1993): On Viscosity Correlations of Natural Gas. Petroleum Society of Canada. doi:10.2118/93-02

[45] Gurbanov, R.S., Dadash-Zade, M.A. (1986): Calculations of Natural Gas Viscosity Under Pressure and Temperature. Azerbaijianskoe Neftianoe Khoziaistvo., No.2, pp.41-44 (in Russian)

[46] Dortmund Data Bank Software & Separation Technology GmbH (2015): http://ddbonline.ddbst.de/DIPPR105DensityCalculation/DIPPR105CalculationCGI.exe?component=Water (accessed: 2015-10-10)

[47] Kestin, J., Sengers, J.V., Kamgar-Parsi, B., Levit Sengers, J.M.H. (1984): Thermophysical Properties of Fluid H2O. Journal of Physical Chemistry, Volume 13, No. 1

[48] Pigott, M.J., Parker, M.H., Mazzanti, D.V., Dalrymple, L.V., Cox, D.C., Coyle, R.A. (2002): Wellbore Heating to Prevent Liquid Loading. Society of Petroleum Engineers. doi:10.2118/77649-MS

[49] http://www.geocities.ws/abouelsaoud/productionstorage/liquidholdup.pdf (accessed: 2015-11-13)

[50] Bahadori, A. (2014): Natural Gas Processing, Technology and Engineering Design.Elsevier, ISBN:978-0-08-099971-5. p.86f

[51] Bellarby, J. (2009): Well Completion Design. Elsevier, ISBN:978-0-444-53210-7. p.263ff

[52] http://www.ingenieriadepetroleo.com/flow-regimes-in-horizontal-and-vertical-pipes.html (accessed: 2015-11-23)

[53] http://www.nptel.ac.in/courses/103105058/images/gd_33.jpg (accessed: 2015-11-24)

[54] Çengel, Y.A., Boles, M.A. (2007): Thermodynamics, An Engineering Approach. McGraw Hill, Sixth edition. ISBN:9780071257718

[55] Gill, W.N., Scher, M. (1961): A Modification of the Momentum Transport Hypothesis. AlChE Journal Volume 7, Issue 1, p.61. doi: 10.1002/aic.690070116

[56] Lockhart, R.W., Martinelli, R.C. (1949): Proposed Correlation of Data for Isothermal Two-Phase, Two-Component Flow in Pipes. Chemical Engineering Progress, Volume 45, pp.39-48

[57] Nosseir, M.A., Darwich, T.A., Sayyough, M.H., El Sallaly, M. (1997): A New Approach for Accurate Prediction of Loading in Gas Wells Under Different Flowing Conditions. Society of Petroleum Engineers. doi: 10.2118/37408-MS

[58] Willhite, G.P. (1967): Over-all Heat Transfer Coefficients in Steam and Hot Water Injection Wells. Society of Petroleum Engineers. doi: 10.2118/1449-PA

[59] Abou-Kassem, J.H., Mattar, L., Dranchuk, P.M. (1990): Computer Calculations of Compressibility of Natural Gas. The Journal of Canadian Petroleum Technology, Volume 29, No. 5, pp.105-108

[60] Rojey, A., Jaffret, C., Cornot-Gandolphe, S., Durand, B., Jullian, S., Valais, M. (1997): Natural Gas, Production Transport Processing. Editions Technip, Paris. ISBN:2710806932

[61] http://www.engineeringtoolbox.com/water-thermal-properties-d_162.html (accessed: 2016-01-18)

[62] Van Wingen, N. (1950): Viscosity of Oil, Water, Natural Gas, and Crude Oil at Varying Pressures and Temperatures. Secondary Recovery of Oil in the United States, American Petroleum Institute

[63] McCain Jr., W.D. (1991): Reservoir-Fluid Property Correlations – State of the Art. Society of Petroleum Engineers. doi:10.2118/18571-PA

[64] Ahmed, T. (2007): Equations of State and PVT Analysis, Applications for Improved Reservoir Modeling. Gulf Publishing Company, Houston, TX, USA

[65] Teja, A.S. (1983): Simple method for the calculation of heat capacities of liquid mixtures. J. Chem. Eng. Data, 28. doi:10.1021/je00031a025

[66] Thome, J.R. (2010): Engineering Data Book III. Chapter 12, p.12-1 ff. Wolverine Tube Inc., Lausanne, Switzerland

[67] Orkiszewski, J. (1967): Predicting Two-Phase Pressure Drops in Vertical Pipe. Society of Petroleum Engineers. doi:10.2118/1546-PA

[68] Duns Jr., H., Ros, N.C.J. (1963): Vertical flow of gas and liquid mixtures in wells. World Petroleum Congress. doi:WPC-10132

[69] Thome, J.R. (2010): Two-Phase Flow Patterns and Flow Pattern Maps. Faculty of Engineering Science, Lausanne, Switzerland

[70] http://www.geocities.ws/abouelsaoud/productionstorage/liquidholdup.pdf (accessed: 2016-01-20)

[71] http://booksite.elsevier.com/samplechapters/9780123858689/Chapter_3.pdf (accessed: 2016-02-02)

[72] http://www.engineeringtoolbox.com/emissivity-coefficients-d_447.html (accessed: 2016-02-02)

[73] https://en.wikipedia.org/wiki/List_of_thermal_conductivities (accessed: 2016-02-04)

[74] Langbauer, C. (2015): Advanced Well Completion: Liquid Load Up of Gas Wells. Lecture Notes. Chair of Petroleum & Geothermal Energy Recovery, MU Leoben, Austria

[75] IFP Energies Nouvelles (2014): Properties of Natural Gases at High Pressure. doi: http://www.ifpenergies nouvelles.fr/index.php/content/download/56595/1246566/file/Properties%20of%20Natural%20Gases%20at %20High%20Pressure.pdf

Nomenclature

Constants

g	… Standard acceleration due to gravity, $g = 9.81\ \mathrm{m/s^2} = 32.17\ \mathrm{ft/s^2}$
R	… Universal gas constant, $R = 8.314\ /\ \mathrm{mol}$

Symbols

A	… Cross-section, m^2
A_d	… Droplet cross-section, m^2
A_f	… Flow area, m^2
A_P	… Pipe cross-section, m^2
$_G$	… Formation volume factor of gas
$_W$	… Formation volume factor of water
c_{an}	… Heat capacity of annular fluid, BTU/lb°F
c_D	… Drag coefficient
c_p	… Specific heat capacity of gas, J/kg°K
c_{p_m}	… Isobaric heat capacity, J/kg°K
$c_{p_m}{}^0$	… Ideal isobaric heat capacity, J/kg°K
$c_{p_m} - c_{p_m}{}^0$	… Heat capacity depature from the ideal state, J/kg°K
$c_{p,W}$	… Specific heat capacity of water, J/kg°K
d	… Diameter, m
d_{BH}	… Borehole diameter, m
d_d	… Droplet diameter, m
d_H	… Hydraulic diameter, m
d_P	… Pipe diameter, m
f, f_D	… Friction factor
f_L	… Friction factor for laminar flow
f_T	… Friction factor for turbulent flow
f_{TR}	… Friction factor for fully rough turbulent flow
f_{TS}	… Friction factor for fully smooth turbulent flow
F_B	… Buoyancy force, N
F_D	… Drag force, N
F_G	… Gravity force, N
Gr	… Grashof number
$g(t)$	… Transient heat conduction function
h	… Convective heat transfer coefficient, W/m^2K
$H'(t)$	… Specific transient thermal resistance, mK/W
H_L	… Liquid holdup
k	… Thermal conductivity, W/mK
k_e	… Thermal conductivity of earth, W/mK
k_{ha}	… Thermal conductivity of annular fluid at average temperature, W/mK
k_{hc}	… Equivalent thermal conductivity of annular fluid, W/mK
k_S	… Sand grain diameter, m
L	… Characteristic length, m
m	… Mass, kg
$\dot{m}$	… Mass flow rate, kg/s

M_g … Molecular mass
M_w … Molar mass, kg/mol
n … Number of moles, mol
p … Pressure, Pa
p_b … Pressure at bottom of section, Pa
p_c … Critical pressure, Pa
p_{pc} … Pseudo-critical pressure, Pa
p_{pc}^* … Modified pseudo-critical pressure, Pa
p_{pr} … Pseudo-reduced pressure
p_r … Reduced pressure
p_{SC} … Pressure at standard conditions, Pa
Pr … Prandtl number
q_c … Critical volumetric flow rate, m^3/day
$q_{c,c}$ … Critical volumetric flow rate for condensate droplets, m^3/day
$q_{c,w}$ … Critical volumetric flow rate for water droplets, m^3/day
q' … Specific heat flow, W/m
r … Radius, m
r_{ci} … Inside radius of casing, ft
r_{to} … Outside radius of tubing, ft
Re … Reynolds number
$R_{G/W}$ … Solubility of gas in water
R_t … Thermal resistance, mK/W
R' … Specific thermal resistance, mK/W
S … Loss factor by Luan and He [2012]
T … Temperature, K
ΔT … Temperature difference, K
T_b … Temperature at bottom of section, K
T_c … Critical temperature, K
T_{ci} … Temperature of inside casing surface, °F
$T_{e,b}$ … Earth temperature at bottom of section, K
T_G … Temperature of gas, K
T_{pc} … Pseudo-critical temperature, K
T_{pc}^* … Modified pseudo-critical temperature, K
T_{pr} … Pseudo-reduced temperature
T_r … Reduced temperature
T_{SC} … Temperature at standard conditions, K
T_{to} … Temperature of outside tubing surface, °F
T_w … Borehole wall temperature, K
U … Overall heat transfer coefficient, W/m^2K
v … Velocity, m/s
v_c … Critical velocity, m/s
$v_{c,c}$ … Critical velocity for condensate droplets, m/s
$v_{c,w}$ … Critical velocity for water droplets, m/s
v_{crit-L} … Critical velocity by Li et al. [2002], m/s
v_{crit-S} … Critical velocity by Luan and He [2012], m/s
v_{crit-T} … Critical velocity by Turner et al. [1969], m/s
v_G … Actual velocity of gas, m/s
v_L … Actual velocity of liquid, m/s
$v_{S,G}$ … Superficial velocity of gas, m/s
$v_{S,L}$ … Superficial velocity of liquid, m/s
v_{slip} … Slip velocity, m/s

V	… Volume, m^3
$\dot{V}$	… Volumetric flow rate, m^3/s
$\dot{V}_G$	… Volumetric flow rate of gas, m^3/s
V_R	… Volume at reservoir conditions, m^3
V_{SC}	… Volume at standard conditions, m^3
$\dot{V}_W$	… Volumetric flow rate of water, m^3/s
We	… Weber number
We_c	… Critical Weber number
y_i	… Mole fraction of component i
z	… Compressibility factor
z_{SC}	… Compressibility factor at standard conditions

Greek symbols

α	… Pipe angle, deg
α_f	… Weighting factor by Cheng [2008]
β	… Thermal volumetric expansion coefficient, 1/°R
β_f	… Weighting factor by Cheng [2008]
ε	… Deviation parameter by Wichert and Aziz [1972]
η	… Joule-Thomson coefficient
γ_e	… Geothermal gradient, K/m
γ_G	… Specific gravity of gas
λ	… Local running coordinate, m
λ_L	… No-slip liquid hold-up
μ	… Viscosity, Pa·s
μ_{an}	… Viscosity of annular fluid, lb/ft hr
μ_G	… Gas viscosity, Pa·s
μ_W	… Water viscosity, Pa·s
ρ	… Density, kg/m^3
ρ_A	… Density of air, kg/m^3
ρ_{an}	… Density of annular fluid, lb/ft^3
ρ_C	… Density of condensate, kg/m^3
ρ_E	… Average density of multiphase fluid at equilibrium, kg/m^3
ρ_G	… Density of gas, kg/m^3
ρ_L	… Density of liquid, kg/m^3
ρ_r	… Reduced density
ρ_S	… Density with slippage, kg/m^3
ρ_W	… Density of water, kg/m^3
σ	… Surface tension, N/m
σ_C	… Surface tension of condensate, N/m
σ_L	… Surface tension of liquid, N/m
σ_W	… Surface tension of water, N/m

Superscripts

S	… Standard conditions

Appendices

Appendix A

Due to interfacial shear $_i$, a liquid film with the thickness h on the walls of a vertical tube is transported upwards. In order for this to happen, the interfacial shear has to be larger than the counteracting gravity and friction forces. As shown in Figure 83, at any point y from the tube wall, a velocity v and a shear stress exist. At the wall, a resisting shear stress $_0$ can be found. [8]

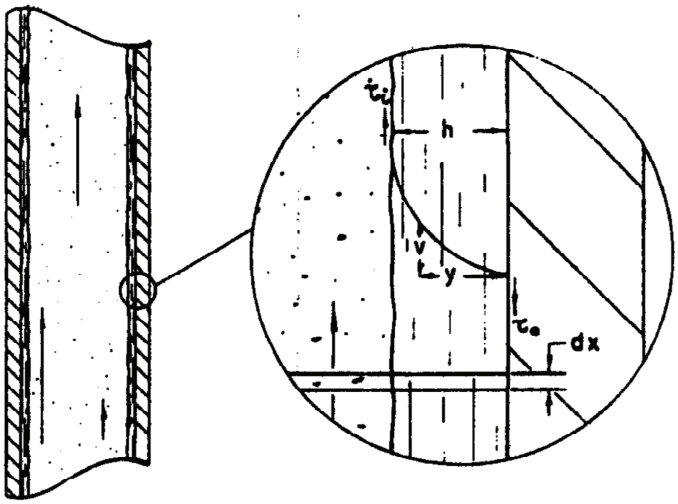

Figure 82: Movement of Liquid Film with Thickness h. [8]

This can also be expressed as a steady-state force balance by the following formula [8]

(A-1) $$\frac{}{_0} = 1 + \frac{y\,\rho_L\,g}{_0 g_c}$$

In a dimensionless form, this can be rewritten as follows. It describes the shear stress distribution depending on the distance from the tube wall. [8]

(A-2) $$\frac{}{_0} = 1 + y^+\frac{\sigma}{\eta}$$

with

$$y^+ = \frac{v^*\,y\,\rho_L}{_L}$$

$$\sigma^3 = \frac{h\ \rho_L{}^2 g}{\eta^2\ {}^2_L}$$

$$\eta = \frac{h\, v^{*}\, \rho_L}{L}$$

$$v^{*} = \sqrt{\frac{{}_0 g_c}{\rho_L}}$$

$$v^{+} = \frac{v}{v^{*}}$$

Next, by using the momentum transport hypothesis by Gill and Scher [1961] the dimensionless velocity distribution in the flow stream can be determined. [8]

(A-3)
$$v^{+} = \int_0^{y^{+}} \frac{2\left(1+y\frac{\sigma}{\eta}\right)}{1+\sqrt{1+4k^2y^{+2}\left(1-e^{\frac{-\phi y^{+}}{y^{+}m}}\right)^2\left(1+y^{+}\frac{\sigma}{\eta}\right)}}\, dy^{+}$$

To find the liquid phase flow rate, the velocity distribution in the liquid film has to be integrated: [8]

(A-4)
$$_L = \pi\, d\, \mu_L \int_0^{\eta} v^{+}\, dy^{+}$$

Equations A-3 and A-4 can then help to determine the minimum required gas rate for a steady upward movement of the liquid film. For this purpose, the minimum flow condition will be when the interfacial shear approaches the gravitational shear, and when the wall shear stress approaches zero. Therefore, the limiting condition is the ratio [8]

(A-5)
$$X = \frac{h\, \rho_L\, g/g_c}{i}$$

For their analysis, Turner et al. [1969] assumed that $X = 0.99$. Moreover, the following relationships were used: [8]

(A-6)
$$\sigma^3 = \frac{X}{1-X}$$

(A-7)
$$\frac{\beta}{\eta^{2/}} = \frac{1}{X^{2/}\ (1-X)^{2/}}$$

(A-8)
$$\beta = \frac{F\, d\, \rho_L{}^{2/}\ g^{1/}}{4\ \ {}_L{}^{2/}}$$

(A-9)
$$F = \frac{\frac{\Delta p}{\Delta x} - \rho\ \overline{\ }_c}{\rho_L \overline{\ }_c}$$

The term $\frac{\Delta}{\Delta x} - \rho_g \frac{g}{g_c}$ is the two-phase pressure drop for which they used a correlation proposed by Lockhart and Martinelli [1949] which is rated as 5/7 for two-phase flow calculations. [56]

For the evaluation, if the calculated minimum flow rate equals the actual flow rate of the test well, it will plot on the diagonal. All wells with near-load up conditions (circles on the graph) should plot near the diagonal. Wells that unload easily (squares) should plot above the diagonal and wells that don't unload (triangles) should plot below. As a result, Turner et al. [1969] found that the results of the CFM do not give a clear indication and drew the conclusion that for liquid unloading, the CFM is not the commanding mechanism. [8]

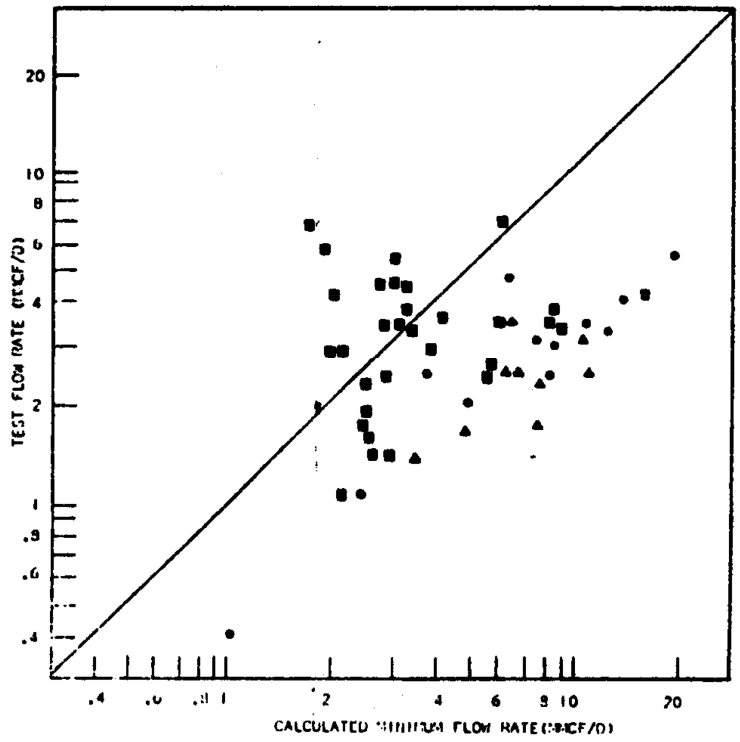

Figure 83: Continuous Film Model after Turner et al. [1969]. [8]

Appendix B

Figure 84 shows the setup of the tool. The entries which are marked in green depict parameters that remain unchanged during the simulation runs to allow for better comparability amongst the scenarios. The blue entries are varied as discussed in the respective results section of each scenario, while the orange fields highlight the three parameters of which two have to be supplied and the missing one will be calculated accordingly.

Setup	CalcWHFP	CalcBHFP	CalcQ
Earth Pars			
Surface Temperature, °C	15		
Geoth. Gradient, °C/100m	3		
Production Pars			
Spec. Gravity of Gas, -	0,6		
Bottom Hole Flowing Temperature, °C	105		
Bottom Hole Flowing Pressure, bar	300,0	300,0	
Wellhead Flowing Pressure, bar	60,0	60,0	
Gas Production Rate, Nm^3/d	579611,1	579,6	
Water Production Rate, Nm^3	5,8	10	
Gas Mass Flow Rate, kg/s	4,8768	ρ_g, kg/m^3	0,7270
Water Mass Flow Rate, kg/s	0,0670	ρ_w, kg/m^3	999,0175
Borehole Pars			
Borehole Depth, m	3.000		
Borehole Diameter, inch	8 1/2		
Casing Outer Diameter, inch	7		
Casing Wall Thickness, inch	0,28		
Tubing Outer Diameter, inch	2 3/8		
Tubing Wall Thickness, inch	0,28		
Isolation Thickness, inch	0,03	3	
Cement Conductivity, W/m°K	2		
Casing Conductivity, W/m°K	16	Steel	
Tubing Conductivity, W/m°K	16	Steel	
Isolation Conductivity, W/m°K	0,02	Rigid Polyurethane Foam	
Emissivity Coefficient	0,5	50	
Annular Pars			
Annular Fluid (Water / Gas)	G	2	○ W ◉ G
Custom Free Conv. Nusselt Number	10		
Use Custom Free Conv. Nusselt Number	0	FALSCH	☐
Simulation Pars			
max. Number of Iterations (Q)	1000	24	4,0 sec
max. Number of Iterations (T)	1000		
max. Number of Iterations (R)	100		
max. Section Length, m	50		
ignore JT effect?	0	FALSCH	☐
ignore formation heat transfer?	0	FALSCH	☐
ignore kinetic energy term?	0	FALSCH	☐
Auto-Calc	0	FALSCH	☐
Monitor Calculations	0	FALSCH	☐
Annular Free Convection Correction Factor	0	0	
End Of Data			

Figure 84: Setup of MS Excel Tool.

Appendix C

Tubing and Casing Sizes

Table 16: Matching Tubing Size with Production Casing Size for Oil and Gas Wells. [71]

Tubing OD			Production Casing OD	
[in]	[mm]		[in]	[mm]
2 3/8	60.3		5	127.0
2 7/8	73.0		5 1/2	139.7
3 1/2	88.9		6 5/8 – 7	168.3 – 177.8
4	101.6		7	177.8

Table 17: Comparison of Nominal Tubing Sizes. [71]

Tubing OD			Tubing Wall Thickness	
[in]	[mm]		[in]	[mm]
2 3/8	60.3		0.2175	5.52
2 7/8	73.0		0.22	5.59
3 1/2	88.9		0.25	6.35
4	101.6		0.26	6.60

Table 18: Comparison of Nominal Production Casing Sizes. [71]

Production Casing OD			Production Casing Wall Thickness	
[in]	[mm]		[in]	[mm]
5	127.0		0.22, 0.25	5.59, 6.43
5 1/2	139.7		0.24, 0.27	6.20, 6.98
6 5/8 – 7	168.3 – 177.8		0.29, 0.35	7.32, 8.94
7	177.8		0.23, 0.28	5.87, 6.91